Nanoparticles as X-ray CT Imaging Contrast Agents in Saturated Porous Media

by

Jacob William Carlos

A thesis

presented to the University of Waterloo

in fulfillment of the

thesis requirement for the degree of

Masters pf Applied Science

in

Civil Engineering

Waterloo, Ontario, Canada, 2020

AUTHOR'S DECLARATION

I hereby declare that I am the sole author of this thesis. This is a true copy of the thesis, including any required final revisions, as accepted by my examiners.

I understand that my thesis may be made electronically available to the public.

Abstract

Parallels exist between medical imaging techniques, such as X-ray computed tomography (CT) or magnetic resonance imaging, and geophysical methods used to analyze the subsurface, such as ground penetrating radar, electromagnetic induction, magnetic susceptibility, or nuclear magnetic resonance. These methods measure a property (or properties) of electromagnetic radiation as it travels through a porous medium, which in turn allows information about the area of interest (i.e., a patient's body or subsurface feature) to be gathered. The use of nanoparticles (NPs) as imaging contrast agents for electromagnetic detection methods is well established in the medical industry but has not been part of the toolbox used to characterize contaminated sites.

X-Ray CT measures differences in X-ray attenuation between two or more materials. The density and the effective atomic number of the material the X-rays are passing through influence attenuation. Thus, in theory, NPs comprised of elements with higher atomic numbers than geologic materials and water should attenuate X-rays more strongly and, therefore, should be distinguishable from the background material. The objective of this research was to evaluate the ability of X-ray CT to monitor the transport of engineered NPs in saturated geologic porous media at a typical column scale. The research findings serve to demonstrate the use of NPs with X-ray CT as a potentially valuable tool to assess hydrodynamic behavior at the bench-scale, and as a proof-of-concept for the use of NPs as imaging contrast agents for field scale EM geophysical techniques.

A 240 kV, GE Phoenix v|tome|x m compact micro CT system was used with three column designs: glass column (15.24 cm long, 2.54 cm inner diameter), acrylic column (10.16 cm long and 0.9 cm internal diameter), and acrylic cuvettes (4.5 cm long, 1 cm by 1 cm cross section). Columns were packed with 150-212 µm acid-washed glass beads and saturated with Milli-Q water. This study assessed the use

of two NP solutions (Fe_3O_4 and bismuth ferrite) as X-ray CT contrast agents for use in saturated porous media columns in comparison to a known contrast agent, NaI.

The minimum concentration of NaI needed to attenuate the X-ray beam enough to be distinguished in processed X-ray CT images was found to be 15 g_I/L in the saturated glass column and acrylic cuvettes. Qualitative comparisons of the relative X-ray attenuation between NaI and the NP solutions were made by scanning two stacked cuvettes, one containing a 15 g_I/L NaI solution and the other containing the respective NP solutions. Results showed that the X-ray attenuation due to Fe_3O_4 NPs was inadequate when used at concentrations < 70 g/L. At this concentration, the Fe_3O_4 NP suspension was too viscous for transport through the column, and thus ineffective as X-ray CT imaging contrast agents in a saturated glass bead porous medium. The bismuth ferrite NP solution had a higher relative X-ray attenuation than the 15 g_I/L solution. These bismuth ferrite NPs were injected at a concentration of ~7.8 g_{Bi}/L into a saturated glass column, and the monitoring of NP transport was successful.

This study marks the first use of engineered NPs as X-ray CT imaging contrast agents in a saturated representative geologic porous medium at the column scale. NPs offer the potential benefit of target-specific binding to impacted soil media in comparison to traditional X-ray CT contrast agents such as NaI, thus opening exciting opportunities for future geological X-ray CT studies. As X-ray CT is an electromagnetic imaging technique, the work presented here serves as a proof-of-concept for the use of NPs as imaging contrast agents for electromagnetic geophysical methods.

Acknowledgments

I would like to thank my thesis advisor, Dr. Neil Thomson, for providing me the opportunity to complete this degree, for the chance to work on an exciting multi-disciplinary project, for helping me deepen my research skills, and for allowing me the chance to obtain fieldwork experience with the rest of my colleagues during this degree. I have learned much in my time at the University of Waterloo, met countless fantastic people, and am very grateful for the opportunities that arose during my time at the school. Thanks to Kammy Sra and Kevin Mcvey for your continued interest in this research, I hope it benefits you as it has benefited me.

Thank you to all the technical staff at Waterloo who play an integral role in the success of graduate research. In particular, Mark Sobon and Mark Merlau, who aided me countless times with sample analysis and apparatus construction.

I would also like to thank all my colleagues who supported and helped with this research. Special thanks to Stuart Linley for his knowledge and aid with nanoparticle synthesis as well as his continued support through editing and advice, as well as to Wanis Nafo for his expertise and assistance concerning X-ray CT imaging. I am also thankful for all the other members of the Soil and Groundwater Research Group at Waterloo, who helped support this research through advice, expertise, and continued support.

Above all, I would like to thank my family and loved ones. Thank you to my loving fiancé Ally, to parents Lisa and Georges, and the rest of my extended family. They always showed enthusiasm and support for whatever endeavor I take on. A special thank you to Felix and Lianne Lopes for your continued interest in my research and your eagerness to support me through it.

This work was financially supported by the Natural Sciences and Engineering Research Council of Canada (NSERC) as well as Chevron Energy Technology Company

Dedication

For my loving wife Ally

and

For my parents, Lisa and Georges

Table of Contents

List of Figures

List of Tables

List of Abbreviations

AA	Acrylic Acid
AC	Alternating Current
ACS	American Chemical Society
BETX	Benzene, Toluene, Ethylbenzene, and Xylene
BTC	Breakthrough Curve
CMC	Carboxymethyl cellulose
CT	Computed Tomography
DCM	Dichloromethane
DI	De-Ionized
DPPC	Dual Pathway Parallel Conductance
EM	Electromagnetic
EMI	Electromagnetic Induction
ERT	Electric Resistivity Tomography
EVA	Ethyl Vinyl Acetate
GPR	Ground Penetrating Radar
GT-nZVI	Green Tea Extract Suported Nanoscale Zerovalent Iron
IC	Iionized Chromatogaphy
ICP	Inductivly Coupled Plasma
IFT	Iodide Flow Through
LNAPL	Light Non-Aqueous Phase Liquid
MD	Multidomain
MRI	Magnetic Resonance Imaging
MS	Magnetic Susceptibility
NAPL	Non-Aqueous Phase Liquid
NMR	Nuclear Magnetic Resonance
NP	Nanoparticle
NSERC	Natural Science and Engineering Research Council
nZVI	Nanoscale Zerovalent Iron
OSTRICH	Optimization Software Toolkit for Research Involving Computational Heuristics
PAMPS	poly(2-acrylamido-2-methyl-1-proanesulfonic acid)
PAMPS-AA	Poly(2-acrylamido-2-methyl-1-proanesulfonic acid) - Acrylic Acid Copolymer
PCBs	Polychlorinated Biphenyls
PCE	Tetrachloroethylene
PHC	Petroleum Hydrocarbon
PSD	Pseudo-Single Domain
PV	Pore Volume
RB	Round Bottom
RNIP	Reactive Nanoscale Iron nanoparticles

RPM	Rotations per minute
SD	single domain
SP	Superparamagnetic
SQUID	Superconducting Quantum Interference Device
TCE	Trichloroethylene
TDR	Time-Domain Reflectometry
VSM	Vibrating Sample Magnetometer
ZVI	Zerovalent Iron

Chapter 1

Introduction

1.1 Background

Nanoparticles (NPs) are an attractive option for in situ remediation due to their enhanced reactivity, relatively low cost, and ability to be delivered to the subsurface (Karn et al., 2009; Wang and Zhang, 1997). Wang and Zhang (1997) showed that iron NPs could be as much as 10 to 100 times more reactive than commercially available iron powders. Karn et al. (2009) also reported that remediation cost savings using nanotechnologies could be as high as 80 to 90% compared to permeable reactive barriers and pump and treat systems. NPs smaller than porous medium pore throats are capable of transport in subsurface environments and have been used for reservoir characterization, oil recovery, CO_2 sequestration, and contaminant remediation (An et al., 2017; Elliott and Zhang, 2001; Hashemi et al., 2013; Javadpour and Nicot, 2011; Rahmani et al., 2015). In some applications, NP coating materials such as polymers and surfactants are used to ensure both NP mobility in the porous medium and binding to a target non-aqueous phase liquid (NAPL). For example, Linley et al. (2019) added a copolymer coating to the surface of iron oxide (Fe_3O_4) NPs which promoted hydrophobic interactions with the target NAPL (i.e., crude oil). They demonstrated preferential binding with ~45 % more NPs bound to crude oil impacted silica sand compared to clean silica sand. Linley et al. (2019) also demonstrated the use of X-ray computed tomography (CT) as a novel non-destructive technique to detect NPs in porous media. Specifically, they showed that NPs are discernable when present in clean silica sand, and when bound to crude oil in oil impacted silica sand, in dry conditions, acting as contrast agents in the reconstructed 3-D X-ray CT images.

The use of NPs as imaging contrast agents for electromagnetic detection methods such as X-ray CT or magnetic resonance imaging (MRI) has been investigated in the medical industry but has not been part of the toolbox used to characterize contaminated sites. Many parallels exist between medical imaging and electromagnetic geophysical methods used to analyze the subsurface, such as ground penetrating radar (GPR), electromagnetic induction (EMI), magnetic susceptibility (MS), or nuclear magnetic resonance (NMR). In both cases, some property (or properties) of electromagnetic radiation is measured as it travels through a porous medium, which in turn allows information about the area of interest (i.e., a patient's body or subsurface feature) to be gathered. Geophysical methods are excellent tools for site characterization and monitoring as they are non-destructive, allow information about the subsurface to be obtained relatively quickly, and are often cost-effective (relative to other characterization methods such drilling). In theory, a conductive or magnetic NP slug at sufficient concentration in the subsurface would alter the electrical or magnetic properties so that electromagnetic geophysical methods could detect its presence. The introduction of such geophysical imaging contrast agents could provide many benefits for site characterization, including identification of NAPL impacted regions.

Geologic material is generally resistive, and thus the measured conductivity by EMI geophysics, for example, is governed primarily by the electrolytic conduction of the pore water (Godio and Naldi, 2009). Immiscible organic contaminants, such as petroleum hydrocarbons (PHCs), are typically resistive (Mazáč et al., 1990). However, they can undergo numerous complex reactions in the subsurface which can influence the ionic composition of surrounding pore water resulting in a wide range of measured resistivities (Godio and Naldi, 2009). Studies have reported both conductive and resistive anomalies associated with subsurface hydrocarbon contamination (Atekwana et al., 2000; Delgado-Rodríguez et al., 2014; Estella a et al., 2002). Furthermore, geophysical methods are not always capable of detecting

NAPL contaminants present in low concentrations (on the order of parts per billions) that may be of a regulatory concern (Godio and Naldi, 2009).

Figure 1-1 shows a conceptual schematic of contamination by crude oil (a light non-aqueous phase liquid or LNAPL) and the use of conductive NPs as geophysical imaging contrast agents to reduce the shortcomings of electromagnetic induction geophysics. Following a baseline EM scan, NPs designed to migrate through the subsurface and preferentially bind to crude oil are injected and allowed to transport into and through the target detection zone. By design, these NPs will preferentially bind to areas of NAPL presence proportional to the bulk soil NAPL concentration. As a result, a post-injection EMI scan may detect areas of increased conductivity based on the NP concentration. Consequently, the reconstructed subsurface image of the EMI scans will provide an indication of the crude oil body location and a sense of the relative mass present. This information may lead to improved remediation design and associated cost savings. While the conceptual schematic shown in Figure 1-1 represents an EMI geophysics application, similar principals would apply for GPR, MS, or NMR.

To date, few studies have assessed the use of NPs as geophysical imaging contrast agents. Modeling efforts by Rahmani et al. (2015, 2014) and by Hu et al. (2016) have shown that subsurface measurements of MS would be sensitive to an injected magnetic or conductive slug (e.g., the presence of conductive or magnetic NPs) and that the movement of such a slug could be observed. Laboratory experiments performed by Buchau et al. (2010) and by Morrow et al. (2015) demonstrated the use of nanoscale zero-valent iron and magnetite particles to enhance the MS in porous media. Many geophysical measurement tools are developed for field scale use and as such, bench-scale geophysical studies typically involve measuring the parameters that influence a geophysical method, but do not use the actual geophysical measurement device. Field scale experiments are often more resource-intensive than bench-scale studies. Thus, it is beneficial to initially investigate the use of NPs as geophysical

imaging contrast agents using another EM method, such as X-ray CT, as a proxy proof-of-concept before moving to field scale experimentation.

X-ray CT has found many uses in geoscience applications and could serve as a suitable bench-scale proof-of-concept method for the use of NPs as imaging contrast agents for EM geophysical methods. Although not typically considered amongst the common geophysical tools, X-rays have found field applicability through X-ray surface and downhole fluorescence (a technique that uses a portable X-ray fluorescence analyzer to obtain information on element types and concentrations) (Ge and Li, 2019; Knoll, 2005; Stromberg et al., 2019). Bench-scale implementations of X-ray CT often place emphasis on assessing pore-scale processes, finding usage for a range of applications such as pore characterization, grain size analysis, fracture analysis, ore analysis, monitoring of dynamic structural processes, fossil characterization, plant root characterization, and petroleum applications (Cnudde et al., 2006; Taina et al., 2008; Zhang et al., 2019). Some X-ray CT studies have also reported on the visual observations of flow processes. For instance, Clausnitzer and Hopmans (2000), and Zhang et al. (2019) successfully used X-ray CT to visually observe the transport of sodium iodide (NaI, a commonly used contrast agent) slug through a soil column.

The initial and successful X-ray CT observations presented by Linley et al. (2019) highlight the potential for the use of NPs as an imaging contrast agent to support site characterization needs. NPs provide an advantage over traditional X-ray CT contrast agents, such as NaI, as they can be engineered to bind to target NAPLs and may be functionalized for treatment. Thus, the use of NPs as imaging contrast agents could potentially open new avenues to detect and treat contamination in shallow subsurface environments. While the findings reported by Linley et al. (2019) are encouraging, their work was conducted using a relatively small spatial scale (acrylic cuvettes measuring 1 cm by 1 cm by 4.5 cm in height) static system packed with dry porous media. To advance this novel NP geophysical monitoring

application as envisioned (see Figure 1-1), the ability of X-ray CT to detect the presence and transport of NPs under saturated conditions at a larger spatial scale must be established.

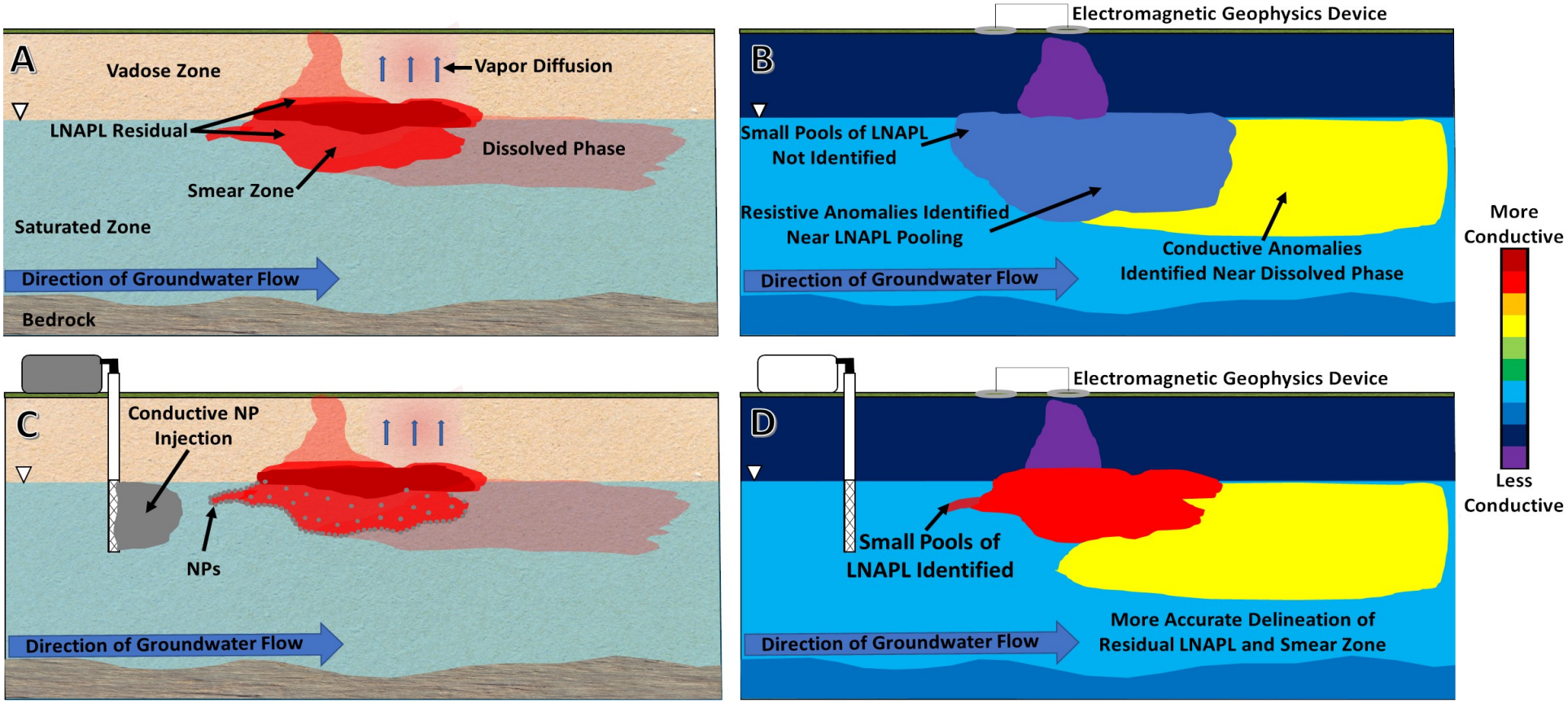

Figure 1-1: Conceptual schematic showing the use of conductive nanoparticles as imaging contrast agents for electromagnetic geophysical scanning of subsurface LNAPL contamination. An example of a LNAPL contaminated site is shown (A). First, a background electromagnetic scan reveals subsurface regions of higher and lower conductivity (B). Then, injection wells are installed upgradient of the presumed contamination zone, and highly conductive NPs, designed for both transport and targeted binding to the LNAPL, are injected and migrate to the areas of LNAPL contamination where they preferentially bind to the areas of highest contaminant concentration (C). A subsequent electromagnetic scan detects areas of higher conductivity where the NPs have bound to the LNAPL, resulting in a delineation of the contamination zone and regions of varying concentrations of the LNAPL (D).

1.2 Research Objective

In this research, X-ray CT is used as a potential tool to assess geologic behavior at the bench-scale, and as a proof-of-concept for the use of NPs as imaging contrast agents for field scale EM geophysical techniques. The overarching objective of this research is to evaluate the ability of X-ray CT to monitor the transport of engineered NPs in saturated geologic porous media at a typical column scale. If successful, this will be the first research to visualize the transport of NPs through a column packed with a representative porous medium using X-ray CT. The overall objective will be considered complete upon the achievement of the following sub-objectives:

1. Establish NP solution contrast in an aqueous environment.
2. Establish NP solution contrast in a saturated porous medium.
3. Isolate and examine X-ray CT artifacts that may impact the use of NPs as imaging contrast agents in column tracer experiments.
4. Determine the effects of concentration and flow rate on X-ray CT contrast agent transport and monitoring.
5. Develop an appropriate methodology to assess the suitability of NP solutions as X-ray CT imaging contrast agents in a saturated porous medium through comparison to a known X-ray CT contrast agent.

1.3 Thesis Scope

This thesis consists of four main chapters. The first (current) chapter outlines the motivation for this research and the main research objective. Chapter two introduces concepts relevant to this research by reviewing literature related to NP transport through porous media, the principals of electromagnetic geophysical methods, current uses of NPs in geophysical studies, the principals of X-ray

CT, fluid flow studies using X-ray CT, and existing applications of NPs as X-ray CT contrast agents in geologic studies. Chapter three examines the use of Fe_3O_4 and bismuth ferrite NPs as imaging contrast agents. Troubleshooting of X-ray CT flow-through experiments is covered in detail. Comparative X-ray CT scans to qualitatively determine the relative X-ray attenuation between NaI and both NP solutions are included. This chapter also describes NaI tracer transport results and their accompanying X-ray CT scans, performed using three concentrations of NaI at three flow rates through glass bead packed columns. The capability to use bismuth ferrite NPs as an X-ray CT imaging contrast agent is demonstrated through the results of a bismuth ferrite transport and scan experiment. Finally, the fourth chapter summarizes the principal conclusions, implications of this research, and recommendations for future research.

Chapter 2

Background Literature

2.1 Nanotechnology for Environmental Hydrogeologic Applications

Wang and Zhang (1997) first suggested the use of nanoscale zerovalent iron (nZVI) for subsurface remediation of trichloroethylene (TCE) and polychlorinated biphenyls (PCBs) when they showed vastly improved dechlorination of TCE and PCBs using nZVI and palladized nZVI (Fe/Pd) in comparison to commercially available ZVI and palladized ZVI powders. This study was followed by the first field scale pilot test of NPs for in situ remediation by Elliott and Zhang (2001), successfully showing proof-of-concept for in situ injections of Fe/Pd to remediate TCE.

NPs are a promising technology that has been extensively studied at both the laboratory and field scale across the world. For example, reviews by Mueller et al. (2012) and Karn et al. (2009) together report a total of 58 field scale sites, in 7 different countries (US, Canada, China, Czech Republic, Germany, Italy, and Slovakia), where NPs have been used for in situ remediation applications. Of all these studies, 98% made use of nZVI (about 29% of which were bimetallic nZVI particles), with the remaining 2% being metal oxides such as nano peroxide (Karn et al., 2009; Kuiken, 2010; Mueller et al., 2012). Most of these field sites were using NPs for the remediation of PCE, TCE, or PCBs. However, other target contaminants include chromium, nickel, nitrates, and BTEX (benzene, toluene, ethylbenzene, and xylene) compounds (Karn et al., 2009; Mueller et al., 2012).

While the high reactivity of NPs renders them effective for breaking down target contaminants, it can also hinder both their stability and mobility in porous media. NPs tend to aggregate due to magnetic and Van der Waals forces, both reducing their ability to migrate through pore spaces and their

specific surface area (i.e., total surface area per unit mass) (Donselaar and Philipse, 1999). Moreover, the high reactivity of NPs can result in interactions with surrounding aquifer materials before reaching a target contaminant. For instance, a study completed in a model aquifer (10 m by 10 m by 2.4 m deep) found completely oxidization of the leading edge of an injected nZVI plume by aquifer material (Johnson et al., 2013). Many research efforts have focused on modifying the surface characteristics of NPs to enhance their stability and mobility in porous media to address these challenges. The substances used to achieve this modification are typically given the broad term of "stabilizers" (Liu et al., 2015; Thomé et al., 2015). See Appendix A-1 for additional details on NP stabilizers.

2.1.1 Subsurface Nanoparticle Transport

The mobility of NPs is typically accessed at the lab scale using column breakthrough experiments. These lab-scale NP transport studies are most commonly conducted in natural and acid-washed sands, however, glass beads, sandstone, and limestone have also been used (Kmetz et al. 2016; Becker et al. 2015; Xue et al. 2014; Ding et al. 2013; Shen et al. 2011; Kotsmar et al. 2010; Tiraferri and Sethi 2009; He et al. 2007; Lecoanet et al. 2004). The columns used in these tests have mostly ranged from 3-20 cm in length and 1-4 cm in diameter, with the larger columns being used for foam transport experiments, and nearly all studies reporting breakthrough concentrations of greater than 90% for the respective stabilized NPs tested (Becker et al., 2015; Ding et al., 2013; He et al., 2007; Kmetz et al., 2016; Kotsmar et al., 2010; Lecoanet et al., 2004; Mystrioti et al., 2015; Shen et al., 2011; Tiraferri and Sethi, 2009; Xue et al., 2014). There is little doubt that stabilized NPs are more mobile through subsurface media than non-stabilized NPs. Lecoanet et al. (2004) compared the mobility of CMC stabilized Fe/Pd NPs in a packed column of loamy sand and achieved a breakthrough of 98%, but only ~0.2% using non-stabilized Fe/Pd NPs under the same conditions. Tiraferri and Sethi (2009) found similar results using

reactive nanoscale iron NPs (RNIP), where breakthrough of non-stabilized RNIPs was negligible in a packed sand column, but NPs stabilized in guar gum achieved a breakthrough of 87%.

Kmetz et al. (2016) conducted an extensive study highlighting the many factors that can influence NP subsurface mobility. These factors include the stabilizer used, pre-coating of the porous medium, NP concentration, injection velocities, and the composition/geochemistry of the porous medium itself. They studied the mobility of stabilized nano magnetite (nMag) mixed with additional polymers and surfactants as amending agents through Ottawa sand and crushed Berea sandstone. NP recoveries were shown to increase by 33 to 44 % depending on the amendment used. Tiraferri and Sethi (2009) also found differences in NP mobility, depending on the stabilizers used. Further, Xue et al. (2014) showed the ability to "optimize" stabilizers. They conducted adsorption tests of PAMPS-AA stabilized iron oxide NPs on silica sand and studied the effect of altering the ratio of PAMPS:AA from 1:1 to 20:1. They found reduced adsorption when the ratio was increased from 1:1 to 3:1, but that increasing the ratio further had little effect. Kmetz et al. (2016) also showed that pre-washing the Berea sandstone before NP injection increased recovery by 54%, and an increase in the injection flow velocity from 2 to 10 m/d resulted in a NP recovery increase from 39 to 55%. Findings from tests done in Ottawa sand indicated that increasing the injection slurry concentration of from 625 mg/L to 2500 mg/g increased recovery from 80 to 97%. While maintaining all other experiment conditions, changing the porous medium from Ottawa sand to crushed sandstone resulted in a decreased recovery from 97% to 38%.

In the study completed by Kmetz et al. (2016), the decrease in recovery due to a change in the porous media is attributed to a reduction in grain size. However, geochemical changes can also affect NP transport. For instance, Mystrioti et al. (2015) found that the elution of GT-nZVI NPs transporting

through a sand/soil mixture, in which the soil had a calcareous composition, decreased from 50 to 0% (after 40 pore volumes) relative to acid washed silica sand. The authors attributed this decrease to neutralization reactions within the NP slurry. Clay and humic acid content have also influence NP transport (Jung et al., 2014). Furthermore, nZVI injected at the field scale has been related to decreased dissolved oxygen in groundwater and oxidized NPs have been collected as far as 1.5 m away from the injection point (Busch et al., 2015; Chowdhury et al., 2015; Johnson et al., 2013).

Other field scale studies have reported NPs traveling as far as 0.8-5.3 m in primarily sand or sand and gravel aquifers, with CMC, stabilized nZVI being the most commonly used NP at the field scale (Busch et al., 2015; Chowdhury et al., 2015; Elliott and Zhang, 2001; Johnson et al., 2013; Kocur et al., 2014). It is worth noting that some field studies do not directly measure NP concentrations and use proxies, such as total iron content, to infer NP transport (Elliott and Zhang, 2001). Unfortunately, field studies assessing the mobility of NPs are difficult to compare due to differences in injection rates, injection concentrations, aquifer parameters (i.e., porosity, conductivity, ect.), and geochemistry.

Most lab studies make use of columns that are approximately 10 cm in length and use flow conditions that are more representative of injection conditions rather than natural flow conditions. Studies have shown that pre-coating a porous media with stabilizer can result in increased mobility, likely due in part to the adsorption of those stabilizers onto the grain surfaces. Thus, smaller columns may not be representative of actual NP mobilities as the initial NPs coat the grains allowing for larger recoveries after several pore volumes. Further, assessing NP transport under injection flow conditions may be adequate if the intent is for NP transport to halt after a certain distance, but where further travel distances are required, it would be best to study transport under natural groundwater flow conditions.

2.2 Electromagnetic Geophysics.

Electromagnetic geophysics methods are based on measuring changes in electromagnetic radiation as it travels through the subsurface. One issue that can arise from geophysical methods is a lack of uniqueness in data interpretation; that is, a measured anomaly could be due to several various factors. Imaging contrast agents, such as NPs that alter the electromagnetic properties of a porous media, could be injected subsurface to allow for improved interpretation of geophysical data and monitoring of chemical or structural changes (such as contaminant mass removal or fracking applications). Although non-electromagnetic geophysical methods exist, such as seismic reflection and refraction methods, they are less likely to be affected by NPs used as imaging contrast agents. As such, the methods that will be discussed in this review have been limited to ground penetrating radar (GPR), electromagnetic induction (EMI), magnetic susceptibility (MS), and nuclear magnetic resonance (NMR).

2.2.1 Ground Penetrating Radar

2.2.1.1 Theory and Fundamentals

Ground-penetrating radar (GPR) is an EM technique that uses high-frequency (10 MHz-1 GHz) EM waves (radio waves) (Everett, 2013a, 2013b). GPR detects variations in EM impedance, or changes in dielectric properties, which alter the propagation and reflection of the EM waves. High-frequency EM waves are rapidly attenuated within the subsurface, and as such, GPR is used primarily for shallow applications (<100 m).

Three main factors contribute to the energy loss of EM waves as they propagate through the subsurface, including geometric spreading, scattering, and absorption. Geometric spreading is the resulting loss of energy per unit volume as EM waves travel radially in a spherical shape away from their

emission source, effectively resulting in a loss of energy at the wavefront. Scattering is the fracturing of EM waves as they encounter changes in electric properties, which increases with increased subsurface heterogeneity. Lastly, some of the energy from an EM wave can be absorbed by a material and converted to heat (Burger et al., 2006a). The term attenuation is used to describe the decrease in wave energy by scattering and absorption, but not due to geometric spreading. Attenuation increases with both material conductivity and frequency; thus, while higher frequency surveys can produce higher-resolution data, they are more limited in investigation depth (Burger et al., 2006a; Everett, 2013a). Further, Cassidy (2007) showed that an increase in the content of magnetic minerals results in greater signal attenuation. Most geologic materials have very low magnetic permeabilities (refer to Section 2.2.3). As a result, many GPR surveys ignore the effect of magnetic permeability unless the area or target of interest is known to have a high content of magnetic material (Burger et al., 2006a).

2.2.1.2 Dielectric Properties of geologic material

Electrical permittivity is a constant of proportionality that is a measure of a substance's ability to displace electric charge within an electric field. Relative electric permittivity, which is also referred to as the dielectric constant, is a material property that describes its electrical permittivity relative to that of free space, which is 8.85×10^{-12} Fm^{-1}.

Most geologic materials have dielectric constants between 3 and 8, air has a dielectric constant of 1, and water has a dielectric constant of approximately 80. Further, increasing salinity and temperature both result in decreases in the dielectric constant of water (Hizem et al., 2008). For a summary of some typical geologic materials and their respective dielectric constants, the reader is directed to other sources (Everett, 2013a). Due to the high dielectric constant of water, soil moisture can have a significant impact on the bulk dielectric constant of geologic material, raising it to values of

10-30 (Everett, 2013a). Topp et al. (1980) developed an empirical equation that describes the bulk dielectric constant of a material with changing water content. In addition to water content, the bulk dielectric constant of geologic materials can be influenced by frequency, the content of magnetic material, and the presence of various contaminants (Bradford, 2007; Cassidy, 2008; Heimovaara et al., 1996; Knight, 2001).

Heimovaara et al. (1996) studied the dielectric permittivity of air, demineralized water, tap water, saline water, and two types of sandy soil using both time-domain reflectometry (TDR) and frequency domain analyzer measurements at frequencies ranging from 0Hz to 3 GHz. They show dielectric permittivity to be a complex function of frequency and found that reasonable predictions of frequency-dependent permittivity can be made using a Debye relaxation curve for frequencies from 0-1GHz. These results would have implications when using TDR or a network analyzer to quantify other medium parameters, such as soil moisture content, for example. The authors also conclude that the higher the complex dielectric permittivity of a material, the lower the useful frequency band is for TDR and network analyzer measurements.

Cassidy (2008) prepared samples of pressed pellets consisting of pure powdered quartz and powdered quartz mixed with varying concentrations of nano-scale magnetite and found that increased magnetite concentration resulted in an increased dielectric permittivity. The dielectric permittivity of the pure quartz samples was found to be frequency independent. In contrast, samples of pure magnetite were found to have a generally decreasing dielectric permittivity with increasing frequency. Although average value for the complex dielectric permittivity appears to be constant from 20 MHz to 3 GHz in this study, small fluctuations were observed indicating that the permittivity is indeed a complex function of frequency, thus agreeing with the results of (Heimovaara et al., 1996). These results also

suggest that the frequency dependency of complex permittivity may be negligible for field scale GPR applications unless a high content of magnetic minerals (likely magnetite) or perhaps magnetic buried objects are present.

2.2.1.3 Research Gaps in GPR Geophysics

When conducting GPR surveys, two issues that are of importance to understand are target polarization and the measurement of thin beds. For a buried target to be effectively detected using GPR, it is required that it scatters enough energy. Coil orientation can be important as scattering in a preferential direction can depolarize the incident electric field. This effect has been observed to occur when using GPR to detect buried pipes. In a study discussed by Everett, (2013a), GPR devices with coils parallel to a buried pipe target (referred to as TM mode) can identify the pipe while GPR devices with coils perpendicular to the target (referred to as TE mode) experience depolarization and are thus unable to detect the pipe. GPR devices can also operate in a cross configuration. Due to this effect, it is typically good practice to run surveys in multiple modes (Everett, 2013a). The other limitation of GPR is the ability to distinguish thin bedding. The thinnest bed that GPR surveys can effectively measure is given by Rayleigh's criterion, defined as $\lambda/4$, where λ is the wavelength (Everett, 2013a). If beds are thinner than this value, then the reflections received above and below the bed will be indistinguishable.

GPR data is typically qualitative and, like many other geophysical methods, suffer from an issue known as non-uniqueness. That is, a detected anomaly can often be attributed to multiple potential causes. Nonetheless, GPR has been used for the delineation of subsurface contamination, and several models have been developed to improve GPR analysis.

Porous media impacted by PHCs tend to have higher resistivities; as a result, it could be expected that a PHC contaminated site would generate unexpected additional reflectors (Mazáč et al.,

1990). LNAPL PHC pools can act as additional reflectors located above the water table, which is one potential characteristic of PHC contamination in GPR radar grams (Atekwana et al., 2000; Cassidy, 2007; Catapano et al., 2014; Mansi et al., 2002). Interestingly, however, shadow zones that are characteristic of landfill leachate or heavy metal contamination have also been identified at hydrocarbon contaminated sites (Atekwana et al., 2002, 2000; Cassidy, 2007). For instance, Atekwana et al. (2000) used GPR, ERT, EM, and soil boring analysis to characterize an old crystal refinery site in which release from storage tanks and pipelines were expected. They found a GPR reflector that corresponded to an oil-stained grey sand layer above the water table but also identified shadow zones in the GPR data that corresponded with zones of high conductivity both above and below the water table. One proposed theory is that zones of higher porewater conductivity arise due to increased mineral dissolution from the byproducts of weathering and biodegradation processes within the hydrocarbon impacted soil (Atekwana et al., 2000). Seasonal fluctuations in the groundwater table may have been responsible for the increased conductivity above and below the average groundwater table location. In agreement with Atekwana et al. (2000), a later study by Cassidy (2007) also discusses the complex response of GPR signals at hydrocarbon sites due to the processes that occur within the "smear zones" that are characteristic of LNAPL contamination. Cassidy (2007) compares GPR radargrams from an LNAPL contaminated site survey and nearby "clean" site surveys. A well-defined reflector in the contaminated surveys, which is attributed to the resistive LNAPL saturated sands, and a much weaker reflector in the clean samples, which can occur due to gradational changes in saturation above the water table due to capillary fringe, were found. The contaminated surveys also showed an increased signal attenuation at depth in comparison to the uncontaminated survey lines. An attenuation attribute analysis conducted on the surveys confirmed that overall signal amplitude was indeed larger for the uncontaminated survey

lines. These results agree with the findings of Atekwana et al. (2000). These studies show the issue of non-uniqueness. That is, both reflectors and shadow zones can be found at hydrocarbon impacted sites and these anomalies can arise from many factors such as the presence of other contaminants, buried metal objects, or changes in the natural electrical properties of the subsurface (Porsani et al., 2004; Reyes-López et al., 2008; Wijewardana et al., 2012). A need still exists to improve GPR survey or analysis methods for hydrocarbon contaminated sites to obtain higher quality information.

Bradford (2007)Bradford derived a function for a dispersion parameter (assigned as 'D') that relates the frequency-dependent attenuation of GPR to the frequency-dependent reflection. A GPR survey over an uncontaminated pond indicated that the theoretically calculated D values based on expected values of dielectric permittivity were relatively close to those recorded. Although the method could not quantify the presence of LNAPL or DNAPL, it was successfully demonstrated to be a good "qualitative indicator of relaxation anomalies caused by the presence of organic contaminants" (Bradford, 2007). Carcione and Seriani (2000) created a model to determine the complex permittivity and conductivity of sand, clay, and silt with varying saturation of air, water, and hydrocarbons Carcione and Seriani (2000). They found that different hydrocarbons (methane and aviation gasoline) have large enough contrasts in dielectric permittivities to be theoretically disguisable by GPR signals. Catapano et al. (2014) used a tomographic inversion algorithm to show how tomographic reconstruction of GPR data can be used to better delineate a hydrocarbon plume. The model developed by Carcione and Seriani (2000) assumes homogeneous and isotropic conditions, which may limit its applicability in certain field scenarios. Another inversion algorithm developed by Catapano et al. (2014) suffered from some delocalization effects as it neglected the layered structure of the soil and assumed a constant wave propagation throughout. The results of these modeling efforts are encouraging with regards to the

improved ability of GPR to delineate hydrocarbon contamination. However, until these models are improved further, these results obtained remain qualitative.

2.2.1.4 NPs as Imaging Contrast Agents for GPR Geophysics

To the author's knowledge, there have been no peer-reviewed publications implementing NP sensing using a GPR geophysical technique. This technique is based on detecting changes in electrical properties within the subsurface at high resolution. As such, there is potential for this method to detect and monitor NPs that change the bulk conductivity or dielectric permittivity of the medium. Increases in these properties could improve the issue of non-uniqueness and potentially allow quantitative information to be obtained from GPR surveys. GPR devices are not as commonly used in a laboratory setting (in comparison to magnetic susceptibility geophysics, for example), which may explain why there is a lack of literature on enhanced GPR imaging combined with nanotechnology.

Several nanomaterials have been shown to change fluid or material conductivity. Alumina oxide nanofluids have been shown to increase in electrical conductivity with increasing concentration of alumina oxide (Ganguly et al., 2009). Conversely, nZVI has been demonstrated by Mar Gil-Díaz et al. (2014) to decrease overall conductivity in soil samples. It should be noted that in this study, the nZVI was coated with polyacrylic acid to stabilize the particles, which may have contributed to these results. Silver NPs have also been found to increase the conductivity of their suspension base fluid (Solanki and Murthy, 2011).

2.2.2 Electromagnetic Induction

2.2.2.1 Theory and Fundamentals

Electromagnetic induction (EMI) geophysics is based on the principles of Faraday's Law of Induction and Amperes Circuital Law. The principles of the method can be described by a set of four equations, known as Maxwell's equations (Boaga, 2017; Burger et al., 2006a):

$$\nabla xE = -\frac{\partial B}{\partial t} = -2\pi i f B \quad \text{2-1}$$

$$\nabla \times H = I + \frac{\partial D}{\partial t} \quad \text{2-2}$$

$$\nabla \times D = \rho c \quad \text{2-3}$$

$$\nabla \times B = 0 \quad \text{2-4}$$

These equations are based on Faraday's Law (Equation 2-1), Ampere's Law (Equation 2-2), Gauss' Law (Equation 2-3), and a law for the magnetic field indicating that there are no magnetic monopoles (Equation 2-4). With $I=\sigma E$, $D=\varepsilon E$, and $B=\mu H$, and where E is the electric field intensity, f is the frequency, $i = \sqrt{-1}$, B is the magnetic induction, H is the magnetizing field density, I is the current density, D is the electrical displacement, σ is electric conductivity, ε is the dielectric permittivity, and μ is the magnetic permeability (Burger et al., 2006a).

Ground conductivity meters used for EMI geophysics typically comprise of a transmitter and receiver coil that is operated at low frequencies (<10-40 kHz) (Burger et al., 2006a; Connell and Key, 2013; Doolittle and Brevik, 2014; Godio and Naldi, 2009; Monteiro Santos et al., 2006). The transmitting electrical coil makes use of an alternating current to produce a magnetic field known as the primary

field. This field, in turn, induces electrical eddy currents within conductive subsurface bodies, which then produce another magnetic field, known as the secondary field. This secondary field is comprised of an in-phase (real) and out-of-phase (quadrature) component. A receiver coil detects the compounding effects of the primary and secondary fields. The strength of the secondary magnetic field is a complex function of the electrical properties of the material, size, and geometry of the target, the operating frequency, and coil spacing and orientation. However, the relationship of the secondary magnetic field to all these variables becomes simplified when operating within a certain frequency range, in what is known commonly as "low induction number" conditions (Boaga, 2017; McNeill, 1980):

$$2\pi f \ll \frac{2}{\mu_0 \sigma s^2} \qquad 2\text{-}5$$

where μ_0 is the magnetic permeability of a vacuum ($4\pi x10^{-7}$ NA^{-2}) and s is the inter-coil spacing, and f and σ are as previously defined. The complex relationship of the secondary field and the theory of operation at low induction numbers has been well described (Boaga, 2017; McNeill, 1980). Under these conditions a reading of the average conductivity between the ground conductivity meter and its effective depth of penetration, known as apparent conductivity, can be calculated from the ratio of the secondary to the primary field (Boaga, 2017; McNeill, 1980):

$$\sigma_a = \frac{4}{\omega \mu_0 s^2} \left(\frac{H_s}{H_p} \right)_{Quatrature\ Component} \qquad 2\text{-}6$$

where σ_a is the apparent conductivity, ω is the angular frequency, H_s and H_p are the quadrature components of the secondary and primary field respectively, and all other variables are as previously defined.

The effective depth of investigation for a given ground conductivity meter is referred to as the skin depth and is equal to the depth at which the primary field strength becomes 1/e of its original value (Böhm et al., 2015; Burger et al., 2006a; Godio and Naldi, 2009; Monteiro Santos et al., 2006; Wilt et al., 1995). EM waves lose energy as they travel through the subsurface due to geometric spreading, wave scattering due to changes in electrical properties, and energy absorption by the geologic material (Burger et al., 2006a). Attenuation is a function of the conductivity, dielectric permittivity, and magnetic permeability of the material, given by the following relationship:

$$\alpha = 1690\left(\frac{\sigma}{\sqrt{\varepsilon_r}}\right) \qquad 2\text{-}7$$

$$\alpha = 1690\left(\frac{\sigma}{\sqrt{\left(\frac{\mu}{\epsilon_r}\right)}}\right) \qquad 2\text{-}8$$

where α is the attenuation factor, and all other variables are as previously defined. Here Equation 2-7 and 2-8 describe the behavior of non-magnetic and magnetic material, respectively (Burger et al., 2006a; Everett, 2013a).

In general, rock-forming materials are poor conductors, and as a result, ions in pore water typically govern apparent conductivity measurements. However, so long as enough contrast exists, EMI can be used to delineate conductive or resistive targets. Some examples of targets that can be identified

through EMI geophysics include permafrost zones, caves, crystalline rock deposits, saltwater intrusions, clay lenses, archeological structures, buried metal objects, and inorganic and organic contaminant plumes (Everett, 2013b).

2.2.2.2 Research Gaps in EMI Geophysics

While most EMI surveys provide qualitative information, some empirical relations have been developed to provide quantitative data. For instance, Zia et al. (2010) showed the use of two models, a spatial regression model and the Dual Pathway Parallel Conductance (DPPC) model to predict soil properties from EMI survey results. While the various predicted parameters were generally in good agreement with measured values, the best fit parameter only had an R^2 value of 0.89, showing the room for improvement. A recent review by Boaga (2017) agrees with the notion that there is still much potential to improve quantitative EMI relationships to determine hydrogeologic parameters. Boaga highlights the fact that advancements in inversion algorithms have aided in improving such predictive models, but many of the developed relationships remain empirical or site-specific.

Like GPR, one of the largest drawbacks for EMI geophysics is the issue of non-uniqueness. Often interpretations are made based on historical land use or using other site characterization techniques. In a study by Monteiro Santos et al. (2006), for instance, a conductive anomaly was attributed to leachate contamination since it could not be attributed to any known geological feature. This guided groundwater sampling, which confirmed the presence of landfill leachate, this type of elimination process to guide further analysis or draw conclusions is typical in EMI interpretation (Monteiro Santos et al., 2006). As another example, both resistive and conductive anomalies have been attributed to hydrocarbon contamination (Atekwana et al., 2000; Delgado-Rodríguez et al., 2014; Estella a et al., 2002). Other issues can arise if concentrations of a contaminant are too low to significantly alter the

electrical properties in the subsurface or if the contaminant zone is too thin to detect. Thus, there is still potential to improve the sensitivity of EMI devices to better understand the electrical response to specific contaminants, or potentially to artificially enhance contrast subsurface.

2.2.2.3 NPs as Imaging Contrast Agents for EMI Geophysics

To date, no practical use of NPs as imaging contrast agents for EMI geophysics has been reported. However, NPs have been assessed as imaging contrast agents for electromagnetic measurements at the laboratory scale and through modeling efforts. Burtman et al. (2015) show the addition of conductive organic polystyrene sulfonate and semi-conductive inorganic NPs (Fe_3O_4, Fe_2O_3, NiO, Al_2O_3) to samples of Saudi Arabian carbonate reservoir rocks, as well as to artificial rocks, to reduce complex resistivity measurements. The addition of these NPs produces a significant spectral induced polarization effect. It is concluded that NPs paired with electromagnetic measurement techniques could provide new possibilities for monitoring fluid movements in reservoirs.

NPs have also been modeled as conductive and magnetic (or “ferrofluid”) slugs to influence cross-well electromagnetic tomography measurements. Rahmani et al. (2015, 2014) show the propagation and vertical boundaries of a magnetic slug can be sensed before the arrival at an observation well.

2.2.3 Magnetic Susceptibility

2.2.3.1 Theory and Fundamentals

Magnetic geophysics devices induce magnetic fields in the subsurface and make use of manometers to measure small local variations in the Earth’s magnetic field due to differences in the magnetic properties of subsurface material. When a material becomes subject to a magnetic field it

becomes magnetized to an extent that is proportional to the applied field given by the following relationship:

$$\mathrm{M} = \chi \mathrm{H} \qquad 2\text{-}9$$

where *M* is the induced magnetization, *H* is the applied magnetic field, and χ is the magnetic susceptibility (MS). MS is a unitless constant of proportionality that is a measure of a material's tendency to become magnetized when exposed to a magnetic field. It is like magnetic permeability, which describes the ability of a medium to form a magnetic field, and is related mathematically by:

$$\mu = \mu_0(1 + \chi) \qquad 2\text{-}10$$

where μ is the magnetic permeability of a given material, μ_0 is the permittivity of a vacuum. The terms are very similar in definition, but MS is commonly reported for magnetic geophysics.

Most geologic materials possess a magnetic moment of zero, but when exposed to a magnetic field can either develop a net positive or negative (i.e., in line with or opposed to the applied magnetic field) value of magnetization (and thus MS) depending on how the magnetic domains align. Materials where domains do not alight perfectly parallel but have a net positive magnetization are termed paramagnetic, while materials with negative magnetization are termed diamagnetic. In some materials, such as iron, the magnetic domains align perfectly parallel within a material when subject to a magnetic field. If these domains all align in the same direction the material is known as ferromagnetic, if they align in parallel but opposite directions such that the resulting magnetic moment is zero the material is known as anti-ferromagnetic, and if domains parallel but opposite such that there is still a resulting magnetic moment the material is known as ferrimagnetic. Ferromagnetic materials will have the highest

values of MS, followed by ferri-, para- and diamagnetic, respectively. While ferromagnetic materials would have the most significant values of MS, they do not occur naturally on Earth (Burger et al., 2006b; Telford et al., 1990). Diamagnetic and paramagnetic rocks or minerals have very low MS values, meaning they do not typically provide enough contrast to be detected for subsurface delineation (Burger et al., 2006b; Telford et al., 1990). Thus, ferrimagnetic materials are the typical target for magnetic geophysics. The most commonly occurring ferrimagnetic materials are magnetite, maghemite, and titanomagnetite. Often the MS response of a subsurface target is directly related to its magnetite content. Typical ranges of magnetic susceptibilities for various geologic materials can be found in (Telford et al., 1990).

Magnetic fine-grained particles are understood to exist in four possible domain states (see review on environmental magnetism by Liu et al. (2012)). Larger particles (greater than approximately 100 nm), which can form multiple magnetic domains are termed multidomain grains (MD). In comparison, smaller particles may form one single magnetic domain and are termed single domain grains (SD). Some particles behave in a transitional state between MD and SD behavior, in which a signal domain is still present but “fans out”. Such particles are termed pseudo-single domain grains (PSD). Finally, in very small SD grains, the magnetic domain can change orientation as it is dominated by thermal fluctuations. Particles that experience this behavior are termed superparamagnetic grains (SP). An understanding of these behaviors is useful in quantifying grain size, mineralogy, or even the genesis of some magnetic minerals (Ameen et al., 2014; Emmerton et al., 2013; Rijal et al., 2012).

2.2.3.2 Research Gaps in MS Geophysics

The most apparent drawback of magnetic geophysics is the limited range of geologic materials that can be detected. Magnetic geophysics will not be a useful tool to delineate contaminants unless the contaminant possesses magnetic properties that are significant enough to contrast the background

geologic material. Targets must be made of magnetic metals or typically be related to an increased concentration of magnetite. For instance, magnetic anomalies have been correlated to the presence of PHC contamination (Aldana et al., 2003; Foote, 2007; Menshov et al., 2016, 2015; Rijal et al., 2012). however, the cause of this anomaly is still not fully understood. It has been suggested that the presence of PHCs enhance the activity of iron-reducing bacteria to produce magnetic minerals such as magnetite (e.g., Batt et al., 1995; Beaver et al., 2016; Emmerton et al., 2013; Klueglein et al., 2013; Menshov et al., 2016, 2015; Rijal et al., 2012). Emmerton et al. (2013) conducted an extensive study that found a correlation between biodegradation processes and magnetic properties in oil-bearing geologic media. However, Porsch et al. (2014) found that while the presence of a mobile organic carbon source did increase the activity or iron-reducing bacteria leading to the production of magnetite (and enhanced MS) when bioavailable iron was available, a hydrocarbon source did not produce better results than lactate/acetate as a carbon source. Further, Ameen et al. (2014) concluded that bioavailable iron had no significance to the formation of magnetite.

Magnetic geophysics also suffers from the issue of nonunique qualitative information. For instance, in cases where magnetic geophysics is used to delineate PHC contamination, the results must be paired with other methods to confirm that the magnetic anomalies are indeed due to PHC contamination rather than some other magnetic target (Aldana et al., 2003; Rijal et al., 2012). There is still a research need to study the relationship between MS and various contaminants, with PHCs as one example. Alternatively, there is a potential gap to increase the contrast between the targets of a magnetic geophysics investigation and the background geologic material, which could result in an ability to obtain unique or even quantitative results.

2.2.3.3 NPs as Imaging Contrast Agents for MS Geophysics

The use of NPs to alter the magnetic susceptibility of a medium they are in has been studied both at the lab-scale and through modeling efforts for applications such as reservoir characterization, increasing imaging contrast of proppants, delineating hydrocarbon contamination, and determining nZVI concentrations. (Chanzy et al., 1996; Estella a et al., 2002; Hu et al., 2016; Klueglein et al., 2013).

Numerical simulation by Rahmani et al. (2014) assessed the use of magnetic susceptibility tomography for the sensing of superparamagnetic NPs in both single well and Crosswell applications. It was found that magnetic NPs can change magnetic susceptibility measurements, with the sensitivity of magnetic measurements being most significant near the source and receiver (or near the wellbore for single well simulations) but less significant in the inter-well regions (for cross-well simulations). The magnetic susceptibility was independent of frequency when measurements were taken at low induction numbers.

Batch laboratory experiments by Morrow et al. (2015) demonstrated the use of nanomagnetite (nMag) to enhance the magnetic signature if present in sufficient concentrations, with higher levels of paramagnetic minerals in the background material requiring more substantial quantities of nMag. While this author suggests that this is evidence supporting the use of nMag mixed in proppant for fracking applications to better sense the nature of fractures, it also provides evidence to suggest nMag could act as a contrast agent for environmental geophysical applications if it were introduced in concentrations large enough to increase the magnetic signature relative to the background paramagnetic mineral concentrations and the magnetic susceptibility of a target contaminant.

At a larger scale, using an equilateral triangular box with lengths of approximately 4 m and height of approximately 1.5 m, Buchau et al. (2010) also demonstrated the application of MS for NP

sensing. They measured the MS before and after the injection of nZVI and found small (~0.01 SI) changes in susceptibility post-injection. The authors highlight the need for MS equipment to be highly sensitive and stable, as a small concentration (5.5 g/L) of nZVI and specialized sensors were used for these experiments. A gap still exists to determine if higher concentrations could be detected with conventional field MS devices.

Current field magnetic susceptibility meters can be as sensitive as 10^{-7} SI (ex: KT-20 Magnetic Susceptibility Meter (Terraplus, 2013)). The magnetic susceptibility for a range of geologic material can be found in Appendix A-2. Table 2-1, comparatively, shows the magnetic susceptibility of various NPs reported in literature. Based on these tables, nanomaterials do exist that could potentially act as contrast agents for some geologic materials (nMag in sedimentary material, for example).

Table 2-1: Magnetic susceptibility of various nanoparticles reported in literature.

Nanoparticle	MS measured	Value (units)	Reference
$MnFe_{2-x}Ag_xO_4$	Mass Specific	$1x10^{-5}$-$4.5x10^{-5}$ (m^3/kg)	(Aslibeiki et al., 2013)
Co/Au	AC Susceptibility	0.04-0.065 (N/A)	(Hrubovčák et al., 2015)
Au-Fe_3O_4	AC Susceptibility	$10x10^{-4}$ -$4x10^{-2}$(N/A)	(Frey et al., 2009)
Citrate- Fe_2O_3	SQUID/VSM	0.04-8.9 (N/A)	(Yoon et al., 2016)
SP Magnetite	AC Susceptibility	0.017-0.019 (N/A)	(van Berkum et al., 2013)
Magnetite	AC Susceptibility	0.1-0.76 (N/A)	(van Berkum et al., 2013)
Cobalt Ferrite	AC Susceptibility	0.01-0.22 (N/A)	(van Berkum et al., 2013)
Magnetite	AC Susceptibility	$1x10^{-4}$-0.2	(Allia and Tiberto, 2011)
Magnetite	Not specified	0.016-0.245	(Ali-zade, 2011)

2.2.4 Nuclear Magnetic Resonance

2.2.4.1 Theory and Fundamentals

The key physical property that NMR geophysics makes use of is the magnetic spin of atoms. Magnetic spin is an intrinsic property of atoms that is described by angular momentum and associated magnetic moment. NMR geophysics specifically measures responses of the spin of hydrogen protons in water. Although this is sometimes visually depicted by the protons rotating about some axis, the angular momentum and magnetic moment exist without physically rotating (Behroozmand et al., 2015; Hertrich, 2008). In the absence of any magnetic field, the spin magnetic moments will be randomly oriented. Conversely, when in a static magnetic field, such as the Earth's Magnetic field, hydrogen protons will precess about the magnetic field at a frequency known as the Larmor frequency. In this case, at thermal equilibrium, the alignment of the spin magnetic moments will be such that a small net magnetic moment will be generated in the field direction (Behroozmand et al., 2015; Hertrich, 2008). The Larmor frequency is given by:

$$f_L = \frac{\omega_L}{2\pi} = -\frac{\gamma|B_0|}{2\pi} \qquad 2\text{-}11$$

where ω_L is the Larmor angular frequency, γ is the proton gyromagnetic ratio, and B_0 is the static magnetic field.

Similar to other geoelectric methods, NMR geophysics makes use of alternating current to generate an energizing magnetic field. The total energy induced in the subsurface is called the pulse moment, often denoted as q (Behroozmand et al., 2015; Hertrich, 2008). In surface NMR methods, the Earth's magnetic field acts as the static field, but borehole NRM devices generate their own static field as well as the induced field. The perpendicular component of the generated field, in comparison to the static field, causes protons to become excited and tilt away from the static field. When this field is turned off, excited protons will transfer energy to surrounding mater through a process known as relaxation, in which the protons precess around axes both parallel and perpendicular to the static magnetic field. The relaxation time around the parallel axis is often denoted as T_1, while the relaxation time around the perpendicular axis is denoted as T_2 (Behroozmand et al., 2015; Hertrich, 2008). This precession generates a small alternating current allowing the amplitude and relaxations times to be measured by receiver coils.

NMR relaxation times are influenced by several factors such as viscosity, temperature, the presence of paramagnetic material, and pore size (Bloembergen et al., 1947; Brownstein and Tarr, 1979; Senturia and Robinson, 1970). In general, relaxation times tend to decrease with increasing fluid viscosity (Bloembergen et al., 1947). The combined effects of the presence of paramagnetic sites within soil grains (such as manganese (II) or iron (III)), as well as the area to volume ratio of pore space, are termed surface relaxation (Behroozmand et al., 2015; Brownstein and Tarr, 1979; Hedberg et al., 1993; Senturia and Robinson, 1970). The amplitude of NMR signals is related to the number of hydrogen

atoms present, because of this NMR can be used to both distinguish fluids and quantify their volumes (Bloch, 1946). One of the main benefits of NMR geophysics is the ability to obtain quantitative as well as qualitative information of the subsurface. Typical uses of NMR geophysics include determination of water content, estimation of pore-size distributions, estimating hydraulic conductivity, petroleum exploration, contaminant delineation and quantification, and biogeophysical applications. Many of these, as well as a list of relaxation times for various natural and synthetic geologic material at different Larmor frequencies, are discussed in detail by (Behroozmand et al., 2015).

2.2.4.2 Research Gaps in NMR Geophysics

NMR geophysics is very sensitive to hydrogen protons, and as such, to water content. This sensitivity allows the method to provide both qualitative and quantitative hydrogeologic information and has found use in groundwater delineation, detection of unfrozen sediments below permafrost zones, estimation of hydraulic conductivity, identifying differences in formation conductivity, and determining water content (Behroozmand et al., 2015; Parsekian et al., 2013; Shushakov, 1996; Walsh, 2008). Since NMR relaxation times are affected by the media surrounding the protons, it is also possible to use NMR geophysics to delineate contaminants in the subsurface. For example, studies have successfully used NMR to distinguish gasoline, diesel, toluene, crude oil, and TCE, in various geologic material (Bryar and Knight, 2008, 2003; Fay and Knight, 2016; Hedberg et al., 1993). However, it has also been shown that the response of NMR to the presence of the contaminants is complex and is dependent on the background material (Bryar and Knight, 2003; Fay and Knight, 2016). Since the NMR relaxation response is dependent on both the contaminant of interest and the material surrounding the contaminant, a research gap still exists to better understand these relationships. There is also a research

potential to artificially enhance or control the NMR response for a specific contaminant through NP technology.

2.2.4.3 NPs as Imaging Contrast Agents for NMR Geophysics

There exists a potential to use NPs as contrast agents for NMR geophysics since relaxation times of hydrogen protons are influenced by factors such as the surface charge or magnetic properties of the surrounding material. Several studies have already begun to assess the influence of NPs on NMR in aqueous and in geologic media (Klueglein et al., 2013; Medvedeva et al., 2014; Zhu et al., 2016).

Medvedeva et al. (2014) assessed the effect of nanopowder magnetite suspended in water at various concentrations on the T_2 relaxation times of NMR measurements. Their results show that T_2 relaxation times decrease with increasing magnetite. However, the authors note an increasing uncertainty in T_2 measurements with increasing magnetite concentration due to the rapid aggregation of the nanopowder particles in the presence of the magnetic field generated by the NMR device. This effect could pose an issue for field applications of magnetic NPs used to enhance imaging of electro-magnetic methods and shows a further need for research.

In addition to iron oxide, NPs Zhu et al. (2016) recently demonstrated the zirconia oxide (ZrO_2) NPs as a contrast agent for NMR sensing in sandstone cores. This laboratory experiment found that dispersions of ZrO2 NPs in the cores altered measurements of surface relaxivity. The effect on surface relaxivity was found to be complex, depending on many factors such as pH, the NPs surface charge, and the stabilizer used. While encouraging, these results are indicative that further research is still required to improve the use of NPs as contrast agents in subsurface NMR imaging.

2.3 X-ray CT as a Geophysical Tool

X-ray technology is commonly known to be a useful tool for medical diagnosis and security purposes; however, it has also found many uses in geological fields of study. Although not typically considered a geophysical method, X-ray CT bears several similarities to electromagnetic geophysical methods, the primary one being that the method functions by measuring changes in electromagnetic radiation as it passes through a material. X-ray CT is well studied as a geologic tool and has found nearly 40 years of use (e.g., Linley et al., 2019; Petrovic et al., 1982). Some surface and downhole X-ray fluorescent methods do exist (Ge and Li, 2019; Knoll, 2005; Stromberg et al., 2019); however, due to the shallow penetration depth of X-rays (0.01-10s of cm), they are not typically used for geophysical surveys.

2.3.1 Principles of X-ray CT

X-ray computed tomography (X-ray CT) is a non-destructive analysis tool that uses dedicated software to construct 3-D images, comprised of volumetric pixels (voxels) from multiple 2-D radiographs. X-ray CT scans can be performed in one of two ways. The X-ray source and detector can rotate around a fixed sample, as is typical for medical imaging applications, or the X-ray source and detector remain fixed while the sample rotates. Many laboratory set-ups used for geoscience applications make use of standard cone-beam micro-CT devices which use the later of the two mechanisms (Clausnitzer and Hopmans, 2000; Cnudde and Boone, 2013; Linley et al., 2019a; Taina et al., 2008; Zhang et al., 2019). The distinction between X-ray CT and micro-X-ray CT is based on the attainable spatial resolution for a given device and has been defined as 200 μm or less (Cnudde and Boone, 2013).

X-ray CT is based on the principle that X-ray radiation is attenuated to different degrees as it penetrates various materials. For a monochromatic beam, this phenomenon is mathematically described by Beer's law:

$$I = I_0 e^{-\int \mu(s) ds} \qquad 2\text{-}12$$

where I_0 and I are the incident and attenuated X-ray intensity (photons/unit time), μ is the linear attenuation coefficient, and s is the ray path (Cnudde and Boone, 2013; Taina et al., 2008). μ is an energy-dependent value that is determined primarily by the mechanisms of the photoelectric effect and Compton scatter (incoherent scatter), and Rayleigh scatter (coherent scatter). The photoelectric effect is described as the complete loss of photon energy as it is absorbed by an atom followed by the ejection of an electron. Compton scatter involves the partial transfer of the photon energy to an atom followed by the deflection of the photon, and Rayleigh scatter is defined as an event in which a photon is deflected by the interaction with an atom but retains all of its energy (Knoll, 2005). These effects are influenced by the density (ρ) and the effective atomic number (Z) of the material the X-rays are passing through, given by (Denison et al., 1997; Taina et al., 2008; Wellington and Vinegar, 1987):

$$\mu = \rho \left(a + \frac{bZ^{3.8}}{E^{3.2}} \right) \qquad 2\text{-}13$$

where a is a slightly energy-dependent coefficient, b is a constant, and E is the photon (or X-ray beam) energy. For situations where a mixture of atomic species is present the effective atomic number, Z_e, is given by:

$$Z_e^{3.8} = \sum f_i (Z)^{3.8} \qquad 2\text{-}14$$

where f_i is the fraction of electrons contributed by an element *i* over the total electrons in the structure for each element of atomic number Z.

2.3.2 Considerations for X-ray CT Experiments

Factors that can influence X-ray CT results include imaging artifacts, resolution limitations, and the dependence on operator interpretation. Micro CT scanners often produce a polychromatic X-ray beam, which influences the previously discussed principle behaviors of monochromatic beams. It can be seen from Equation 2-13 that lower energy radiation will be attenuated more easily than higher energy radiation. As a result, the makeup of a polychromatic beam contains less low energy radiation as is passes through a given material, describing an effect referred to as "beam hardening" (Clausnitzer and Hopmans, 2000; Cnudde and Boone, 2013; Taina et al., 2008). In X-ray CT processing, the 3-D images are produced based on a linear integration of the attenuation coefficient for each voxel. The beam hardening effect can thus influence scan results as the apparent attenuation of any given voxel is ultimately dependent on the attenuation of the surrounding material. Beam hardening can create a "cupping effect" in image results in which the outer edges of a sample show higher attenuation than the center (Hunter and McDavid, 2012). The effects of beam hardening can be mitigated through pre-filtration of the X-ray beam, or post-scanning software corrections (Hunter and McDavid, 2012). Other imaging artifacts include the cone-beam effect, which affects slices at the outer edges of the cone, streak artifacts that can occur due to the presence of metals or other highly attenuating substances, and artifacts caused by the movement of the sample (outside of the intended rotation) during scanning. See review by Cnudde and Boone (2013) for more details.

A second factor that must be considered is that any feature of a sample that is smaller than the voxel size will not be discretely detected but rather will influence the overall attenuation coefficient of voxels that contain or partially contain that given feature. This occurrence is known as the partial volume effect, which must be considered when selecting the resolution of a scan and when assessing X-ray CT image contrast.

A final issue is a dependency on the operator in X-ray CT image acquisition, processing, and interpretation. In X-ray CT software, such as VGStudio Max, for example, a histogram of grey-values is produced, which the user can interact with to remove or isolate voxels below or above certain grey values, which can be used to define various sample features (Volume Graphics GmbH, 2001). Unfortunately, this grey-value thresholding is dependent on user interpretation. Further, X-ray CT imaging Micro CT devices often allow the adjustment of settings such as tube voltage, tube current, exposure time, number of images scanned, magnification, and beam filtering. As illustrated by equation 2-13, X-ray attenuation depends on both the X-ray energy and the sample material. Thus the adjustment of the various scanning parameters can influence the linear attenuation coefficients and the grey-values that are generated to produce the image. Some researchers have developed algorithms or defined techniques to segregate elements of X-ray CT scans (see review paper by Taina et al. (2008)), but user-defined thresholding is also practiced. As of yet, no standard accepted protocol exists for micro-X-ray-CT imaging (Cnudde and Boone, 2013; Taina et al., 2008).

2.3.3 X-ray CT for Fluid Flow Tracking in Porous Media

Interest in X-ray CT as a tool for geoscience-related applications began as early as the 1980s and still exists today (e.g., Linley et al., 2019; Petrovic et al., 1982). The work presented in this thesis involves the use of X-ray CT for fluid flow applications, which will be further discussed here. For more

information regarding other uses of X-ray CT, the reader is referred to other sources (Cnudde and Boone, 2013; Taina et al., 2008; Zhang et al., 2019).

Water has a much higher X-ray attenuation relative to air and thus saturated, or partially saturated, systems can sometimes be more difficult to analyze depending on the objective. X-ray CT studies that assess fluid flow or other hydro-physical properties make use of high X-ray attenuating tracer solutions (referred to as imaging contrast agents) such as NaI or KI to enhance the contrast observed between wetting, non-wetting, and solid phases (Clausnitzer and Hopmans, 2000; Costanza-Robinson et al., 2008; Culligan et al., 2006; Porter et al., 2010; Zhang et al., 2019).

Clausnitzer and Hopmans (2000) successfully performed continuous X-ray CT scanning to visualize the transport of a NaI slug injected into a small saturated plexiglass flow cell (50 mm in length, 4.76 mm inner diameter) packed with glass beads (0.5 mm diameter). The experiment consisted of a 30 min period of water flow, followed by 90 min of NaI injection, and then 240 minutes of water flow. A thin section (0.44 mm vertical section) of the column was continuously scanned at a voxel resolution of 23 μm^3 during this process at a rate of ~ 20 minutes per scan, producing 16 scans. The edges of the 3-D cylindrical images produced were cut such that a cube remained for analysis. The authors note that a very low flow rate (0.1 mL/h) is required to ensure no temporal distortions occurred during the scanning process (i.e., to ensure that the NaI slug does not appear smeared or stretched in the final reconstructed 3-D image it must remain stationary for the duration of each complete X-ray CT scan). Clausnitzer and Hopmans (2000) used results from scanned capillary tubes filled with various concentrations of NaI and from the saturated glass bead column before NaI injection to develop a calibration method to quantify NaI concentrations from X-ray CT scans. They derived the flowing equation:

$$C(x) = \left[\frac{\mu(x) - \mu_{H_2O}}{u_{glass}(r) - \mu_{H_2O}(x)}\right] c_{equiv}(r) \qquad 2\text{-}15$$

where *C(x)* is the NaI concentration at voxel location *x*, μ is the effective attenuation coefficient, μ_{H2O} is the effective linear attenuation coefficient of the voxel before NaI injection, and $\mu_{glass}(r)$ and $C_{equiv}(r)$ are fitted functional expressions that describe the effective attenuation of the glass and the NaI concentration that has an effective attenuation equal to the glass for a given energy level and radius r away from the central axis. They obtained a relatively good fit (less than 4 g/L deviation) between experimental and measured data.

Recently, Zhang et al. (2019) also used X-ray CT to observe a NaI slug moving through an acrylic column (95 mm in length, 32 mm inner diameter) packed with melamine resin particles. The column was saturated with a 10% wt. NaCl solution to reduce any potential density effects between the injected 10% wt. NaI slug and the saturation solution. A 0.13 mL slug of NaI was injected into the column followed by 0.5 PV (dependent on the porosity of each column packed with various particle sizes of melamine resin particles) of NaCl with scans performed every 0.1 PV at a voxel resolution of 103 µm. Zhang et al. (2019) assessed the dispersion of the NaI plume as it transported through the column by identifying the wt. % concentrations in the 3-D scan images using a calibration curve related to the brightness of the CT images.

Other studies that have assessed fluid transport or hydro-physical properties in porous geologic media using X-ray CT usually do so by scanning before and after a particular alteration to the samples (such as before and after saturation or various degrees of drainage), but do not scan during transport. For example, several studies have used X-ray CT to assess air-water or water-NAPL interfacial areas at

different degrees of saturation by scanning samples at (or near) saturation and then again after a drainage event (Costanza-Robinson et al., 2008; Culligan et al., 2006; Porter et al., 2010). These experiments often used an iodide-doped saturating solution to increase the contrast between the air, solid, and NAPL phase. Further, many geologic X-ray CT fluid property studies have been performed on small sample sections (5.5 mm vertical slices or less) at fine resolutions (~10-17 µm voxels) (Costanza-Robinson et al., 2008; Culligan et al., 2006; Porter et al., 2010).

2.3.4 X-ray CT Imaging of Nanoparticles in Geologic Porous Media

Although the use of NPs as imaging contrast agents for X-ray CT is relatively common in the medical field, their use for such an application in the geoscience field is relatively new. Linley et al. (2019) recently demonstrated the use of iron oxide NPs as imaging contrast agents in silica sand samples. The iron oxide NPs used were coated with an amphiphilic block copolymer (Pluronic), which serves both to stabilize the NPs in and to allow for targeted binding to crude oil. Linley et al. (2019) demonstrated a clear, discernable contrast between silica sand and silica sand containing Fe_3O_4 NPs, and an apparent increase in contrast between crude oil impacted silica sand and crude oil impacted silica sand with bound NPs. These experiments were performed in dry conditions in 4.5 mL cuvettes. They found that the Fe_3O_4 NPs could be detected at concentrations as low as 1 mg/kg.

Chapter 3

Nanoparticles as X-ray CT Contrast Agents

3.1 Overview

The primary objective of this research is to evaluate the ability of X-ray CT to monitor the transport of engineered NPs in a saturated geologic porous medium at the column scale. The sub-objectives are as follows:

1. Establish NP solution contrast in an aqueous environment.
2. Establish NP solution contrast in a saturated porous medium.
3. Isolate and examine X-ray CT artifacts that may impact the use of NPs as imaging contrast agents in column tracer experiments.
4. Determine the effects of concentration and flow rate on X-ray CT contrast agent transport and monitoring.
5. Develop an appropriate methodology to assess the suitability of NP solutions as X-ray CT imaging contrast agents in a saturated porous medium through comparison to a known X-ray CT contrast agent.

The following experiments were performed using glass columns, an acrylic column, and in 4.5 mL acrylic cuvettes to achieve these objectives:

1. Placement of glass beads saturated with Fe_3O_4 NPs in the glass column via wet packing followed by X-ray CT scanning to determine NP contrast potential.
2. Injection of Fe_3O_4 NPs through a saturated glass column with multiple X-ray CT scans performed during NP migration.

3. X-ray CT scans between two cuvettes stacked on top of each other to determine the relative X-ray attenuation between two respective solutions.
4. Troubleshooting experiments performed in the packed and saturated acrylic column to examine a reoccurring X-ray CT artifact.
5. Injection of various concentrations of NaI into a packed and saturated glass column or cuvettes to determine the lowest concentration of NaI required to establish X-ray CT contrast.
6. Injection of three concentrations NaI through a packed and saturated glass column at three different flow rates to assess the use of X-ray CT to monitor the migration of a known contrast agent.
7. Injection of bismuth ferrite NPs through a packed and saturated glass column with multiple X-ray CT scans performed during NP migration.

An appreciation of the chronology is required to understand the experimental progression followed to meet the objective of this research. Fe_3O_4 NPs were initially utilized to achieve sub-objectives 1 and 2 due to their availability and previous success as X-ray CT contrast agents in dry porous media by Linley et al. (2019). X-ray scans of aqueous Fe_3O_4 NP suspensions in saturated glass columns, and the acrylic cuvette, both packed with glass beads, were conducted to determine the relative contrast and visibility in a processed X-ray CT image. It was revealed that the Fe_3O_4 NPs had a stronger X-ray attenuation relative to Milli-Q water, meeting sub-objective 1. However, early results also indicated that NP contrast could not be achieved in a saturated glass bead porous medium at any scale used in this work. During these early experiments, an X-ray CT imaging artifact was recognized in which a conical shape of X-ray attenuation contrast was observed. To achieve sub-objective 3, several troubleshooting

experiments were performed using an acrylic column in an attempt to isolate and eliminate the origin of this “conical effect” artifact. This artifact was determined to be the result of a sample misalignment issue within the X-ray CT system and may be eliminated where the difference in X-ray attenuation contrast is large enough. To assess the inability of the Fe_3O_4 NP solution to generate an observable X-ray attenuation contrast, and to respond to sub-objective 5 of this research, the NP solution was directly compared to a known X-ray contrast agent, NaI. First, NaI was used at the smallest scale (cuvette) to determine the minimum concentration of NaI required for contrast to be observed. Then, stacked cuvette contrast scans were then used to determine the relative X-ray attenuation relationship between NaI and Fe_3O_4 NP solutions. This evaluation revealed that the Fe_3O_4 NPs do not provide sufficient X-ray attenuation for contrast to be observed at any of the column scales. However, it did prove an effective method to assess the suitability of NP solutions as X-ray CT imaging contrast agents in a saturated porous medium, thus meeting the requirements of sub-objective 5. While a new NP solution, comprising of a higher atomic number element to increase X-ray attenuation, was under development, a series of NaI transport experiments were performed at various concentrations and flow rates to satisfy sub-objective 4. The flow rate was found to have little effect on the ability to monitor tracer movement using X-ray CT; however, evidence of viscous fingering due to gravity was observed due to the high concentrations of NaI used. Thus, it was determined that the density of a NP X-ray CT contrast agent solution must be considered. Finally, bismuth ferrite NPs (with a higher atomic number and thus a stronger X-ray attenuation than the Fe_3O_4 NPs) were synthesized, and the transport of these NPs through the packed and saturated glass column was successfully monitored with X-ray CT. This objective was achieved following a stacked cuvette comparison between the bismuth ferrite NP and NaI solutions, thus satisfying the requirements of sub-objective 5 and the overarching objective of this research.

3.2 Materials and Methods

3.2.1 Chemicals

The following chemicals were used as received:

- 1-Pentanol (≥ 99%; from Sigma Aldrich, St. Louis, MO, USA)
- Ammonium hydroxide (NH_4OH, 28-30% in water; from Sigma Aldrich, St. Louis, MO, USA)
- Bismuth (III) nitrate ($Bi(NO_3)_3$, ≥ 98.0%; from Sigma Aldrich, St. Louis, MO, USA)
- Dichloromethane (DCM, > 99%; from Sigma Aldrich, St. Louis, MO, USA)
- Ethanol (ACS grade, 99%; from Fisher Scientific, Hampton, NH, USA)
- Hexane (ACS grade; ≥ 98%; from Sigma Aldrich, St. Louis, MO, USA)
- Hydrochloric acid (37%; from Sigma Aldrich, St. Louis, MO, USA)
- Iron (III) chloride hexahydrate ($FeCl_3 \cdot 6H_2O$, > 99%; from Sigma Aldrich, St. Louis, MO, USA)
- Iron (III) Nitrate ($Fe(NO_3)_3$, ≥ 98%; from Sigma Aldrich, St. Louis, MO, USA)
- Iron (II) sulfate heptahydrate ($FeSO_4 \cdot 7H_2O$, > 99%; from Sigma Aldrich, St. Louis, MO, USA)
- Nitric Acid (HNO_3, ACS Grade >90 %; from Sigma Aldrich, St. Louis, MO, USA)
- Oleic acid (>90%; from Sigma Aldrich, St. Louis, MO, USA)
- Pluronic co-polymers P104, L62, and L121 (gifted by Brenntag, Essen, Germany, and BASF, Ludwigshafen, Germany)
- Potassium Hydroxide (KOH, ACS Grade ≥85%, pellets; from Sigma Aldrich, St. Louis, MO, USA)

- Sodium Bromide (NaBr >99%; from Sigma Aldrich, St. Louis, MO, USA)
- Sodium Hydroxide (NaOH, ≥ 98%; from Sigma Aldrich, St. Louis, MO, USA)
- Sodium Iodide (NaI > 99%; (from Sigma Aldrich, St. Louis, MO, USA)

3.2.2 Porous Media

The porous medium used in all column experiments was Sigma Aldrich G1145 150-212 µm acid-washed glass beads. The glass beads were acid-washed after being received to further remove any potential impurities. They were immersed in a beaker for 24 hours covered with aluminum foil containing enough 5 M nitric acid to submerge the beads and were stirred occasionally. Following these 24 hours, the beads were rinsed in deionized water until the pH of the DI water containing the submerged beads was ~ 7. Then the wet beads were placed in a drying oven at 237°C for a minimum of 3 hours. The density of the glass beads was estimated gravimetrically to be 1.46 ±0.02 g/cm^3 (see Appendix B-3) which is in agreement with other sources that have cited the density of 150-212 µm glass beads (Nsugbe et al., 2016)

3.2.3 Fe_3O_4 NPs

The Fe_3O_4 NPs used in this research were synthesized following the method provided by Linley et al. (2019). A molar ratio of 2:3 ($FeSO_4$:$FeCl_3$) of $FeSO_4 \cdot 7H_2O$ and FeCl3$\cdot 6H_2O$ were added to deoxygenated water, followed by the addition of NH_4OH to achieve concentrations of either 4 or 0.22 mol/L. The solution was stirred for 1 hour at 70°C followed by an additional hour of stirring at 90°C under flowing N_2 to purge NH_3 gas. The resultant black precipitate was recovered by magnetic decantation, rinsed by deoxygenated Millipore DI water, and dried under flowing N_2. The dried NPs were then added to a mixture of 1% oleic acid in hexane (v/v) such that the NP concentration was 90 g/L. This

solution was sonicated for 10 minutes, and the suspension was added at 10% (v/v) to aqueous Pluronic copolymer(s) followed by another 30 minutes of sonication. Finally, the emulsified NPs were separated over 48 h using a separatory funnel. Analysis performed by Linley et al. (2020) indicated that this method produces spherical NPs with an average diameter of 7 ± 2 nm. Higher concentrations of the stabilizing surfactant were required when modifying this method to generate higher concentration NP solutions (Linley et al., 2020).

3.2.4 Bismuth ferrite NPs

Bi-metallic bismuth ferrite NPs were developed as NPs comprising of higher atomic number elements relative to Fe_3O_4 NPs were required. The synthesis of the bismuth ferrite NPs involved the production of Fe-oleate and Bi-oleate. To create the Fe-oleate, 21.46 mL oleic acid and 20 mL ethanol were mixed in a beaker until fully dissolved and then added to a round bottom (RB) flask containing 10 mL of 264 g/L NaOH while stirring. 6.464 g $Fe(NO_3)_3 \cdot 9H_2O$ was dissolved in 10 mL Milli-Q water and added to the RB flask while stirring. 20 mL of hexane was added to the solution in the RB flask, which was then fitted with a reflux condenser and heated to 85°C in an oil bath while stirring slowly for 1 hour. The solution was left to cool and separate. Then the bottom aqueous phase was removed using a Pasteur pipette. The solution was washed thrice with 20 mL Milli-Q water, 5 mL of ethanol, 5 mL of hexane, and refluxed for 30 minutes. Once washed, 15 mL of 1-pentanol was added, and the remaining hexane was evaporated under heat with no reflux for 30 minutes. The remaining solution was stored in an appropriately sized vial and placed in a fridge (4°C) until used.

To create the Bi-oleate a mixture of 20 mL Milli-Q water, 40 mL of ethanol and 60 mL of hexane was prepared in an Erlenmeyer flask and added to 2.192 g of Na-oleate and 0.5821 g $Bi(NO_3)_3 \cdot 5H_2O$ in an

RB flask while stirring vigorously in an oil bath at a temperature of 70°C. Then 2 mL of 1.8 M/L KOH was added by pipette to the RB flask and left to stir under reflux for 4 hours at 70°C. The RB flask containing the solution was then removed from the oil bath and allowed to cool before transfer into a separatory funnel. The bottom aqueous phase was discarded, and the organic phase was returned to the RB flask. 30 mL of Milli-Q water, 7.5 mL of hexane, and 7.5 mL of ethanol was added to the remaining organic phase and boiled for 30 minutes under reflux. The solution was left to cool, transferred to the separatory funnel, and the aqueous phase was again discarded. The organic phase was poured back into the RB flask, 15 mL of 1-pentanol was added, and the solution was heated to 85°C in an oil bath to evaporate the remaining hexane. The temperature was increased by 10°C each time no boiling/bubble formation was observed until a temperature of 115 °C was reached. The final solution was left to cool and was stored in an appropriately sized vial that was placed in a fridge (4°C) until used.

Once both oleate solutions were prepared, an equimolar amount of each (typically ~20 mL of Bi-oleate and ~2.5 mL Fe-oleate) were added to a 125 mL Teflon-lined stainless steel reaction vessel, followed by 32 mL of 1-pentanol and 27 mL of Milli-Q water before sealing the reaction vessel, shaking vigorously, and placing in an oven at 180°C for 10 hours. The product was left to cool, decanted into 50 mL centrifuge tubes, and centrifuged at ~1.28 xg for 5 minutes. The excess 1-pentanol and water were then decanted, leaving the brown solid at the base of the centrifuge tubes. The NPs were then washed with ethanol or hexane and re-centrifuged an additional five times before being stored in glass vials for use.

3.2.5 X-ray CT Characterization

X-ray CT is a method in which multiple X-ray images of a sample are obtained at different angles (achieved either using a fixed X-ray source and detector with a rotating sample, or a fixed sample and a rotating X-ray source and detector) and are digitally reconstructed by computer algorithms to produce a 3-D image of the sample being scanned. For this research, the term "X-ray CT Scan" is defined as the complete collection of X-ray images obtained on a sample that is to be reconstructed, the term "raw images" is used to describe the individual images collected during an X-ray CT scan, and the term "processed image" or "3-D image" refers to the final 3-D reconstruction of the sample. X-ray CT scans were completed using an open directional high-power micro-focus X-ray tube (240 kV, GE Phoenix v|tome|x m compact micro CT system) equipped with a GE DXR detector array. This device is the same as the one used by Linley et al. (2019). The X-ray scan settings used varied between experiments. The acceleration voltage used in this study ranged from 80-150 kV, the beam current ranged from 80-150 µA, and the voxel (volumetric pixel) size ranged from approximately 29.06-141.96 μm^3. 1000 images were obtained for nearly all scans at a timing of 333 ms per image. The number of images taken during scanning influences the resolution of the processed X-ray CT image, however, it has little impact on whether a contrast (i.e., a difference in X-ray attenuation) between two solutions or materials is discernable. Thus, for experiments where the resolution was not important, such as for liquid to liquid static contrast scans performed in 4.5 mL cuvettes, "quick scanning" was performed by decreasing the number of images obtained to 100. The X-ray CT scanning parameters used for each experiment are listed in Table 3-1. The raw images from each scan were processed using Volume Graphics Software (VGStudio Max version 2.2). The scans were processed using beam hardening correction factors between 5.5 and 9.7.

Each voxel in the processed X-ray CT image is assigned a grey-value representative of its X-ray attenuation, with higher grey-values being assigned to more strongly attenuating materials. A grey-value histogram is produced as part of the 3-D X-ray CT image processed by VGStudio Max. By changing the grey-value threshold, the user indicates which voxels should be displayed and can adjust the image to show a contrast between areas of high and low X-ray attenuation. For example, consider a highly attenuating material “A” with a grey-value of 100, and a slightly attenuating material “B” with a grey-value of 10. Choosing a grey-value threshold of 50 would result in only voxels of material “A” being displayed, selecting a threshold value of 200 would cause neither to be displayed, and choosing a threshold value of 1 would cause both to be displayed. Thus, a comparison of relative X-ray CT attenuation can be made between two NP suspensions, or between a NP suspension and another fluid such as water, by determining a grey-value threshold that causes the voxels of only one of the suspensions to be displayed.

Table 3-1: X-ray CT scanning parameters used for all experiments.

Experiment Description	Voltage (kV)	Current (µA)	Voxel Size (µm^3)	Images	Timing (ms)	Scan Time (min)
Fe_3O_4 NP Contrast Scan 1	150	150	93.0	1000	333	25
Fe_3O_4 NP Contrast Scan 2	150	150	110.9	1000	333	25
Fe_3O_4 flow-through and scan experiment*	150	150	140.4	1000	333	25
Fe_3O_4 NP contrast Scan in acrylic column	100	100	97.6	1000	333	25
Glass column NaI contrast scans	100	100	142.0	100	333	2.5
NaI lower detection limit scans*	100	100	142.0	1000	333	25
Static cuvette contrast scan (water to Fe_3O_4 NPs)	80	80	33.9	1000	333	25
Static cuvette contrast scan (water to Fe_3O_4 NPs in saturated glass beads)	80	80	34.0	1000	333	25
Static cuvette contrast scan (Fe_3O_4 NPs to NaI, ~15g/L to 15 g_I/L)	100	100	97.6	100	333	2.5
Static cuvette contrast scan (bismuth ferrite NPs to NaI, ~15g/L to 15 g_I/L)	100	100	97.6	100	333	2.5
NaI flow-through and scan experiments (i.e. all IFT experiments) *	100	100	142	1000	333	25
Bismuth ferrite NP flow-through and scan experiments*	100	100	142	1000	333	25

* Scanning parameters were constant across all scans for given experiments.

3.2.6 Column Design

Two aspects required consideration when designing a column for this work: the material, and the dimensions. Lower density column materials were preferable to reduce background X-ray attenuation by the experimental apparatus. Additionally, transparent materials were desirable to enable visualization of the coloured NP suspensions as they propagated through the columns. The column dimensions were constrained by the scanning zone of the X-ray CT system, and the column structure should maximize uniform laminar flow (i.e., minimize preferential flow paths).

The maximum scanning height of the X-ray CT system is approximately 15 cm, and the maximum width was non-restrictive. Uniform laminar flow-through a column is influenced by factors including inlet and outlet conditions, diameter, length, diameter to length ratio, the ratio of column diameter to grain size, and wall effects. Table 3-2 outlines recommendations for column design found in the literature that was followed in this work.

The primary column design was made of glass (15.24 cm in length, 2.54 cm internal diameter) with threaded caps at each end containing Teflon seals and a built-in mesh to distribute flow at the inlet/outlet (see left-hand side of Figure 3-1). A secondary column design made of acrylic (10.16 cm in length, 0.9 cm internal diameter) was constructed to reduce background X-ray attenuation compared to the glass walls of the primary column design (see right-hand side of Figure 3-1). This column was also used to troubleshoot a potential X-ray CT scanning and processing issue that was recognized during experiments using the glass column. A custom Styrofoam support was built to mount the acrylic column in the X-ray CT machine. Both columns approximately satisfied the 15 cm maximum height restriction imposed by the X-ray CT machine and thus could be scanned in (or near) their entirety. The materials

used in both columns are comprised of elements with lower atomic numbers than iron (glass = SiO_2 [Si=14, O=8], acrylic $C_5O_2H_8$ [C=6, O=8, H=1], relative to iron [Fe=26]) and thus theoretically should allow for a detectable contrast between the column and the NPs (See Equation 2-13 (Denison et al., 1997; Taina et al., 2008; Wellington and Vinegar, 1987)). Acrylic is of a lower density than glass (the density of common glass =2.4-2.8 kg/m^3, the density of acrylic =1.19 kg/m^3 (Engineering ToolBox, 2009)) and thus allows for even less X-ray attenuation.

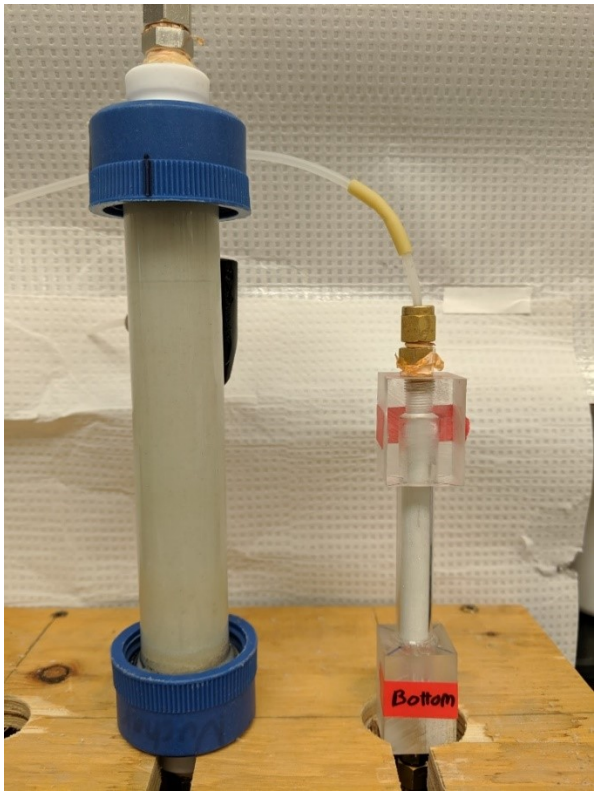

Figure 3-1: Large glass column (left) and small acrylic column (right). The glass column is 15.24 cm in length (excluding endcaps), has an inner diameter of 2.54 cm, and an external diameter of approximately 3.04 cm. The acrylic column has a length of 10.16 cm (including endcaps), an inner diameter of 0.9 cm, and an outer diameter of approximately 1.3 cm.

Table 3-2: Summary of column design recommendations found in literature, including justification and associated reference.

Recommendation	Justification	Reference
Introduce a baffle zone at the inlet and outlet of the column that is at least the length of the column radius.	Non-uniform flow can occur for lengths up to 2/3 the column radius at the inlet and outlets were a baffle is not present.	(Barry, 2009; Gibert et al., 2014)
Columns with diameters greater than 7.59 cm result in larger solute dispersivity than smaller columns	Columns with diameters greater than 7.59 cm result in larger solute dispersivity.	(Bromly et al., 2007)
Length to radius ratio > 3:1	Ensures there is at least a section of laminar flow.	(Barry, 2009)
Length to Diameter =>4:1	Minimizes the occurrence of sidewall flow.	(Gibert et al., 2014; Lewis and Sjöstrom, 2010)
Column to particle diameter ratio > 50:1	Wall effects are significant were column to particle diameter ratio is < 50:1	(Gibert et al., 2014; Mehta and Hawley, 1969)

3.2.7 Column Packing and Saturation

Dry packing was the primary method selected to fill the columns with the glass beads. However, a wet packing method was also used so the NPs could be placed at discrete locations in the column while maintaining saturated conditions. Wet packing was used in early experiments where the goal was only to establish a contrast between the saturated glass bead medium and the NPs using X-ray CT. When packing the glass and acrylic columns, approximately 2.5 cm and 1 cm of glass wool were packed just before the inlet and outlet, respectively, to act as a baffle to distribute flow.

All dry-packed columns were filled in 0.2 cm lifts (Oliviera et al., 1996). After the addition of each lift, the material was packed down manually using a rubber plunger (diameter of ~ 2.54 cm) for the glass columns and a wooden plunger (diameter of ~ 0.9 cm) for the acrylic column. Dry packed columns were flushed with CO_2 for approximately five minutes and then saturated from bottom to top with DI or Milli-

Q water until about 3 pore volumes were passed through the column to minimize the potential for entrapped air.

The wet packing method used was also based on recommendations by Oliviera et al. (1996). First, water (or NP suspension) was added into the column such that it raised the water level by approximately 0.25-0.5 cm. Then glass beads were sprinkled into the column while stirring slowly as the beads settled. This process was repeated until the column was completely packed.

3.2.8 Column Characterization

The hydraulic conductivity of the packed columns was estimated using a series of falling head tests based on the ASTM D5084-16a test method (ASTM International, 2016). The hydraulic conductivity was estimated in four separate glass columns, dry-packed with glass beads and saturated. Falling head tests were performed in triplicate for each column.

Two bromide tracer experiments were performed in glass columns, the first in triplicate and the second in duplicate. The first bromide tracer experiment referred to as Br-1, comprised of three columns run in parallel, Br-1-A, Br-1-B, and Br-1-C. For Br-1-A and Br-1-B, the flow was periodically stopped by shutting the inlet and outlet valves for ~35 minutes to mimic the time that would be required to perform an X-ray CT scan. Br-1 ran with a continuous bromide injection rather than a slug. The second experiment, referred to as Br-2, comprised of two glass columns, Br-2-A and Br-2-B, and was performed using continuous flow. The conditions for these experiments are summarized in Table 3-3. Note that, in trials where stop-flow time was incorporated, the porosity and dispersivity were calculated as though the flow was continuous.

The effective porosity of the packed glass columns was estimated based on modeled results from bromide breakthrough curves (BTCs) using an optimization platform, OSTRICH (Optimization Software Toolkit for Research Involving Computational Heuristics), developed by Matott (2013) coupled with 1-DUSAT, a solute transport model (Thomson, 2019). The diffusion coefficient for bromide used for 1-DUSAT modeling was assumed to be 1.18×10^{-9} m^2/s (Cussler, 2009).

Table 3-3: Summary of conditions for bromide tracer experiments.

Experiment	Flow Rate (mL/min)	Injection Concentration (mg_{Br}/L)	Injection Time (Min)	Sampling duration (min)	Interval Between Samples (min)
Br-1-A	0.36	500	27.66	4	2
Br-1-B	0.36	500	27.66	4	2
Br-1-C	0.36	500	Continuous	4	2
Br-2-A	0.8	500	5.5	2	2
Br-2-B	0.8	500	5.5	2	2

3.2.9 Experiments to Establish X-ray CT Contrast

3.2.9.1 Glass Column NP Contrast Scans

Two preliminary scans that assessed the use of Fe_3O_4 NP as X-ray CT imaging contrast agents in the packed and saturated glass column were performed. For the first contrast scan (referred to as Fe_3O_4 NP Contrast Scan 1), the glass column was wet packed with glass beads, however, rather than stirring, the column was placed on a shaker table (~0.035-0.142 xg). The beads were sprinkled into small lifts of water (approximately 0.5 cm) until the height of the beads in the column was about 7.6 cm from the bottom. This process was repeated, using 500 mg/L NP suspension instead of water, until the column was fully packed, resulting in a NP section that was also approximately 7.6 cm long. For the second

contrast scan (referred to as Fe_3O_4 NP Contrast Scan 2), the wet packing method was used to create several layers of glass beads saturated with varying concentrations of a Fe_3O_4 NP solution that were each separated by fitted septum disks. First, a 2.5 cm thick layer of beads in Milli-Q water was packed into the column, then a septum disk cut to the diameter of the column was placed above the bead layer. This process was repeated moving up the column with a second 2.5 cm thick layer of beads in Milli-Q, followed by five 1.3 cm thick layers of beads in 100, 200, 300, 400, and 500 mg/L NP solutions, respectively. Finally, the column was completed by adding two more layers of beads in Milli-Q water with lengths of 2.5 cm and 0.6 cm, respectively.

3.2.9.2 Acrylic Column NP Contrast Scans

A 6500 mg/L solution of Fe_3O_4 NPs was injected into an acrylic column that was dry-packed with glass beads and saturated with water. These NPs were injected at a flow rate of 0.35 mL/min until they were visible approximately 5 cm into the column (see Figure 3-2). X-ray CT scanning was then performed to investigate contrast.

This experiment was repeated substituting plastic pellets (cylindrical in shape, approximately 0.5cm in length, 0.2 cm in diameter, density < 1 g/cm^3) instead of glass beads as the column packing material (to lower background X-ray attenuation). These pellets were dry-packed into the column, and X-ray scans were performed before and after NP injection.

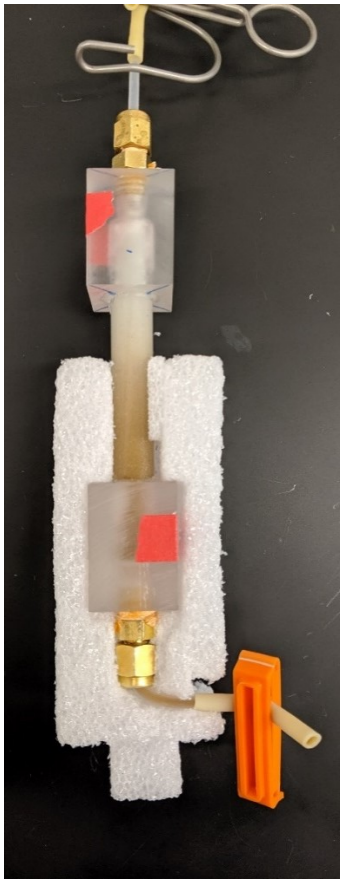

Figure 3-2: Acrylic column in Styrofoam holder showing injected NP solution (brown).

3.2.9.3 Glass Column NaI Contrast Scans

Various concentrations of NaI were injected into dry-packed glass columns saturated with Milli-Q water to determine if X-ray CT contrast was attainable. The NaI was injected at 0.35 mL/min for approximately 20 minutes (corresponding to a slug that was approximately 5 cm long), followed by about 10.5 minutes of Milli-Q water to ensure the slug would be visible by X-ray CT scanning in the bottom or center of the column. The lowest concentration of NaI required to obtain contrast (referred to as the NaI lower detection limit) was determined by repeating contrast scans using decreasing concentrations of NaI until X-ray attenuation appeared uniform along the entire column. A grey-value

threshold was manually selected for each processed X-ray CT image to show blue and green sections of contrast, representing areas of higher and lower X-ray CT attenuation, respectively.

3.2.10 Static Cuvette Contrast Scans

X-ray CT contrast between water and NP suspension was established by scanning stacked cuvettes supported by a custom-built Styrofoam holder. Four X-ray CT cuvette contrast scans were performed between solutions of Fe_3O_4 NPs and water; one between Milli-Q Water and a 6500 mg/L Fe_3O_4 NP solution, one between Milli-Q water and a 650 mg/L NP solution, one between two cuvettes containing glass beads wet packed with Milli-Q water and a 6500 mg/L solution respectively, and lastly one between two cuvettes containing glass beads wet packed with Milli-Q water and a 650 mg/L Fe_3O_4 NP solution respectively. Similar static cuvette contrast scans were also performed between solutions of Fe_3O_4 NPs and various concentrations NaI, as well as between solutions of bismuth ferrite NPs and NaI.

3.2.11 Column Operation: Flow-through and X-ray CT Scan Experiments

Due to space restrictions and the risk of water damage, conducting column flow within the X-ray CT instrument was not possible. Instead, during NP or NaI transport and X-ray CT scan experiments, the flow was periodically stopped, and the column disconnected from the main tubing so that the column could be placed in the X-ray CT. To achieve this, three-way ball valves were attached at the inlet and outlet of each column that allowed the flow to bypass the column when required. Before shutting off the flow, the inlet bypass valve was closed, followed by the outlet valve. The pump was then shut down and all necessary tubing was clamped to prevent leakage. After each scan was completed, all appropriate tubing was reconnected, the pump was turned back on, and the column flow was resumed by opening both inlet and outlet valves. This setup was used for both the glass and acrylic column

experiments. Between 6-8 scans were obtained for all NP and NaI transport and X-ray CT scan experiments.

A MasterFlex®L/S® peristaltic pump was used in all column transport experiments. The flow rate was measured before each test directly from the connected tubing before being attached to the column. Additional flow rate measurements were also made from this tubing when it was disconnected from the column to allow for X-ray CT scanning to be performed.

3.2.11.1 Fe_3O_4 NP Transport and X-ray CT Scans

NP transport experiments were designed using the glass column to confirm the transport of the Fe_3O_4 NPs through the glass beads. Two glass columns were dry-packed with glass beads and saturated. Then a 500 mg/L Fe_3O_4 NP slug was injected into each column at a flow rate of 0.35 mL/min for approximately 20 minutes. Effluent samples were collected for four minutes at an interval of two minutes between each sample. In NP transport experiments where X-ray CT scanning was not performed the column was still periodically disconnected from the flow system using the methodology outlined in Section 3.2.11 for approximately 35 minutes (including set up and take down) to mimic the stop-flow periods required for X-ray CT scanning and transport experiments. These alternating periods of flow were repeated until six simulated scan times were completed. Flow was then continued until approximately 1-2 pore volumes of Milli-Q water had passed through the column after the colour of the effluent samples changed from brown to clear.

3.2.11.2 Bismuth ferrite NP Transport and X-ray CT Scans

Bismuth ferrite NP transport and X-ray CT scan experiments were performed to monitor NP transport through a packed column. A bismuth ferrite NP flow-through and X-ray CT scan experiment

was completed within a glass column dry-packed with glass beads and saturated with Milli-Q water. This experiment was performed at a flow rate of 0.8 mL/min. The NP solution was injected for approximately 9.5 minutes. Scan 1 and Scan 2 were performed before injection and after the NP solution was visible about 2.5 cm from the bottom, respectively. Effluent samples were collected approximately every 10-12 minutes for 2 minutes until the NPs reached the top of the column, after which samples were collected continuously every 2 minutes. Once the colour of the effluent changed from brown to clear, sampling was again performed every 10 minutes.

3.2.11.3 NaI Transport and Scan Experiments

Experiments in which NaI was injected through a packed and saturated glass column were developed to assess the effects of flow rate and concentration on X-ray CT contrast agent transport. A NaI solution of 50, 75, or 100 g_I/L was injected at a flow rate of 0.35, 0.8, or 1.2 mL/min. A scan was completed before injection to serve as a baseline and ensure X-ray CT attenuation was equal throughout the column (i.e., the packing was homogeneous, and the density did not vary significantly throughout the column). Nine experiments were performed, the assigned naming scheme and associated experiment conditions are shown in Table 3-4. The NaI injection period and the sampling interval was dependent on the flow rate used (see Table 3-5)

Table 3-4: Naming scheme for NaI flow-through and X-ray scan experiments with associated flow rate and NaI solution injection concentrations.

Experiment Name	Injected NaI Concentration (g_I/L)	Flow Rate (mL/min)
IFT-1	100	0.35
IFT-2	100	0.8
IFT-3	100	1.2
IFT-4	75	0.35
IFT-5	75	0.8
IFT-6	75	1.2
IFT-7	50	0.35
IFT-8	50	0.8
IFT-9	50	1.2

Table 3-5: Summary of parameters for NaI flow though and scan experiments. The NaI slug injection times, the duration of flow with Milli-Q before the second X-ray CT scan, the total duration of flow between subsequent X-ray CT scans, and the effluent sampling interval are listed.

Flow Rate (mL/min)	NaI Injection Time (min)	Milli-Q flow period before the second X-ray CT scan (min)	Flow Interval between X-ray CT Scans (min)	Sample Collection Length (min)
0.35	10.75	20	15-25	5
0.8	5.5	5	15-25	5
1.2	3.5	4-5	8-14	2

3.2.12 Troubleshooting X-ray CT Scanning and Image Processing

Two troubleshooting experiments were performed to assess a conical shaped X-ray CT artifact observed in multiple processed images. First, a test was performed to evaluate if this effect was the result of shifting in the bead pack due to the effects of flow. An X-ray CT scan was performed after the packed acrylic column was subject to water transport at a low flow rate (0.1 mL/min) for approximately

2 hours, and again after the column had been subject to water transport at a high flow rate for around 2 hours (36 mL/min). A second experiment was designed to determine if this effect was the result of the scanning or image processing. The acrylic column was dry-packed with glass beads and saturated with water, was scanned by X-ray CT while “up-right” (I.e., with the inlet on the bottom and outlet on the top) and again after flipping the column (i.e., with the inlet on the top and the outlet on the bottom).

3.2.13 Flow-through Cuvette Contrast Scans

Flow-through column experiments were downscaled further, to the size of a 4.5 mL cuvette, to determine the minimum concentration of NaI at which an X-ray contrast could be observed in a saturated glass bead column. A small hole (~3 mm) was drilled into the bottom and the lid of a 4.5 mL cuvette sufficient to accommodate small tubing (approximately 3 mm outer diameter and 1 mm inner diameter). The tubing was inserted in the bottom and the lid of the cuvette and was sealed in place using EVA glue sticks and a hot glue gun. These cuvettes were dry-packed using repeated 0.2 mm lifts followed by manual compaction with a plastic plunger cut to fit the dimensions of the cuvette (1 cm x 1 cm square) until the cuvette was fully packed. Approximately 0.5 cm thick layers of glass wool were placed at the inlet (bottom) and outlet (top) of the cuvette to act as a baffle to distribute flow. Once the cuvette was fully packed, the lid was secured onto the cuvette and sealed using EVA glue sticks and a hot glue gun. Each cuvette designed in this fashion was used for a single test. In each experiment, a small slug was injected into the cuvette at a flow rate of 0.35 mL/min for approximately 2.5 minutes. The ends of each cuvette were then sealed by cutting the tubing and inserting a small amount of EVA hot glue into each of the tubing ends prior to X-ray CT scanning.

3.2.14 NaI Pycnometer Density Measurements

The density of the NaI solutions was measured using a 10 mL pycnometer based on ASTM D369 (ASTM International, 1985). The pycnometer was calibrated by filling it with DI water and leaving it in a water bath at room temperature for 30 minutes. The temperature of this bath was recorded to be constant at 22°C. The pycnometer was then dried, weighed, and the actual volume calculated based on the known density of water at 22°C (~0.99776 g/cm^3 (Engineering ToolBox, 2003)), calibration data can be found in Appendix B-8). NaI solutions were prepared and placed in the pycnometer, left to sit in the room temperature water bath for 30 minutes, and then dried and weighed. The density of these solutions was calculated based on the known volume of the pycnometer.

3.2.15 Analytical Methods

The total iron and total bismuth concentration in samples collected from Fe_3O_4 and bismuth ferrite flow-through experiments were quantified through inductively coupled plasma (ICP) analysis using an OES detector. 1 mL of the Fe_3O_4 or the bismuth ferrite NPs, were digested in 0.2 mL of concentrated (12.1 M) hydrochloric acid or nitric acid, respectively, with under constant mixing on a shaker table for 12 hours. Then 8.8 mL of dilute (0.121 M) hydrochloric acid was added to each sample such that samples were diluted by 10x. The sample order was randomized to reduce systematic error. Total iron concentrations were then converted into nanoparticle concentrations based on the oxygen fraction of the nanoparticle structure (Fe_3O_4), as given by

$$[Fe_3O_4\ NPs] = \frac{[Fe]}{1 - 0.27} \qquad 3\text{-}1$$

The Fe_3O_4 NP structure was previously characterized using energy dispersive X-ray spectroscopy in work by Linley et al. (2019). The exact composition of the bismuth ferrite NPs is not known with certainty, and thus the NP concentration could not be determined from total Bi measurements. As such, analysis of the bismuth ferrite NPs was performed using total bismuth concentration.

NaI concentrations were analyzed using Ion Chromatography (IC; Dionex DX-500). Effluent NaI samples were diluted by a factor of 100 before IC analysis. Ten batches of NaI samples (between 25-50 samples each) were analyzed with a new calibration curve being generated for each batch. The average calibration curve is shown in Appendix B-1.

3.3 Results and Discussion

3.3.1 Column Characterization

An estimation of the porosity was required to determine the pore volume (PV) of each column system, which was used in determining the total duration of experiments (all tracer experiments ran until approximately 3 PVs had passed through the column). Modeling results of the Br tracer BTCs indicate the average effective porosity for the glass column packed with glass beads is approximately 27.6 ± 8.2 %. The fitted porosity, dispersivity, and root mean square error (RMSE) for each bromide tracer experiment are displayed in Table 3-6, the BTCs showing observations and the fitted curves as generated by the model are found in Appendix B-2. The difference in the fitted effective porosity was large between Br-1 and Br-2 experiments, resulting in the large standard deviation on the estimate. Separately examining the effective porosities of Br-1 and Br-2 are 21.7 ± 2 %.and 36.4 ± 1.6 %, respectively. Columns were packed identically in all experiments, and as such, it is believed that the flow rate as measured from the inlet tubing was not representative of the flow-through the column systems

resulting in the large discrepancy between these two average porosities. While the flow rate does not affect the porosity of the system, it does influence the modeling results (as the porosity is estimated based on a calculation of average linear velocity and the flow rate input). During Br-1, for example, the flow rate was measured as 0.36 mL/min coming from the inlet tubing before connection to the columns, however, the flow rate measured from the effluent of columns A and B during Br was 0.325 and 0.37 mL/min respectively. The flow rate was only measured from the influent tubing for Br-2. Recovery percentages for all tracer experiments were calculated based on a trapezoidal approximation on the area under the curve and the assumption of a constant flow rate. As such, fluctuations in the flow rate may have influenced the accuracy of these calculations, see (Section 3.3.3).

Table 3-6: Summary of fitted porosity and dispersivity by 1-DUSAT modeling coupled with OSTRICH optimization for all bromide tracer experiments.

Experiment	Porosity	Dispersivity (m)	RMSE
Br-1-A	0.21	8.91E-04	28.8
Br-1-B	0.24	1.12E-03	29.4
Br-1-C	0.20	7.69E-03	56.5
Br-2-A	0.38	5.37E-04	8.3
Br-2-B	0.35	6.60E-04	12.5
Average	0.28	2.18E-03	
Standard Deviation	0.08	3.09E-03	

3.3.2 Glass Column X-ray CT Scans to Establish Fe_3O_4 Nanoparticle Contrast

To evaluate the ability of X-ray CT to monitor the transport of engineered NPs in a saturated representative geologic porous medium at a typical column scale, the capacity of the NPs to generate a discernable contrast relative to the background saturated porous material needed to be verified. Two preliminary scans were performed to confirm that the Fe_3O_4 NPs would be distinguishable from the saturated glass beads.

The result of Fe_3O_4 NP Contrast Scan 1 is shown in Figure 3-3. In this figure, and all subsequent X-ray CT scan results, the blue and green colors represent areas of higher and lower X-ray attenuation, respectively. The location of the blue section in Figure 3-3 (left) generally aligns with the location of the NPs (brown section), as seen in the photo of the column in Figure 3-3 (right). It must be noted that the 3-D spatial image produced from an X-ray CT scan provides attenuation information through the entire sample, and thus, can give an indication of the NP tracer location within the core of the packed column. Conversely, visual inspection only provides evidence on the NP slug location near the column wall. Indeed, the uniformity of the processed scan image is inconsistent with the visual NP distribution evidenced by the column photo. To assess the cause of this discrepancy, the column was carefully unpacked in thin layers (approximately 1 cm thick) to obtain visual confirmation of the NP distribution throughout the column (see Appendix B-4 for images). It was revealed that NP fingering had occurred, likely due to gravity (see Section 3.3.10), resulting in an uneven spatial distribution of the NPs. Overall, these results indicated that glass beads saturated with Fe_3O_4 NP suspension at 500 mg/L were distinguishable from glass beads saturated with Milli-Q water using X-ray CT.

The result of Fe_3O_4 NP Contrast Scan 2 (Figure 3-4) shows eight layers comprising of (from bottom to top) glass beads saturated with Milli-Q water, 100, 200, 300, 400, and 500 mg/L NP solutions, and finally, two layers saturated with Milli-Q water. The increasing concentration of blue pixels from Layer 3 to 7 coincide with increasing NP concentrations, providing evidence that X-ray attenuation is influenced by the concentration of nanoparticles in a sample. However, the attenuation observed in Layer 8 (which is absent of NP) appeared equivalent to that seen in Layer 7 (which contained 500 mg/L NP). Furthermore, Layer 2 (Milli-Q only) exhibits similar attenuation to Layer 4 (300 mg/L NP), and the attenuation between the three layers saturated with only Milli-Q water (Layers 2, 8 and 9) vary

substantially, with higher X-ray attenuation evident at the top of the column. Two key factors influence X-ray attenuation, the density of the material the X-rays are passing through, and the atomic numbers of the elements that comprise the material (Denison et al., 1997; Taina et al., 2008; Wellington and Vinegar, 1987). The identical composition of layers 2, 8, and 9 should result in equivalent or similar X-ray attenuation between these sections in the processed image. The X-ray attenuation is higher than expected for these layers and cannot be explained by NP diffusion from adjacent layers or differences in density due to packing, suggesting that the observed differences in X-ray attenuation are not solely due to the presence of NP the column.

The results of the processed images presented in Figure 3-3 and Figure 3-4 both display an observable contrast in the column where the NPs are present. However, they also show X-ray attenuation to be stronger at the top of the column relative to the bottom regardless of the location of the NPs. This contrast shape is discussed in more detail in Section 3.3.6.

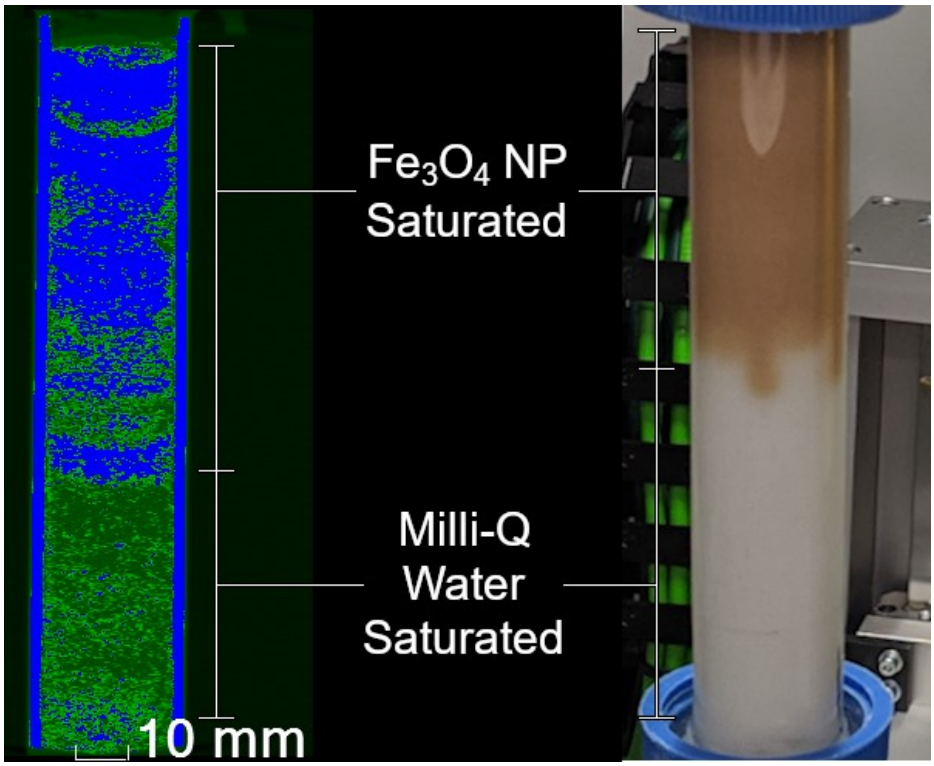

Figure 3-3: X-ray CT contrast scan of glass column wet packed with glass beads using only Milli-Q water in the bottom half and Fe_3O_4 NP solution in the upper half (left), and a photo of the same column (right).

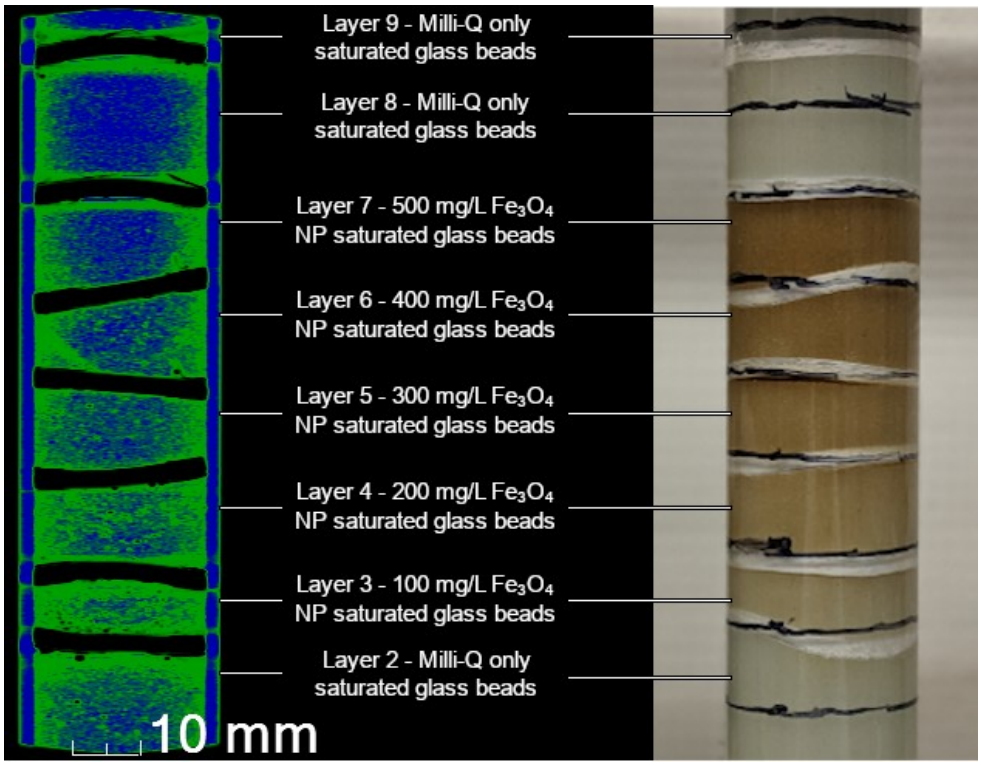

Figure 3-4: Segmented Column NP Contrast Scan 2 showing the processed X-ray CT scan (left) and a photo of the column before the scan (right). The processed image shows (from bottom to top) a Milli-Q saturated bead section, 100, 200, 300, 400, 500 mg/L NP sections, and then two sections of Milli-Q beads.

3.3.3 Fe_3O_4 NP Transport and X-ray CT Scans

After establishing the relationship between NP concentration and X-ray attenuation (Figure 3-3 and Figure 3-4) a NP transport and scan experiment was performed. During this experiment, six X-ray CT scans were completed. Table 3-7 lists the duration of the flow and stop-flow periods between scans. The NP slug (brown) is seen migrating from the bottom (Figure 3-5 A) to top (Figure 3-5 C) in the images of the column, which were taken just before Scans 2, 4, and 6, respectively. The position of the nanoparticle slug in the column did not correlate with areas of high X-ray attenuation from the

corresponding X-ray CT scan image. This result suggests that the attenuation occurring as a result of the NP presence is not significant enough to be distinguished from the attenuation resulting from the saturated glass beads and column. Possible reasons explaining the absence of X-ray contrast at the location of the NP slug include (1) high background X-ray attenuation by the column or porous media, or (2) insufficient X-ray attenuation from the NP slug. Potential options to improve X-ray CT contrast include (1) decreasing the scale and density of the porous medium and column which will reduce the background X-ray attenuation, (2) increasing the concentration of the Fe_3O_4 NP solution X-ray attenuation by the NPs, or (3) developing a NP solution that has a higher X-ray attenuation. The only changed condition between this Fe_3O_4 NP tracer and scan experiment, Fe_3O_4 NP Contrast Scan 1 (see Figure 3-3) and Fe_3O_4 NP Contrast Scan 2 (see Figure 3-4) is the method in which the NPs were introduced into the column (i.e., wet packed into place rather than injected). Thus, the inability to distinguish the NP slug in the processed X-ray CT images during this experiment implies that the contrast observed in the two previous Contrast Scan experiments may have been due to a "conical effect" artifact (more details in Section 3.3.6).

Figure 3-6 shows the NP BTC developed from effluent samples measured by ICP analysis. The standard deviation on ICP NP concentration measurements (after conversion of total iron to NP concentration) was determined to be $\pm$ 0.11 mg/L based on results from calibration checks made every 10 samples using a stock 10 mg/L total iron solution. Assuming a constant flow rate of 0.36 mL/min, the estimated mass recovery was 86.4 ± 0.02% (error calculated based on propagation of error from a trapezoidal approximation of the curve). The estimated mass recoveries calculated from the BTCs of four Br^- tracer experiments performed in the saturated glass bead packed glass columns were found to range from 84-85 %, assuming a constant flow rate throughout the experiment, which was measured from the

inlet tubing before connection to the column. The cause for deviation from an expected 100% mass recovery is an indication that the measured flow rate was not representative of the column system since NaBr is a known conservative tracer. The flow was measured at the beginning of each experiment directly from the connective tubing before being attached to the column. Thus the actual flow rate during column operation may have been affected by back-pressure. The same issue is believed to have occurred for the Fe_3O_4 NP transport experiment. Thus, the similar mass recoveries between the Fe_3O_4 NPs and the Br tracer experiments suggest that the NPs employed in this work exhibit efficient transport through in an inert glass bead porous medium for a distance of at least 15.24 cm. This result is in agreement with previous Fe_3O_4 transport experiments performed in a 15 cm long column in clean Borden sand (Linley et al., 2019b).

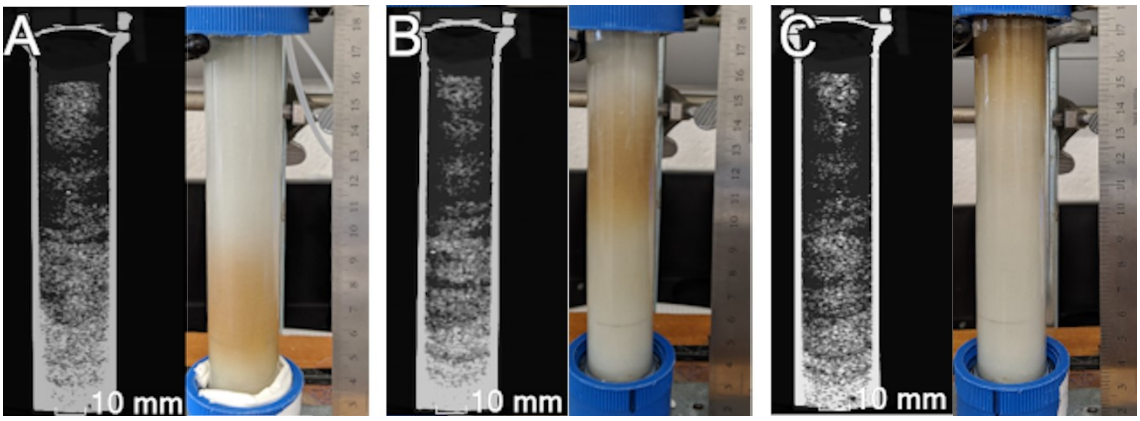

Figure 3-5: Fe_3O_4 NP transport X-ray CT results showings (A) Scan 2, (B) Scan 4, and (C) Scan 6. A phot of the column taken immediately before each scan is placed to the right of each processed scan image. In these processed images, the white regions represent areas of higher X-ray attenuation, while the black regions represent areas of lower X-ray attenuation.

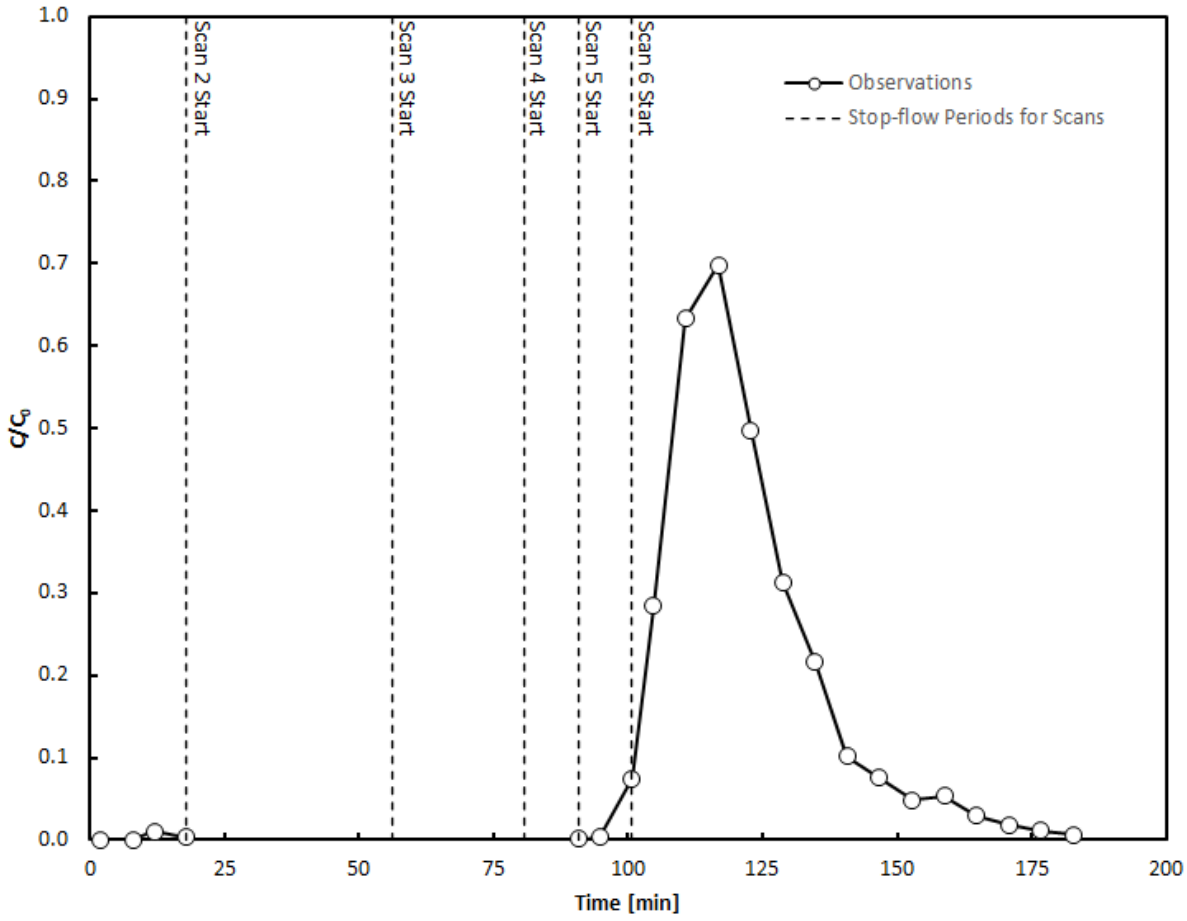

Figure 3-6: Fe_3O_4 NP breakthrough curve. Injection began after 12 minutes of flow with Milli-Q water and was stopped after approximately 21.5 minutes of flow. The time of the stop-flow periods required for each X-ray CT scan have been removed for clarity. The stop-flow periods relative to effluent sample points is shown by the vertical black dashed lines. Scan 1 was performed before sample collection. The stop-flow periods for Scans 2, 3, 4, 5 and 6, were approximately 61, 50, 34.5, 40, and 45 minutes, respectively.

Table 3-7: Flow and stop-flow time before X-ray CT scans for the Fe_3O_4 NP transport and scan experiment.

Scan ID	Flow Duration Before Scan (min)	Stop-flow Time by end of Scan (min).
Scan 1	26.5 (21.5 min NP injection + 5 min Milli-Q water)	55.2
Scan 2	10	61
Scan 3	12	50
Scan 4	12	34.5
Scan 5	10	40
Scan 6	10	45

3.3.4 Fe_3O_4 NP Cuvette Contrast Scans

Although there are several differences between the experiments performed in this research and those performed by Linley et al. (2019), the largest are the scale and saturated condition. Linley et al. (2019) successfully established Fe_3O_4 NP X-ray CT contrast from clean sand in 4.5 mL cuvettes under dry conditions. Thus, a series of contrast experiments were designed at the same scale to investigate if a Fe_3O_4 NP solution could be distinguished from water using X-ray CT. Four contrast scans were performed on two stacked cuvettes filled with (A) 6500 mg/L Fe_3O_4 NP solution (top cuvette) and Milli-Q water (bottom cuvette), (B) 650 mg/L Fe_3O_4 NP solution (top cuvette) and Milli-Q water (bottom cuvette), (C) glass beads wet packed with 6500 mg/L Fe_3O_4 NP solution (top cuvette) and glass beads wet packed with Milli-Q water (bottom cuvette), and (D) glass beads wet packed with 650 mg/L Fe_3O_4 NP solution (top cuvette) and glass beads wet packed with Milli-Q water (bottom cuvette). The processed images of these scans are shown in Figure 3-7. In Figure 3-7 A the high concentration of blue pixels in the top cuvette indicates that the Fe_3O_4 NPs have a higher X-ray attenuation that water and can be distinguished. In Figure 3-7 B, C, and D, the same observation holds as the grey-value threshold was selected such that the lower X-ray attenuating voxels in the bottom cuvette were completely removed

from the image leaving only the higher attenuation voxels in the top cuvette. This observation indicates that the variation in X-ray attenuation between the Fe_3O_4 NP solution and Milli-Q water is sufficient for X-ray CT contrast to exists, which further indicates that the attenuation resulting from the glass beads and the glass column high enough to mask this difference. These findings support the prior conclusion that decreasing the scale and density of the porous medium and column or an increase in the concentration of the Fe_3O_4 NP solution was required for the difference in X-ray attenuation to be sufficient enough to observe X-ray CT contrast. However, it is also recognized in Figure 3-7 B, C, and D that the remaining voxels show a conical X-ray attenuation pattern. Thus, this contrast may be the result of a "conical effect" artifact (see Section 3.3.6 for more details) rather than due to an uneven distribution of the Fe_3O_4 NPs.

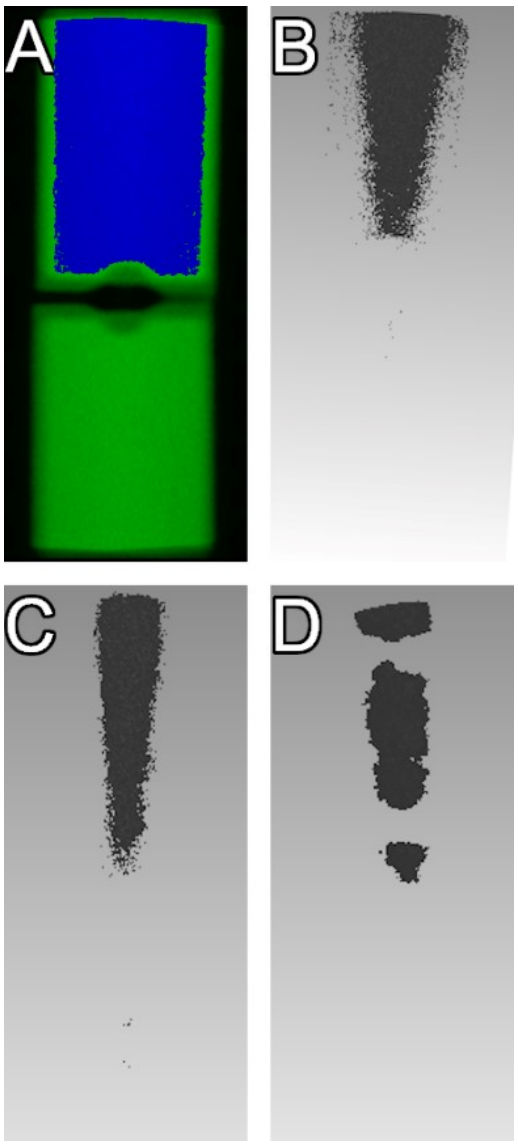

Figure 3-7: Liquid to liquid X-ray CT processed images between water (bottom cuvette) and Fe_3O_4 NP solution (top cuvette). Showing (A) 6500 mg/L Fe_3O_4 NP solution compared to water, (B) 650 mg/L Fe_3O_4 NP solution compared to water, (C) glass beads wet packed with 6500 mg/L Fe_3O_4 NP solution compared to glass beads wet packed with water, and (D) glass beads wet packed with 650 mg/L NP solution compared to glass beads wet packed with water. In (A), The blue and green sections represent areas of higher and lower X-ray attenuation, respectively. In (B), (C) and (D), the grey-value threshold has been set such that the lower X-ray attenuating voxels have been removed from the image and thus the remaining dark grey voxels shown here represent the higher X-ray attenuating regions of the sample.

3.3.5 Acrylic Column X-ray CT Scans to Establish Fe_3O_4 Nanoparticle Contrast

Results from the cuvette contrast scans suggested that the X-ray attenuation resulting from the glass beads and glass column may have effectively masked the difference in X-ray attenuation between the Fe_3O_4 NPs and the Milli-Q water-saturated pore spaces. Thus, Fe_3O_4 NP contrast scans were performed in a less dense (relative to glass) and smaller acrylic column, which should result in a lower X-ray attenuation by the apparatus and packing material (Denison et al., 1997; Taina et al., 2008; Wellington and Vinegar, 1987). Furthermore, the X-ray CT results in the glass column suggested that Fe_3O_4 NP contrast may be observed when the NPs are wet packed into place rather than injected. Thus, the column was dry-packed, saturated with water, and the NPs were introduced by injection to ensure that the observed contrast was due to the presence of the NPs in the column and not due to variations in density distributions introduced during the wet packing process. A scan of the packed and saturated acrylic column before an injection Fe_3O_4 NP at 6500 mg/L shows a higher X-ray attenuation in the center of the column, followed by the top and then the bottom (Figure 3-8 A). After injection, these zones of contrast seem to shift slightly, with the bottom of the column showing higher X-ray attenuation than the center. However, the top of the column, where no NPs were present, also displayed a higher attenuation than the center (Figure 3-8 B), which is an indication that this change, in contrast, is not solely due to the presence on the Fe_3O_4 NPs. This result suggests that the attenuation resulting from the glass beads and the acrylic column sufficiently high to mask the difference in attenuation between the Fe_3O_4 NP solution and Milli-Q. Thus, the Fe_3O_4 NP solution is not suitable as an X-ray CT contrast agent in saturated glass beads at the scale of this acrylic column (0.9 cm diameter, approximately 10 cm length) at a concentration of 6500 mg/L.

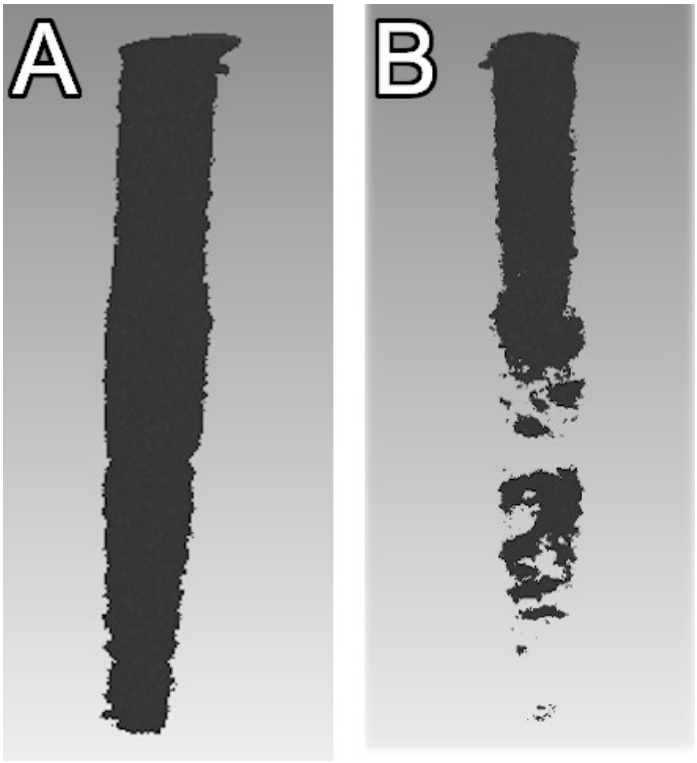

Figure 3-8: Processed X-ray CT images of the acrylic column packed with glass beads. Showing (A) the packed column saturated with water before NP injection and (B) after NP injection. Lower X-ray attenuating voxels "vanish" from the figure first during processing, the remaining dark grey voxels shown here represent the higher X-ray attenuating regions of the sample.

3.3.6 Acrylic Column Scans for X-ray CT Troubleshooting

A consistent observation in many of the X-ray CT column images was a "conical effect", in which a higher X-ray attenuation was observed near the top of the column that extends downward in the shape of an upside-down cone (for example see Figure 3-4, Figure 3-7 B, C, and D). No change, in contrast, was observed in an acrylic column that was wet packed with glass beads and scanned after periods of water injection of low and high flow (0.1 and 36 mL/min). This result suggests that a change in fluid pressure due to fluid flow did not impact the density profile within the column (Figure 3-9 A and B). A second NP contrast scan was performed in the acrylic column to verify the results observed in Figure

3-8. A 6500 mg/L NP solution was injected into the column until it was visible approximately 5cm from the inlet before performing a third X-ray CT scan. The processed image of this scan revealed no change in the observed X-ray attenuation following this injection (Figure 3-9 C). This further indicates that the attenuation resulting from the glass beads and the acrylic column is too high for the difference in attenuation between the Fe_3O_4 NP solution and Milli-Q water to be distinguished.

To assess if the conical shape of X-ray CT attenuation was an artifact arising from the scanning or image processing the acrylic column was scanned both "upside right" (i.e., the inlet of the column on the bottom and outlet on the top) and after being inverted (i.e., the inlet of the column on the top and outlet on the bottom). This column was packed with plastic pellets (cylindrical in shape, approximately 0.5cm in length, 0.2 cm in diameter, density < 1 g/cm^3), to minimize the attenuation resulting from the porous media (Denison et al., 1997; Taina et al., 2008; Wellington and Vinegar, 1987). Figure 3-10 shows the resulting processed images. The conical contrast shape is observed before and after inversion, which confirms that this effect is an artifact of the X-ray CT scanning or processing. If the observed X-ray attenuation was the result of material variations (such as packing density), then the conical contrast should have been inverted with the column. A conceptual schematic of the proposed explanation for the cause of this artifact is shown in Figure 3-11. Theoretically, X-ray attenuation will be highest passing through the core (i.e., along the longitudinal central axis) of the column as the X-rays pass through more material (Figure 3-11 A). The bottom of the column is clamped into a rotating sample holder; thus, any alignment issue is more exaggerated near the top. As a result, the thickest part of the column (i.e., the center) is farther away from the central axis relative to the sample holder, skewing the area of highest X-ray attenuation to the left and right of this axis as the sample rotates (Figure 3-11 B). Such misalignment

may result in a broader range of high attenuation voxels near the top of the column, moving downward once the scan is reconstructed into the 3-D image (Figure 3-11 C).

The results of these troubleshooting experiments suggest that the presence of the NPs may not have caused the change in contrast observed in the initial acrylic column scan to establish Fe3O4 NP contrast (Figure 3-8). The absence of contrast observed in the acrylic column flow rate experiment following the injection the Fe_3O_4 NP (Figure 3-9) confirmed that the attenuation caused by the NPs was not sufficient to be distinguished from the attenuation of the acrylic column saturated and packed with glass beads. Furthermore, the confirmation of the "conical effect" being an artifact of the X-ray CT scanning or image processing provides evidence that the findings from Fe_3O_4 NP Contrast Scan 1 and 2 in the glass column, and from the two Fe_3O_4 NP contrast scans performed in the acrylic column, were due to an off-axis column alignment. The stacked cuvettes in the Styrofoam holder also had a sample height of approximately 10 cm (similar to the acrylic column), thus, the observations made in the 3.3.4 Fe3O4 NP Cuvette Contrast Scans (see Figure 3-7 B, C and D) may have also been impacted by sample misalignment.

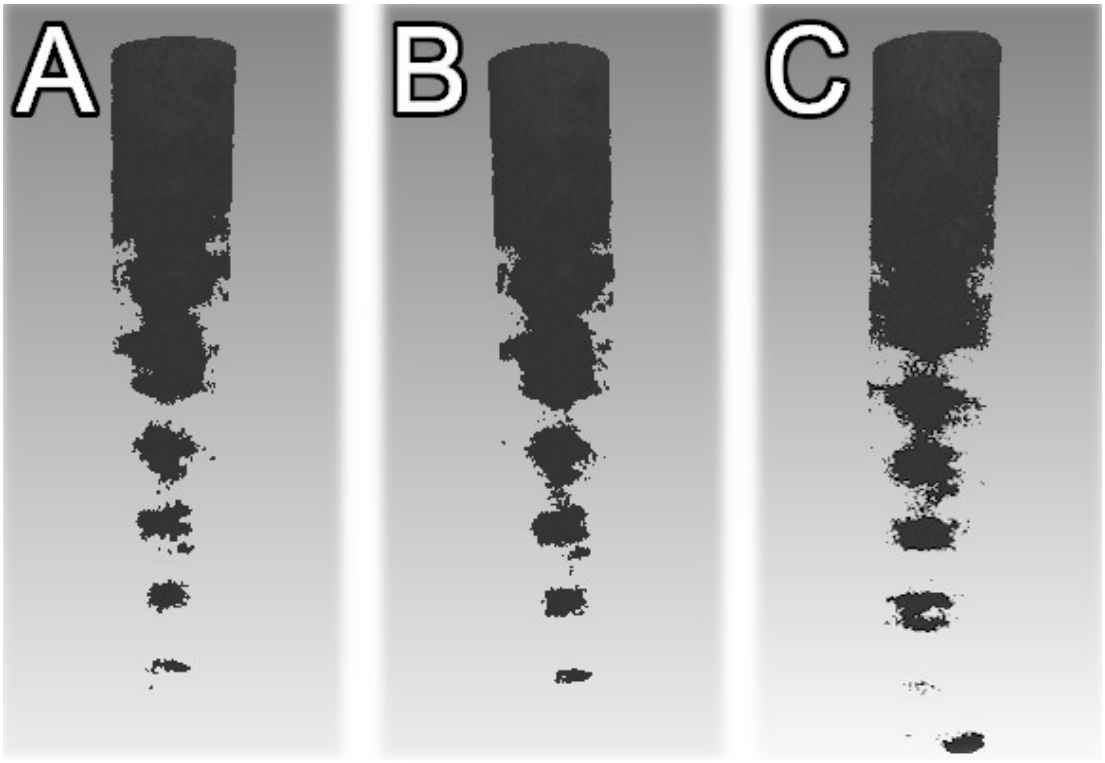

Figure 3-9: X-ray CT scan of the acrylic column showing (A) glass beads saturated with Milli-Q water after low flow (0.1 mL/min), (B) the column after high flow (36 mL/min), and (C) the column after injection of 6500 mg/L NPs. Only voxels above the selected threshold grey value are visible in the processed scan images, thus, the remaining dark grey voxels shown here represent the higher X-ray attenuating regions of the sample.

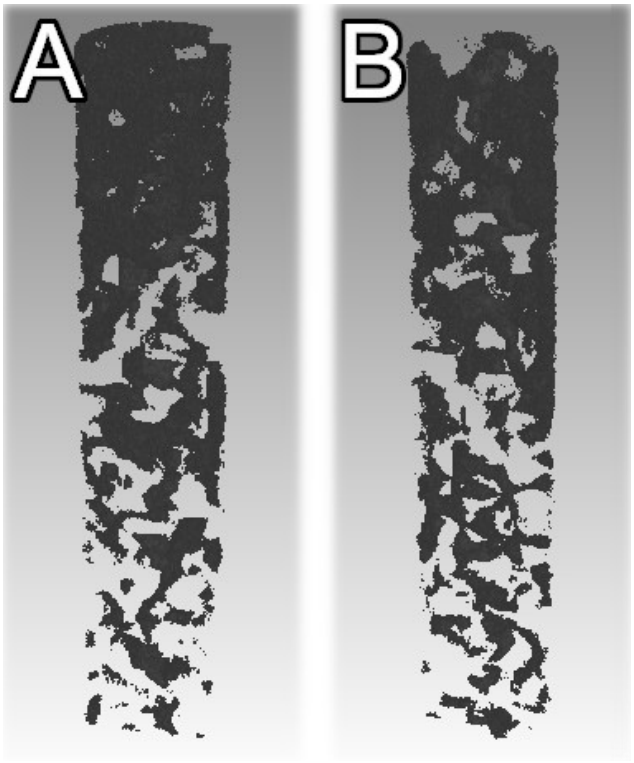

Figure 3-10: X-ray CT scans of (A) the acrylic column packed with plastic pellets and saturated with water, and (B) the same column after being inverted. Only voxels above the selected threshold grey value are visible in the processed scan images, thus the remaining dark grey voxels shown here represent the higher X-ray attenuating regions of the sample.

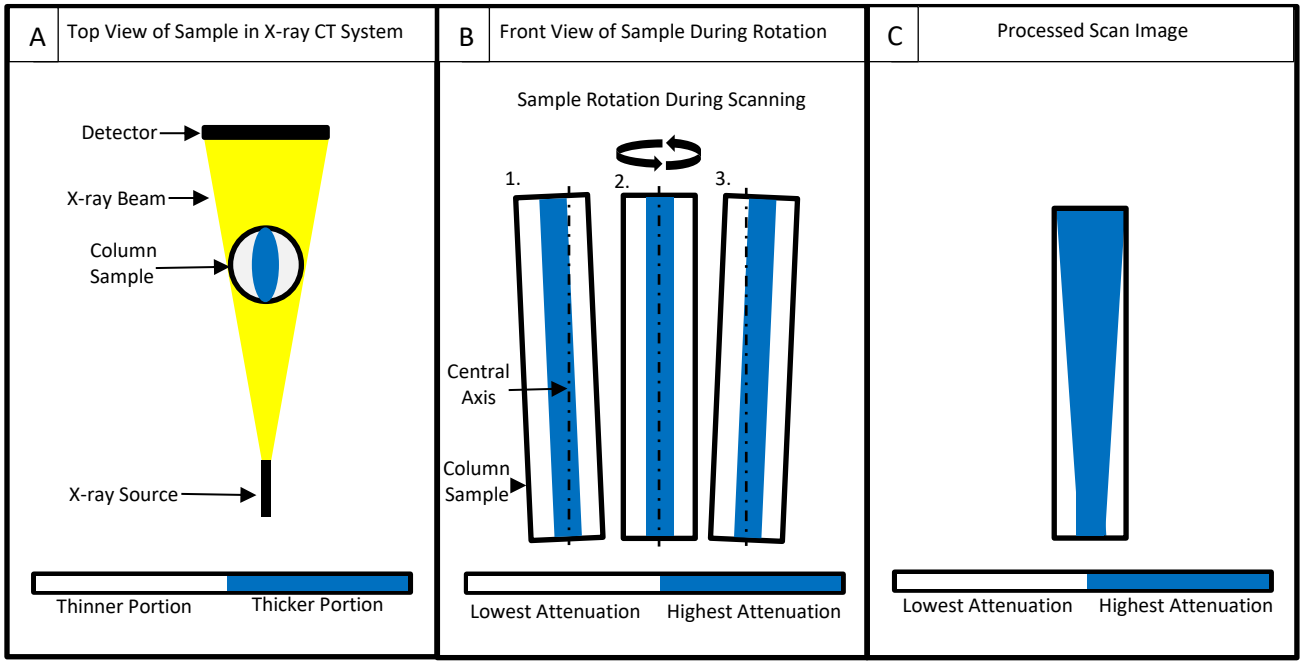

Figure 3-11: Conceptual schematic of the presumed cause for the "conical effect" scanning artifact for a cylindrical homogenous sample, such as the glass column that is saturated and packed with glass beads. (A) represents a top view of the X-ray CT system and highlights the thickest portion of a column relative to the X-ray source and detector. (B) depicts a column that is slightly off-center of its central axis relative to the sample holder as it rotates in the X-ray CT system, the theoretical zone of highest X-ray attenuation as a result of sample thickness is highlighted. (C) shows a potential 2-D slice from the resulting 3-D reconstructed image of the X-ray CT scan.

3.3.7 Flow-through Cuvette Contrast Scans with Fe_3O_4 NPs and NaI

A cuvette was modified to allow flow-through and was subject to an injection with a 6500 mg/L Fe_3O_4 NP solution before X-ray CT scanning to determine if the attenuation contrast observed in the Fe3O4 NP Cuvette Contrast Scan between two stacked cuvettes, the top cuvette containing glass beads wet packed with 6500 mg/L Fe_3O_4 NP solution and the bottom cuvette containing glass beads wet packed with Milli-Q water (Figure 3-7 D), was the result of a "conical effect" artifact or due to the presence of the Fe_3O_4 NP solution. This cuvette was dry-packed with glass beads and saturated with Milli-Q water before NP injection. In the processed image (Figure 3-12), no change in X-ray attenuation

is observed following the injection of the NP solution. This result suggests that the X-ray attenuation occurring due to the glass beads under saturated conditions is large enough to mask any differences in attenuation arising due to the presence of the NPs at the cuvette scale (i.e., 1 cm cx 1 cm x 4.5 cm and an X-ray CT voxel size of approximately 95-97 μm). Furthermore, a conical contrast is apparent in Figure 3-12, indicating that the "conical effect" artifact can arise in longitudinally dominating samples where the sample height: width ≥ 4.5:1 (i.e., the scale of the 4.5 mL cuvettes).

To confirm that an injected fluid could be distinguished from the glass beads and water, a high concentration NaI solution (100 g_I/L) was injected approximately 2.25 cm into a flow-through cuvette that was dry-packed and saturated with water. The resulting processed image is shown in Figure 3-13, with the green and dark grey represents areas saturated NaI and water, respectively. A clear contrast is discernible with the high concentration of NaI used resulted in a "shine-through artifact" (e.g., (Abdul-Fatah et al., 2009)). This confirms that if the difference in X-ray attenuation is sufficient between an injected contrast agent and the background saturating fluid, porous media, and column, a contrast will be discernable.

Additional flow-through cuvettes were injected with decreasing concentrations of NaI solutions to a distance of approximately 2.25 cm from the inlet and scanned to determine the NaI concentration threshold where contrast was no longer observed in a processed image for the given sample conditions (see Appendix B-5). A concentration of 15 g_I/L was determined as the lower detection threshold for the packed and saturated flow-through cuvettes. Based on this lower NaI detection threshold, any solution with an X-ray attenuation equal or higher than that of a 15 g_I/L solution should be distinguishable by the X-ray CT system once injected into a cuvette packed with glass beads and saturated with water.

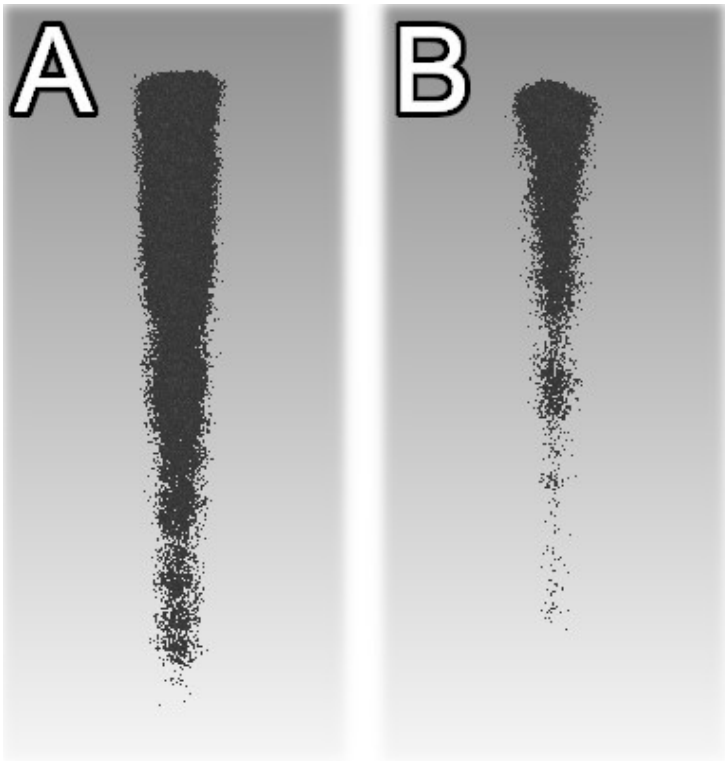

Figure 3-12: Processed X-ray CT scans of flow-through cuvette packed with glass beads and saturated before 6500 mg/L Fe_3O_4 NP injection (A) and after injection (B). Only voxels above the selected threshold grey value are visible in the processed scan images, thus the remaining dark grey voxels shown here represent the higher X-ray attenuating regions of the sample.

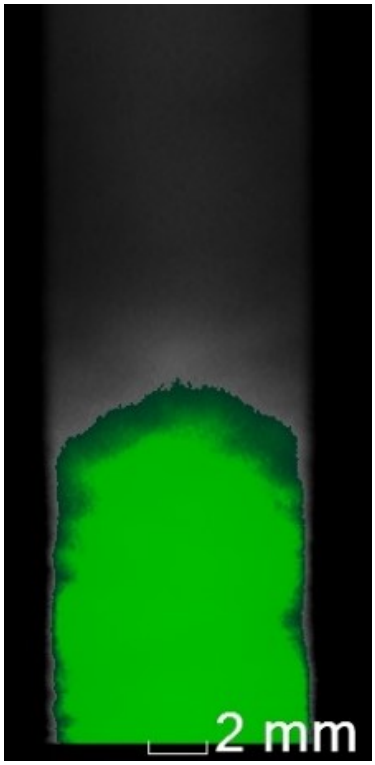

Figure 3-13: Processed X-ray CT image of a flow-through cuvette saturated with water and packed with glass beads after injection with 100 g_I/L NaI solution. The green areas represent the areas of highest X-ray attenuation followed by grey and then black areas, respectively.

3.3.8 Static Cuvette Contrast Scans Between Fe_3O_4 NPs and NaI

In the previously reported stacked cuvette contrast scans between water and Fe_3O_4 NP suspensions, the relative X-ray attenuation was successfully compared (Section 3.3.4). Thus, similar experiments were repeated to compare the Fe_3O_4 NP and NaI solutions. Known concentrations of Fe_3O_4 NP solution were compared to varying concentrations of NaI until the relative X-ray attenuation between the two stacked cuvettes was approximately equal (i.e., the grey-value threshold for the voxels should be roughly equivalent). The NP solution was placed in the bottom cuvette to avoid any false contrast observations that may have arisen from the “conical effect” artifact.

The results from these liquid to liquid contrast scans are summarized in Figure 3-14 (see Figure B 7 in Appendix B-6 for the processed X-ray CT images). The highest concentration of NP suspension tested was 120 g/L. At this concentration, the solution was very viscous and difficult to manipulate. Furthermore, any mixing or pipetting of the 120 g/L NP solution resulted in foaming, likely due to the increased amount of stabilizing surfactant used to achieve this high concentration. The highest concentration that was observed to be workable (i.e., had a workable viscosity to flow and potentially be injected into a cuvette or column) was 50 g/L. A linear relative X-ray attenuation relationship was found to exist between the Fe_3O_4 NPs and Nai with an equivalence ratio of ~5:1 NP:NaI (e.g., 1 g_I/L NaI is equivalent in X-ray attenuation to 5 g/L Fe_3O_4 NP) up to a 50 g/L NP solution, (Figure 3-14). Observations indicated that the X-ray attenuation of a ~70 g/L Fe_3O_4 NP solution would be approximately equivalent to a 15 g_I/L solution. The viscosity of the NPs at this concentration was deemed too high to be injected into a flow-through cuvette. Thus, no X-ray CT contrast scan was performed at this concentration. Therefore, Fe_3O_4 NP solution is not suitable for use as an X-ray CT contrast agent in a glass bead saturated porous medium at any of the three scales used in this work (i.e., the glass column, acrylic column, or cuvettes).

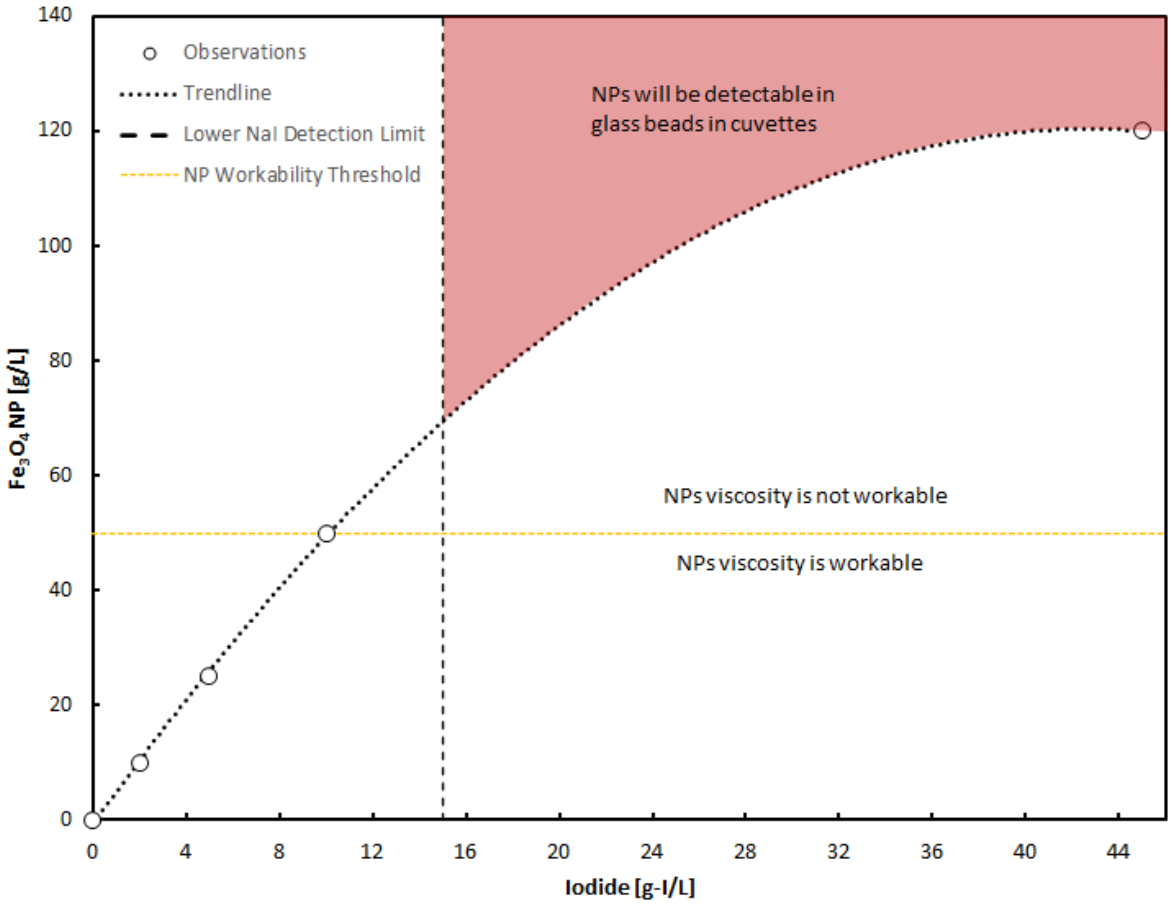

Figure 3-14: Comparison of equivalent X-ray CT attenuation between NaI and Fe_3O_4 NP solutions. The lower detection limit of NaI in saturated glass beads, as well as the observed NP workability threshold, are shown. The R^2 value of the trendline shown is 0.9998.

3.3.9 Glass Column NaI Contrast Scan

To utilize NaI as an X-ray CT imaging contrast agent for tracer experiments it was first necessary to determine an injection concentration NaI at which attenuation contrast would be observed. Thus, Two contrast scans were performed using 50 and 100 g_I/L NaI solutions, respectively (Figure 3-15). In both processed images, a clear contrast is observed at the bottom of the column where the NaI is present.

The lower detection threshold of NaI in the glass column saturated and packed with glass beads was established by injecting decreasing concentrations of NaI into a packed and saturated glass column and performing X-ray CT scans. In Figure 3-16 A and B, it is evident by the blue pixels at the bottom of the column that the NaI injected at concentrations of 25 and 15 g_I/L has a high enough attenuation to generate an observable contrast. This contrast is also apparent for injection concentrations of 5 and 10 g_I/L (Figure 3-16 C and D), however, the presence of the blue pixels at the top of these processed images indicates that the "conical effect" impacted results at these concentrations (Section 3.3.6). This suggests that either there were no issues with alignment in the 15 and 25 g_I/L scans, or that "conical effect" artifacts are negligible when differences in relative X-ray attenuation are large enough. Although contrast is observed at the base of the processed image for the 5 and 10 g_I/L injection scans, the lower detection threshold for NaI in the glass column saturated and packed with glass bead was determined to be 15 g_I/L due to the absence of this artifact (Figure 3-16 B) at this concentration.

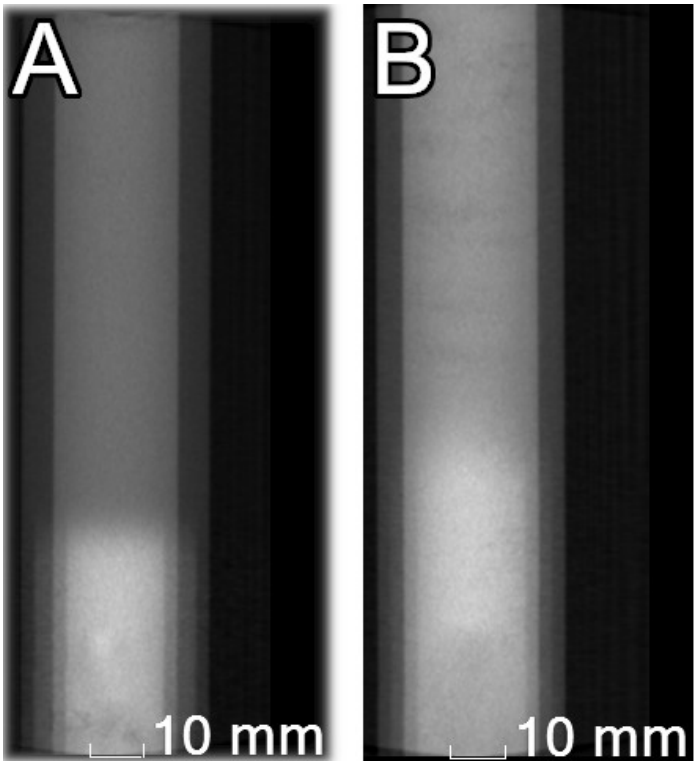

Figure 3-15: Initial glass column NaI X-ray CT contrast scans showing injection of (A) 50 g_I/L and (B) 100 g_I/L NaI solutions. The bright white and grey regions represent areas of higher and lower X-ray attenuation, respectively.

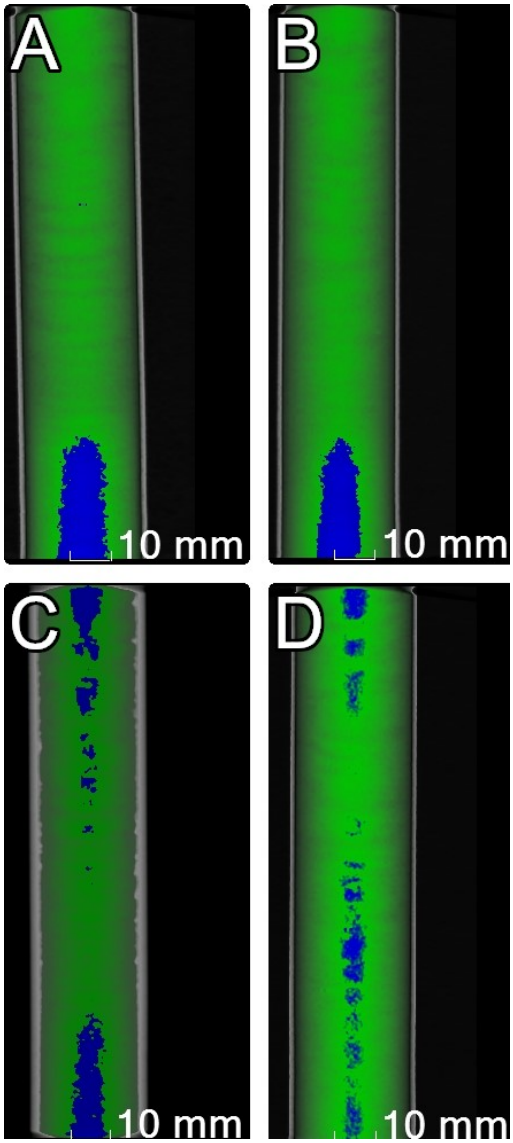

Figure 3-16: Glass column NaI minimum detection limit X-ray CT contrast scans for injections of (A) 25 g_I/L, (B) 15 g_I/L, (C) 10 g_I/L, and (D) 5 g_I/L solutions.

3.3.10 Glass Column NaI Transport Experiment and Scans

X-ray CT tracer experiments were performed using NaI to assess the effects of concentration and flow rate on the transport of an X-ray CT contrast agent. Nine NaI tracer and X-ray CT scan experiments were performed using concentrations of either 50, 75, or 100 g_I/L at flow rates of either 0.36, 0.8, or 1.2 mL/min. As an example, Figure 3-17 shows the X-ray CT scan results for experiment IFT-9 (50 g_I/L injection and flow rate of 1.2 mL/min), the processed scan images for IFT-1, and IFT-3 to 8 experiments are provided in Appendix B-7. The migration of the NaI slug is apparent after injection as the concentration of blue pixels moves from the bottom to the top of the column. This behavior was observed for the other IFT experiments, thus indicating that the migration of a NP solution with sufficient X-ray attenuation should be observable in X-ray CT "snap-shots" of the column.

A memory issue occurred with the X-ray CT computer during experiment IFT-2 that resulted in a 2.5 h delay between Scan 3 and Scan 4 (see Figure 3-18 B and C). The change in contrast between Scan 3 and Scan 4 suggests that the NaI slug sank towards the bottom of the column. Following this observation, water was injected into the column for approximately 26 minutes to migrate the slug to the top of the column (see Figure 3-18 D). The inlet and outlet valves were then closed, and the column was left for 2 hours before Scan 6 was performed, where the shape and location of the observed contrast shifted again (see Figure 3-18 E). After being left for approximately four days, no contrast was visible in the processed X-ray CT image of the column (see Figure 3-18 F). The absence of contrast in Figure 3-18 (F) indicates that (1) the NaI slug may have sunk back into the injection tubing, or (2) the NaI concentration had dispersed equally within the column such that the X-ray attenuation was similar throughout.

The results of experiment IFT-2 suggest that the density difference between the NaI solution and the injected water was significant enough for viscous fingering to occur. Closer examination of processed images from Scan 2, Scan 3, and Scan 4 for experiment IFT-9 (Figure 3-17 A, B, and C) also reveals a longitudinal expansion of the observed contrast as flow and stop-flow periods continued. The displacement of freshwater by an above denser NaCl solution has also been observed by Menand and Woods (2005). Menand and Woods (2005) introduced a term known as the "gravity number" (N_G) to describe the ratio of gravitational to background fluid velocity as a means of describing the gravitational instability between two miscible fluids. The gravity number was later modified by Flowers and Hunt (2007) and is given by:

$$N_G = \frac{kg(\rho_{bot} - \rho_{top})}{n\mu_D|U|} \qquad 3\text{-}2$$

where k is the permeability, g is the acceleration due to gravity, ρ_{bot} is the density of the lower fluid, ρ_{top} is the density of the upper fluid, n is the porosity, μ_D is the dynamic viscosity of the displacing fluid, and U is the pore water velocity. Flowers and Hunt (2007) also discuss the idea of the "mobility ratio" (M), a parameter that describes the ratio of the resident fluid viscosity to the displacing fluid viscosity given by:

$$M = \frac{\mu_R}{\mu_D} \qquad 3\text{-}3$$

where μ_R is the resident fluid viscosity and μ_D is the displacing fluid viscosity. Using the mobility ratio and the gravity number Flowers and Hunt (2007) show that the criterion for stable miscible displacement (i.e., the conditions that must be met for one fluid to displace another without the formation of viscous fingers), based off the original criterion for stable miscible displacement demonstrated by Hill and P (1952), is defined by:

$$N_G > M - 1 \qquad 3\text{-}4$$

Using this criterion, Flowers and Hunt (2007) show that stability or instability for a given displacement between two fluids can be quickly determined based on its position in one of four potential regions of stability (see Regions I, II, III, and IV in Figure 3-19). Regions II and IV represent inherently stable and unstable conditions, respectively, as both viscosity and density serve to either stabilize or destabilize the system. In regions I and III, the stability between the two fluids is dependent on the viscosity and density differences. In Region 1, the system is unstable due to viscous forces but can be stabilized by gravity (i.e., a less dense fluid above a more dense fluid). In contrast, in Region III, the system is gravitational unstable but can be stabilized by viscous forces (i.e., the viscosity of the displacing fluid is higher than the viscosity of the resident fluid). The NaI transport and scan experiments can be broken down into two experimental conditions; (1) the displacement of water by the NaI solution as NaI is initially injected into the column, and (2) the displacement of NaI by water as the NaI slug moves through the column. It is recognized that condition (1) also exits concurrently with condition (2) until the NaI slug reached the top of the column.

Figure 3-19 plots the calculated values for N_G and M for all IFT experiments during flow conditions (1) and (2). The viscosities of the water and the NaI solutions were not measured and were taken to be the viscosities of the respective fluids at 25°C and 100 kPa (Abdulagatov et al., 2006; Engineering ToolBox, 2004). As expected, the experimental conditions are stable for all NaI transport experiments during the injection of NaI. However, the conditions become unstable for all concentrations of NaI used once the water was injected into the column to facilitate the NaI slug to migrate, and thus viscous fingering is expected to occur. This analysis is in agreement with the movement and lateral elongation for the of the contrast regions observed in Figure 3-17 and Figure 3-18. Viscous fingering is

expected to have occurred even if the NaI was injected at a concentration of 15 g_I/L (i.e., the lower detection threshold determined for the glass column saturated and packed with glass beads).

The BTC for experiment IFT-9 ignoring the stop-flow times required for X-ray CT scanning is shown in Figure 3-20 (see Appendix B-9 for BTCs for the other NaI transport and scan experiments). Note that a complete BTC was not created for IFT-2 since effluent samples were not collected following the four days of no-flow used to assess the sinking and spreading of the NaI slug. The BTCs coupled with the processed scan images for all IFT experiments indicate that the flow-rate and concentration have little effect on the ability of X-ray CT to monitor the migration of a contrast agent through a saturated glass bead porous medium, outside of the viscous fingering observed. Thus, these results indicate that a NP solution can be used as an X-ray CT contrast agent at flow rates between 0.36 – 1.2 mL/min (corresponding to average linear velocities of 0.25 and 0.85 cm/min, respectively, in the glass column system when packed with glass beads). The concentration of a NP solution X-ray CT contrast agent must only be considered in terms of the value needed to obtain an X-ray attenuation contrast, and as it relates to density to predict viscous fingering effects.

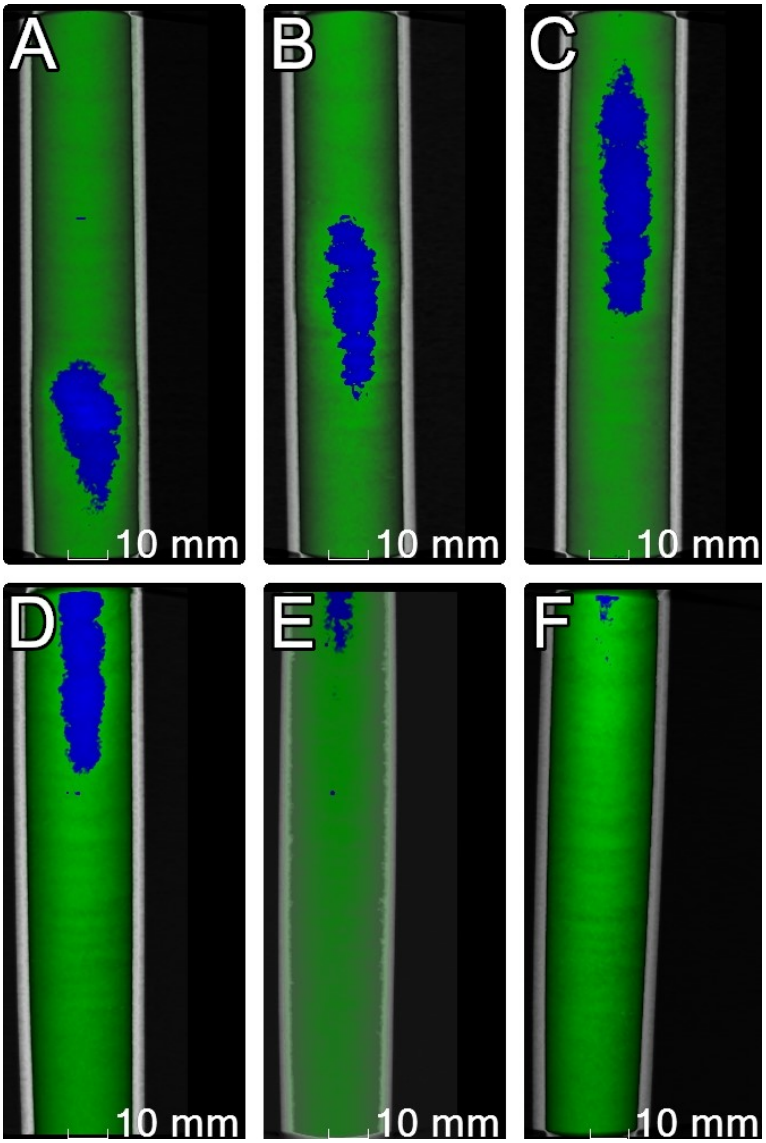

Figure 3-17: IFT-9 X-ray CT processed images showing (A) Scan 2, (B) Scan 3, (C) Scan 4, (D) Scan 5, (E) Scan 6, and (F) Scan 7. Scan 1 was performed before NaI injection. The flow time before Scans 2 – 7 were 3.5 minutes of NaI injection plus 11 minutes of flow with Milli-Q water, then 4.5, 4.5, 6, 6, and 6 minutes of flow with Milli-Q Water, respectively. The stop-flow periods required for Scans 2-7 were 55.5, 60.5, 60.5, 62, 80, and 77 minutes, respectively.

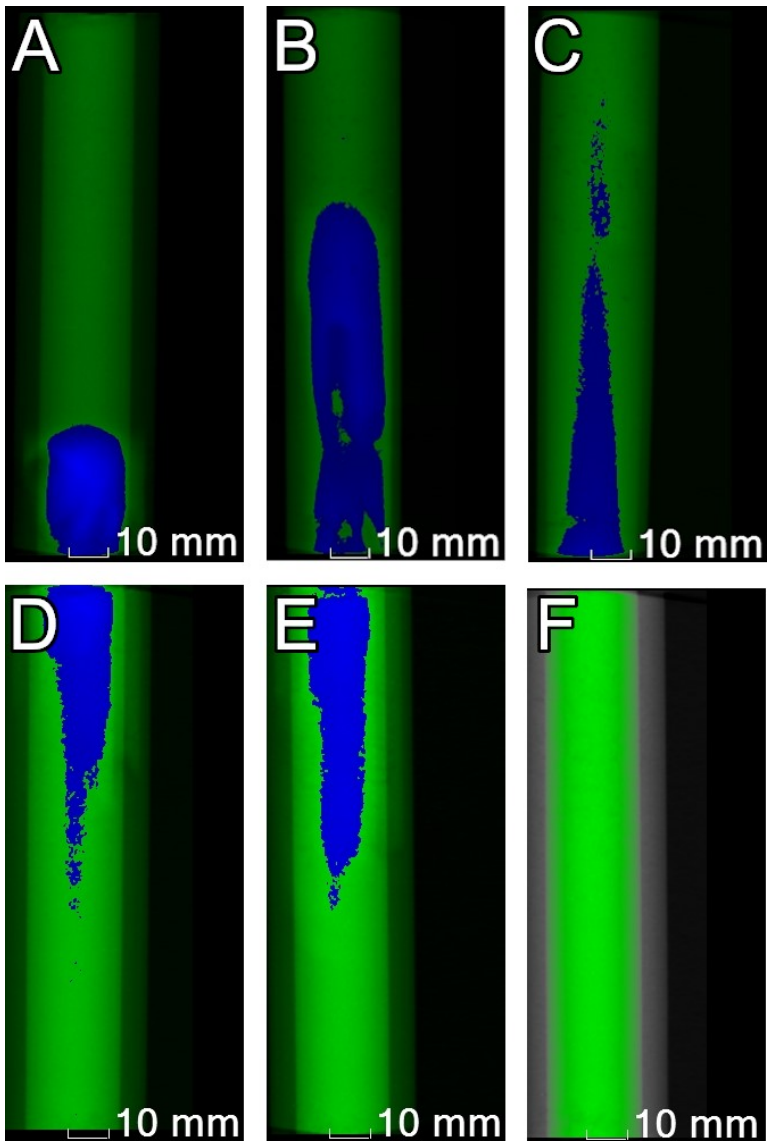

Figure 3-18: IFT-2 X-ray CT processed images showing (A) Scan 2, (B) Scan 3, (C) Scan 4, (D) Scan 5, (E) Scan 6 and (F) Scan 7. Scan 1 was performed before NaI injection. The flow time before Scans 2 – 5 were 5.5 minutes of NaI injection plus 5 minutes of flow with Milli-Q water, then 10, 8, and 26 minutes of flow with Milli-Q Water, respectively. The stop-flow periods for Scans 2-6 were 64.5, 90, 150, 40, 144 minutes, respectively. The total stop flow period before scan 7 was four days. No flow occurred after scan 6.

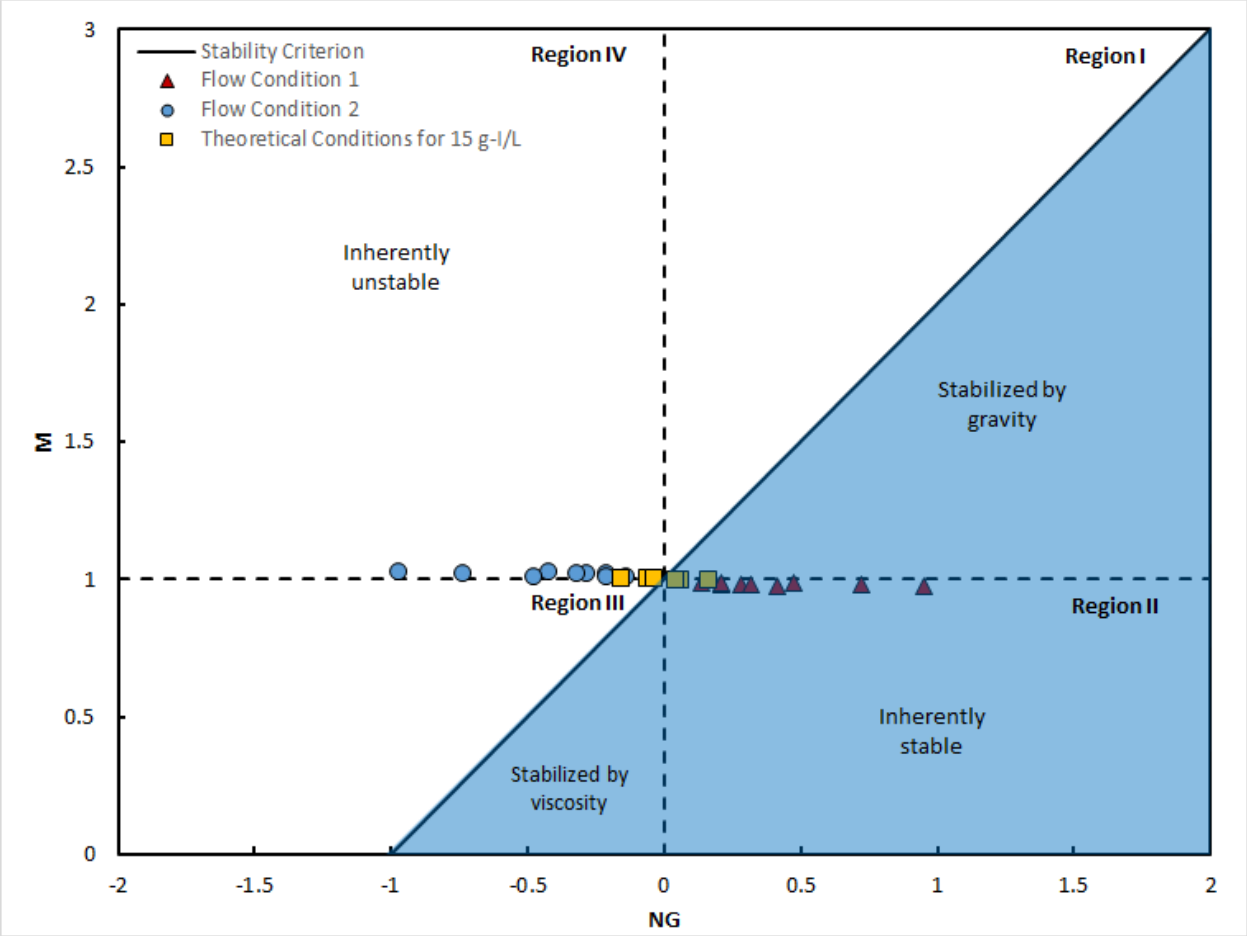

Figure 3-19: Theoretical stability analysis for the displacement of two miscible fluids. The blue triangular region represents stable flow conditions. The conditions for all IFT experiments are shown by blue and red points. The red points represent the initial NaI injection where NaI is displacing water in the column (flow condition 1), and the blue points represent the subsequent displacement of the NaI solution by water (flow condition 2). Viscous fingering is expected as soon as water begins to displace NaI in the column. The orange points represent the theoretical stability of the system for a 15 g_I/L solution.

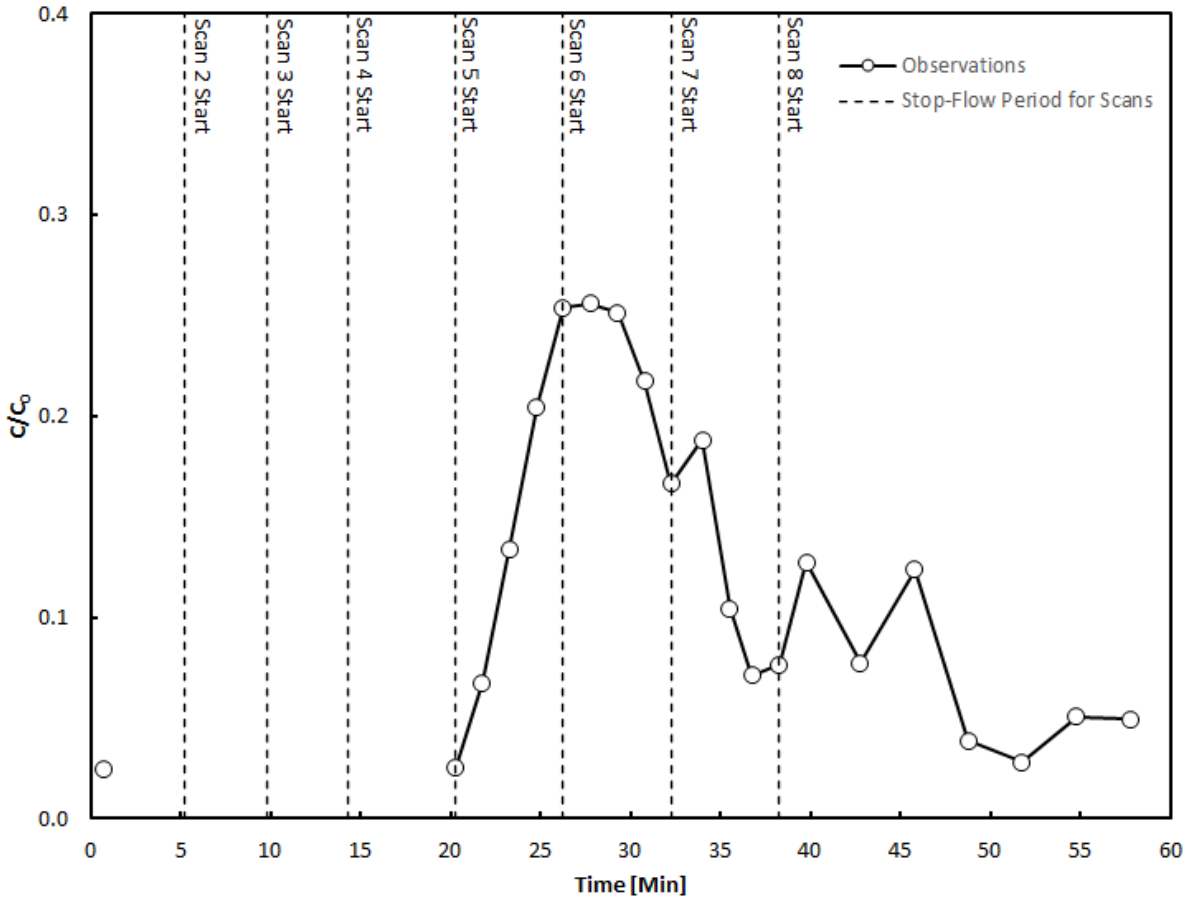

Figure 3-20: BTC for IFT-9. The time of the stop-flow periods required for each X-ray CT scan has been removed for clarity. The location of each stop-flow period for each scan relative to the effluent sample points is shown by the vertical black dashed lines. Scan 1 was performed before sample collection. The stop-flow times for Scans 2 through 8 were approximately 55.5, 60.5, 66.5, 62, 80, 58 minutes, respectively.

3.3.11 Bismuth ferrite NP Contrast and Flow-through Scans

For the bismuth ferrite NPs to generate sufficient contrast to be distinguished from the glass beads and glass column they must have an X-ray attenuation approximately equivalent to that of a 15 g_I/L solution. Thus, a stacked cuvette contrast scan was performed between 15 g_I/L and approximately

7.8 g_{Bi}/L bismuth ferrite NP solutions. As visible by the concentrations of blue pixels in Figure 3-21, the bismuth ferrite NP suspension in the top cuvette had a greater X-ray attenuation than the 15 g_I/L solution. Thus, suggesting that the bismuth ferrite NPs will provide sufficient contrast to be distinguished by X-ray CT in a glass bead-packed column.

The bismuth ferrite NP solution was injected at a concentration of approximately 7.8 g_{Bi}/L into a glass bead packed and saturated glass column to confirm their use as an X-ray CT imaging contrast agent for monitoring tracer transport. A concentration of blue pixels can be seen migrating from the bottom to the top of the column in the processed X-ray CT scans of the bismuth ferrite transport experiment (Figure 3-22). The synthesis of a NP solution comprising of a higher atomic number element (atomic number of bismuth, 83, is approximately three times larger than that of iron, 26) resulted in a much higher X-ray attenuation resulting in an observable contrast at a much lower NP concentration. Based on the results shown in Figure 3-14, the concentration of bismuth ferrite required to attain an observable X-ray attenuation contrast is nearly nine times less than the concentration of a Fe_3O_4 NP solution needed to attain this contrast in an identical column system. However, it appears that a concentration of ~7.8 g-Bi/L was not sufficient enough to overcome the "conical effect" artifact, which is visible before the NP injection (Figure 3-22 A) and in all other scans (Figure 3-22 B-F). As a result, it is difficult to discriminate between the NP slug and this artifact at the top of the column (Figure 3-22 D, E, and F). After Scan 6, effluent samples were collected, and Milli-Q water was injected for 76 minutes until the effluent ran clear. Then the column was scanned, inverted (such that the inlet was on the top and the outlet was on the bottom), and scanned again (see Figure 3-23). A vertical X-ray attenuation gradient is present from top-to-bottom in both scans, confirming the presence of the "conical effect" artifact. Thus, the bismuth ferrite NPs used in this work at a concentration of approximately 7.8 g_{Bi}/L are suitable as X-

ray CT contrast agents in a saturated glass bead porous medium at the column scale used (15 cm length, 2.54 cm inner diameter), however, a higher NP concentration would likely improve results and may be required to ensure “conical effect” artifacts are eliminated from results.

The BTC produced for this experiment is shown in Figure 3-23. The standard deviation on a triplicate of samples from the injection solution was approximately $\pm$ 0.7 mg/L. Based on a trapezoidal estimation of the area below the BTC, assuming a constant flow rate of 0.8 ml/min, the mass recovery was found to be ~76.97 ± 0.01%. This mass recovery estimate is relatively in agreement with the results obtained in the Fe_3O_4 NP tracer experiment and with results obtained by Linley et al. (2019b), indicating that the bismuth ferrite NPs synthesized are suitable for transport in a saturated glass bead porous medium for distances of at least 15 cm. However, this mass recovery estimate may also have suffered from the same issue experienced with Br tracer experiments discussed in Section 3.3.3.

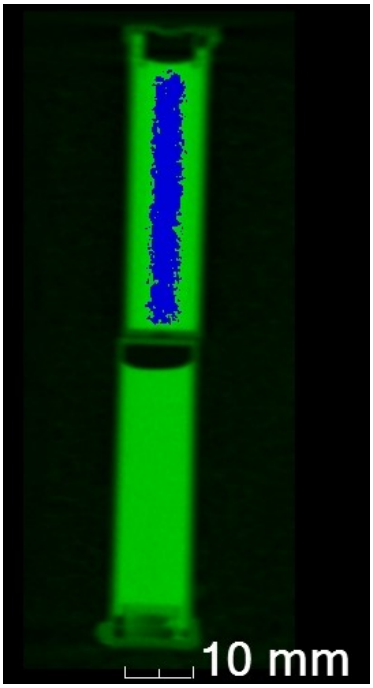

Figure 3-21: X-ray CT contrast scan of two 4.5mL cuvettes filled with ~7.8 g_{Bi}/L bismuth ferrite NP (top) and 15 g/L NaI (bottom).

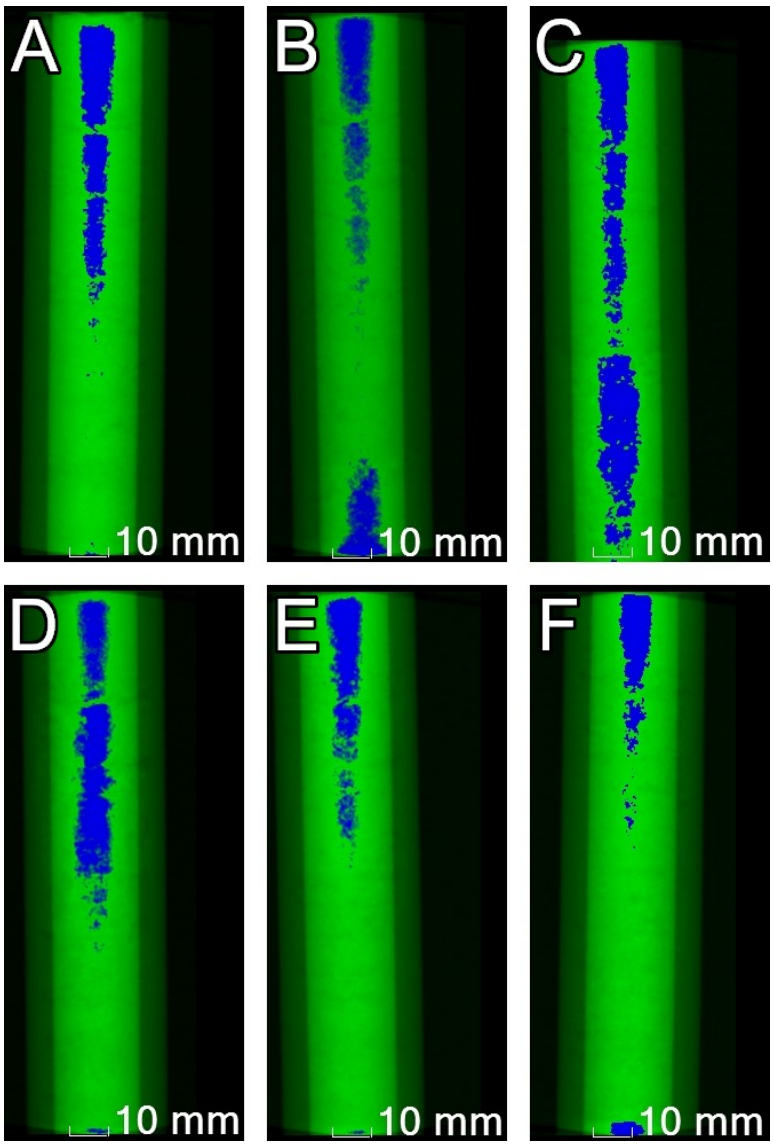

Figure 3-22: Bismuth ferrite NP transport X-ray CT results showing processed images for (A) Scan 1, (B) Scan 2, (C) Scan 3, (D) Scan 4, (E) Scan 5 and (F) Scan 6. The flow time before Scans 2 – 6 were 9.5 minutes of bismuth ferrite NP injection, then flow with Milli-Q water for 6, 10, 14, and 14 minutes, respectively. The stop-flow periods required for Scans 2-6 were 41.5, 38, 63, 41, and 44 minutes, respectively.

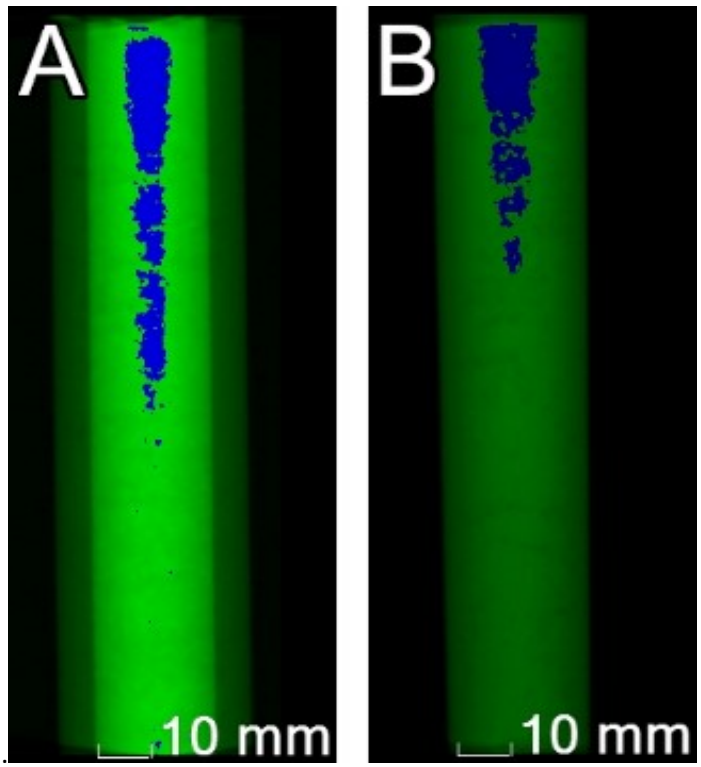

Figure 3-23: X-ray CT processed images of the glass column immediately after water flushing to remove all bismuth ferrite NPs, showing the upright column (A) and the same column flipped (B).

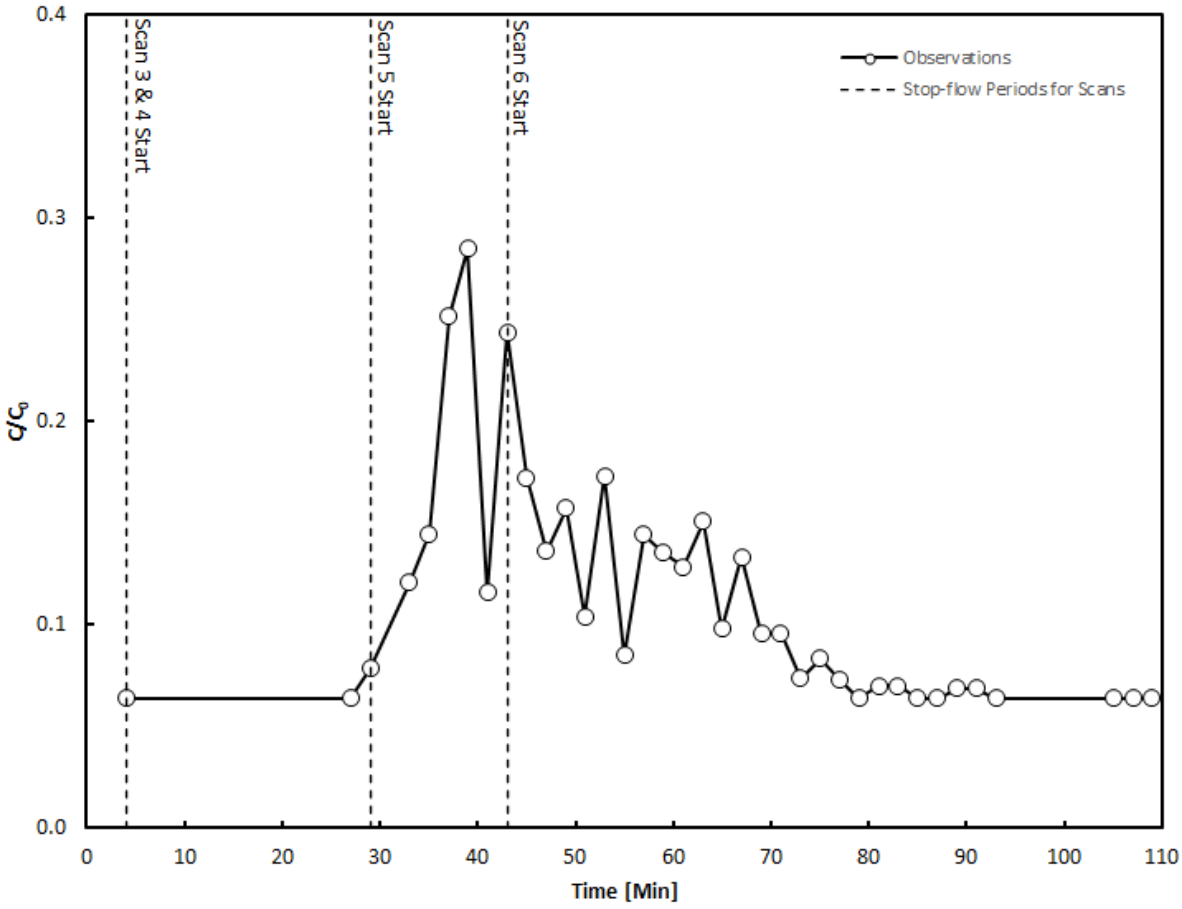

Figure 3-24: BTC for bismuth ferrite transport experiment. The time of the stop-flow periods required for each X-ray CT scan has been removed for clarity. The location of each stop-flow period for each scan relative to the effluent sample points is shown by the vertical black dashed lines. Effluent sample collection began after Scan 2. The duration of the stop-flow periods for Scans 3 and 4, 5, and 6, were 164, 41, and 44 minutes, respectively.

Chapter 4

Major Findings and Future Work

4.1 Conclusions

The primary focus of this research was to assess the use of NPs as X-ray CT imaging to monitor the transport of NP contrast agents through a saturated geologic porous medium at the column scale. Three column systems were used to achieve this goal: glass column (15.24 cm length, 2.54 cm inner diameter), an acrylic column (10.16 cm length, 0.9 cm inner diameter), and 4.5 mL acrylic cuvette (4.5 cm length, 1 cm by 1 cm cross section). The following sub-objectives were defined to achieve the overall objective:

1. Establish NP solution contrast in an aqueous environment.
2. Establish NP solution contrast in a saturated porous medium.
3. Isolate and examine X-ray CT artifacts that may impact the use of NPs as imaging contrast agents in column tracer experiments.
4. Determine the effects of concentration and flow rate on X-ray CT contrast agent transport and monitoring.
5. Develop an appropriate methodology to assess the suitability of NP solutions as X-ray CT imaging contrast agents in a saturated porous medium through comparison to a known X-ray CT contrast agent.

Experiments were first designed to determine the suitability of Fe_3O_4 NPs as X-ray CT contrast agents, but it was found that a NP concentration of approximately 70 g/L was required for the difference in X-ray attenuation between these NPs and the saturated glass bead porous medium to be observed at any of the column scales used. The high viscosity of the Fe_3O_4 NP solution above a concentration of

approximately 50 g/L would hinder their use as a tracer through a saturated porous column, thus, it is was concluded that the Fe_3O_4 NP solution used in this research is not suitable as an X-ray CT contrast agent in a saturated glass bead porous medium at any of the scales assessed (i.e., the glass column, acrylic column or cuvette scale).

Only one X-ray CT artifact was observed to influence X-ray CT scanning results. This is a reoccurring contrast pattern in which X-ray attenuation was seemingly greatest at the top to the columns extending downward in a conical shape, which has been termed a “conical effect” artifact in this work. Through troubleshooting experiments performed in the acrylic column, this effect is suggested to occur due to column misalignment in the X-ray CT system during scanning. Results further indicate that the influence of artifact is negligible, where the difference in X-ray attenuation is sufficiently large between two or more materials.

Nine NaI tracer and X-ray CT scanning experiments were performed to assess the impact of concentration and flow rate on X-ray CT scans of a contrast agent tracer migrating through a saturated porous column. The flow rate was found to have little impact on the ability to monitor the transport of a contrast agent using X-ray CT; however, concentration was found to affect both the magnitude of X-ray attenuation and the density (and therefore transport) of the solution. Experimental results indicated that the concentration of a contrast agent must be high enough to produce an X-ray attenuation that is sufficiently larger than the attenuation caused by the saturated porous medium and column to generate an observable contrast in X-ray CT images. Furthermore, viscous fingering due to gravitational instability was observed in the column systems due to the higher density if NaI relative to that of Milli-Q water at the concentrations used.

Through comparative scans performed for NP suspensions and NaI solutions stacked in 4.5 mL cuvettes, and through experiments to determine the minimum concentration of NaI required for an observable attenuation contrast in a given column system, the following procedure was demonstrated to be a successful method of assessing the suitability of NP solutions as X-ray CT imaging contrast agents in a saturated porous medium:

1. Determine the minimum concentration of NaI (or a similar known contrast agent) required to obtain X-ray CT contrast within a sample at given X-ray CT scanning parameters.
2. Compare the X-Ray attenuation of the selected contrast agent at its minimum concentration to the candidate NP suspension
3. Examine the processed X-ray CT image and determine if the relative X-ray attenuation of the NPs is less or greater than the NaI solution.
    a. If the NPs have a higher relative X-ray attenuation, then they will be suitable for use as imaging contrast agents in the given system using the X-ray CT scan parameters selected.
    b. If the NPs have a lower relative X-ray attenuation, then the NPs will not be suitable as imaging contrast agents. The system must either be modified, the concentration of the NP solution be increased, or a different engineered NP must be used.

A bismuth ferrite NP solution was synthesized as a NP suspension comprising of a higher atomic number element was required to increase the X-ray attenuation of the NP contrast agent solution. X-ray CT scans performed at the cuvette scale proved this bismuth ferrite NP solution to be an effective X-ray

CT contrast agent in a saturated glass bead porous medium. The NP mass recovery was approximately 77 % in a tracer experiment performed with the bismuth ferrite NPs, indicating that these NPs are capable of transport in a saturated glass bead porous medium for distances of at least 15 cm. Finally, the use of X-ray CT to monitor the transport of the bismuth ferrite NP solution was successfully demonstrated in a tracer experiment performed through a saturated glass bead porous medium at the glass column scale. Thus, it is concluded that the bismuth ferrite NPs are a suitable X-ray CT contrast agent in saturated glass bead porous mediums.

4.2 Research Contribution

This research expanded on the work presented by Linley et al. (2019) by demonstrating the potential to use engineered NPs as X-ray CT imaging contrast agents in saturated porous media. This study opens exciting opportunities for future X-ray CT soil studies as NPs offer the potential benefit of target-specific binding in comparison to traditional X-ray CT contrast agents such as NaI. Finally, as X-ray CT is an electromagnetic imaging technique, the work presented here serves as a proof-of-concept for the use of NPs as imaging contrast agents for electromagnetic geophysical methods. The inability of the Fe_3O_4 NPs to generate X-ray CT contrast followed by the synthesis and successful contrast obtained with the bismuth ferrite NPs highlights the ability to modify the properties of engineered NPs to generate a response from an electromagnetic imaging method. NPs could be designed, for example, to enhance the response of GPR by altering the dielectric permittivity, EMT by changing the conductivity, MS by modifying the magnetic response, or NMR by affecting the relaxation times, of the porous media they occupy.

4.3 Recommendations for Future Work

Much of the research presented here involved the troubleshooting of a methodology to assess the suitability of engineered NPs as X-ray CT imaging contrast agents in a representative saturated geologic porous medium. The following general recommendations are made for future research efforts that expand on the work presented here:

1. Column alignment in the X-ray CT system may result in "conical effect" artifacts. Thus, it is recommended that a specialized holder is constructed to ensure that the column is aligned with the central axis of the sample rotator. This holder must be designed such that it does not interfere with X-ray CT scanning results.
2. High contrast agent concentration may be required to achieve an observable X-ray attenuation contrast within a saturated porous column. Thus, the density of the contrast agent should be considered to prevent the occurrence of viscous fingering in column transport studies. Any movement of the contrast agent slug during X-ray CT scanning, such as by viscous fingering, could result in temporal artifacts (an elongated zone of contrast, for instance) and thus should be eliminated for X-ray CT studies. Zhang et al. (2019) recently overcame this issue of gravitational instability in an X-ray CT study by substituting water for a denser NaCl solution as the saturating fluid. It is recommended that the density difference between the resident and the displacing fluids be minimized in future X-ray CT column studies.
3. It is recommended that new NP suspensions being considered for use as an X-ray CT contrast agent in saturated porous systems be compared directly to a known X-ray CT contrast agent following the methodology outlined in Section 4.1.

4. Higher resolutions should be used where possible as this would improve the detection potential for NP contrast in saturated porous media. For instance, if the spatial resolution was at a nanoscale then clusters of NPs may be more easily distinguished.

Several studies are recommended as avenues to expand upon the research presented here:

1. The "conical effect" artifact that was observed in many of the X-ray CT scans in this research is still not fully understood and should be studied further. This issue highlights the sensitivity of X-ray CT systems to small sample alterations. To further investigate this effect, a specialized support could be constructed in which a packed column can be held within an X-ray CT system that allows for small incremental changes to the column alignment relative to the central rotating axis of the X-ray CT sample holder. In this way, the extent of the "conical effect" artifact based on the magnitude of sample misalignment could be fully explored. Furthermore, the column could be injected with increasing concentrations of a known contrast agent, such as NaI, and scanned at various misalignment angles to determine if this artifact is negligible where the difference in X-ray attenuation between two or more materials is sufficiently high.
2. The motivation for this research was to assess the use of NPs to enhance the quality of the information that can be obtained from X-ray CT and geophysical imaging. The bismuth ferrite NPs used here employs the same polymeric coating as the Fe_3O_4 NPs investigated by Linley et al. (2019), and as such, they are also expected to show preferential binding to crude oil. Future work for this research should include assessing the ability of the bismuth ferrite NP to bind to crude oil and evaluating the degree of image contrast enhancement they provide for X-ray CT scans of a porous medium impacted with crude oil. First, batch experiments should be performed to confirm targeted binding. Then, transport and binding column experiments in

which a small section of the packed column is impacted with crude oil and X-ray CT scanning is performed before, during, and after an injection of bismuth ferrite NPs should be completed to determine if the contrast of the impacted section is enhanced by the NPs. Such a study could result in a better understanding of NP binding to the crude oil by highlighting binding location and density. These visual observations could provide valuable insights related to contaminant remediation such as the total NP-NAPL binding area and expected binding concentrations. This work should first be performed using an inert saturated glass bead medium but should then be replicated using natural aquifer materials.

3. The relative attenuation of the bismuth ferrite NP contrast agents, as determined by the X-ray CT to NP concentration, should be investigated. This could be achieved by developing identical porous media packed columns, each containing a "control" area (such as separated water-saturated section), injecting them with various concentration of bismuth ferrite NP solutions, and relating the relative attenuation of the bismuth to that of the control for each sample. Through modeling, it may be possible to quantify the concentration distribution of the NPs in each column.
4. In addition to improving contaminant delineation, the use of NPs as imaging contrast agents may be useful in assessing contaminant remediation. For instance, a given contaminant could be placed or injected into a porous media, followed by the addition of NPs designed for the remediation of that contaminant as well as image enhancement. Multiple X-ray CT scans over some length of time may then provide additional visual confirmation of mass removal, supplementing information obtained by traditional batch studies or column BTC studies to assess treatment effectiveness.

References

Abdul-Fatah, S.B., Zamburlini, M., Halders, S.G.E.A., Brans, B., Teule, G.J.J., Kemerink, G.J., 2009. Identification of a Shine-Through Artifact in the Trachea with 124I PET/CT. J. Nucl. Med. 50, 909–911. https://doi.org/10.2967/jnumed.108.060442

Abdulagatov, I.M., Zeinalova, A.B., Azizov, N.D., 2006. Viscosity of Aqueous Electrolyte Solutions at High Temperatures and High. J. Chem. Eng. Data 51, 1645–1659.

Aldana, M., Costanzo-Alvarez, V., Díaz, M., 2003. Magnetic and mineralogical studies to characterize oil reservoirs in Venezuela. Lead. Edge 22, 526–529. https://doi.org/10.1190/1.1587674

Ali-zade, R.A., 2011. Magnetization of Magnetite Nanoparticles Mediums with Weak Magnetic Dipole–Dipole Interaction. J. Nanosci. Nanotechnol. 11, 2496–2500. https://doi.org/10.1166/jnn.2011.3592

Allia, P., Tiberto, P., 2011. Dynamic effects of dipolar interactions on the magnetic behavior of magnetite nanoparticles. J. Nanoparticle Res. 13, 7277–7293. https://doi.org/10.1007/s11051-011-0642-2

Ameen, N.N., Klueglein, N., Appel, E., Petrovský, E., Kappler, A., Leven, C., 2014. Effect of hydrocarbon-contaminated fluctuating groundwater on magnetic properties of shallow sediments. Stud. Geophys. Geod. 58, 442–460. https://doi.org/10.1007/s11200-014-0407-3

An, C., Yan, B., Alfi, M., Mi, L., Killough, J.E., Heidari, Z., 2017. Estimating spatial distribution of natural fractures by changing NMR T2relaxation with magnetic nanoparticles. J. Pet. Sci. Eng. 157, 273–287. https://doi.org/10.1016/j.petrol.2017.07.030

Aslibeiki, B., Kameli, P., Salamati, H., 2013. The role of Ag on dynamics of superspins in MnFe2−x Ag x O4

nanoparticles. J. Nanoparticle Res. 15, 1430. https://doi.org/10.1007/s11051-013-1430-y

ASTM International, 2016. D5084-16a Standard Test Methods for Measurement of Hydraulic Conductivity of Saturated Porous Materials Using a Flexible Wall Permeameter.

ASTM International, 1985. Standard Test Methods for Specific Gravity of Coating Powders 1. https://doi.org/10.1520/D1429-08.2

Atekwana, E.A., Sauck, W.A., Abdel Aal, G.Z., Werkema, D.D., 2002. Geophysical Investigation of Vadose Zone Conductivity Anomalies at a Hydrocarbon Contaminated Site: Implications for the Assessment of Intrinsic Bioremediation. J. Environ. Eng. Geophys. 7, 103–110. https://doi.org/10.4133/JEEG7.3.103

Atekwana, E.A., Sauck, W.A., Werkema, D.D., 2000. Investigations of geoelectrical signatures at a hydrocarbon contaminated site. J. Appl. Geophys. 44, 167–180. https://doi.org/10.1016/S0926-9851(98)00033-0

Barry, D.A., 2009. Effect of nonuniform boundary conditions on steady flow in saturated homogeneous cylindrical soil columns. Adv. Water Resour. 32, 522–531. https://doi.org/10.1016/j.advwatres.2009.01.003

Batt, C., Fear, S., Heron, C., 1995. The role of magnetic susceptibility as a geophysical survey technique: A site assessment at high cayton, north yorkshire. Archaeol. Prospect. 2, 179–196. https://doi.org/10.1002/1099-0763(199512)2:4<179::AID-ARP6140020402>3.0.CO;2-K

Beaver, C.L., Williams, A.E., Atekwana, E.A., Mewafy, F.M., Abdel Aal, G., Slater, L.D., Rossbach, S., 2016. Microbial Communities Associated with Zones of Elevated Magnetic Susceptibility in Hydrocarbon-Contaminated Sediments. Geomicrobiol. J. 33, 441–452.

https://doi.org/10.1080/01490451.2015.1049676

Becker, M.D., Wang, Y., L. Paulsen, J., Song, Y.Q., Abriola, L.M., Pennell, K.D., 2015. In situ measurement and simulation of nano-magnetite mobility in porous media subject to transient salinity. Nanoscale 7, 1047–1057. https://doi.org/10.1039/c4nr05088f

Behroozmand, A.A., Keating, K., Auken, E., 2015. A Review of the Principles and Applications of the NMR Technique for Near-Surface Characterization. Surv. Geophys. 36, 27–85. https://doi.org/10.1007/s10712-014-9304-0

Bloch, F., 1946. Nuclear induction. Phys. Rev. 70, 460–474. https://doi.org/10.1103/PhysRev.70.460

Bloembergen, N., Purcrll, E.M., Pound, R. V, 1947. Relaxation effects in nuclear magnetic resonance absorption. Nat. Phys Rev 73, 679. https://doi.org/10.1103/PhysRev.73.679

Boaga, J., 2017. The use of FDEM in hydrogeophysics: A review. J. Appl. Geophys. 139, 36–46. https://doi.org/10.1016/j.jappgeo.2017.02.011

Böhm, G., Carcione, J.M., Gei, D., Picotti, S., Michelini, A., 2015. Cross-well seismic and electromagnetic tomography for CO2 detection and monitoring in a saline aquifer. J. Pet. Sci. Eng. 133, 245–257. https://doi.org/10.1016/j.petrol.2015.06.010

Bradford, J.H., 2007. Frequency-dependent attenuation analysis of ground-penetrating radar data. Geophys. Res. Lett. 72, J7–J16.

Bromly, M., Hinz, C., Aylmore, L.A.G., 2007. Relation of dispersivity to properties of homogeneous saturated repacked soil columns. Eur. J. Soil Sci. 58, 293–301. https://doi.org/10.1111/j.1365-2389.2006.00839.x

Brownstein, K.R., Tarr, C.E., 1979. Importance of classical diffusion in NMR studies of water in biological cells. Phys. Rev. A 19, 2446–2453. https://doi.org/10.1103/PhysRevA.19.2446

Bryar, T.R., Knight, R.J., 2008. NMR relaxation measurements to quantify immiscible organic contaminants in sediments. Water Resour. Res. 44, 1–10. https://doi.org/10.1029/2006WR005635

Bryar, T.R., Knight, R.J., 2003. Laboratory studies of the effect of sorbed oil on proton nuclear magnetic resonance. Geophysics 68, 942–948.

Buchau, A., Rucker, W.M., de Boer, C.V., Klaas, N., 2010. Inductive detection and concentration measurement of nano sized zero valent iron in the subsurface. IET Sci. Meas. Technol. 4, 289–297. https://doi.org/10.1049/iet-smt.2009.0116

Burger, H.R., Sheehan, A.F., Jones, C.H., 2006a. Electromagnetic Surveying, in: Wiegman, L. (Ed.), Introduction to Applied Geophsics. W. W. Norton & Company, New York, pp. 499–554.

Burger, H.R., Sheehan, A.F., Jones, C.H., 2006b. Exploration Using The Magnetic Method, in: Wiegman, L. (Ed.), Introduction to Applied Geophysics. W. W. Norton & Company, New York, pp. 429–497.

Burtman, V., Endo, M., Marsala, A., Zhdanov, M.S., 2015. Feasibility study of application of nanoparticles in complex resistivity (CR) reservoir monitoring. SEG Tech. Progr. Expand. Abstr. 34, 963–967. https://doi.org/10.1190/segam2015-5868400.1

Busch, J., Meißner, T., Potthoff, A., Bleyl, S., Georgi, A., Mackenzie, K., Trabitzsch, R., Werban, U., Oswald, S.E., 2015. A field investigation on transport of carbon-supported nanoscale zero-valent iron (nZVI) in groundwater. J. Contam. Hydrol. 181, 59–68. https://doi.org/10.1016/j.jconhyd.2015.03.009

Carcione, Seriani, 2000. An electromagnetic modelling tool for the detection of hydrocarbons in the subsoil. Geophys. Prospect. 48, 231–256. https://doi.org/10.1046/j.1365-2478.2000.00187.x

Cassidy, N.J., 2008. Frequency-dependent attenuation and velocity characteristics of nano-to-micro scale, lossy, magnetite-rich materials. Near Surf. Geophys. 6, 341–354.

Cassidy, N.J., 2007. Evaluating LNAPL contamination using GPR signal attenuation analysis and dielectric property measurements: Practical implications for hydrological studies. J. Contam. Hydrol. 94, 49–75. https://doi.org/10.1016/j.jconhyd.2007.05.002

Catapano, I., Affinito, A., Bertolla, L., Porsani, J.L., Soldovieri, F., 2014. Oil spill monitoring via microwave tomography enhanced GPR surveys. J. Appl. Geophys. 108, 95–103. https://doi.org/10.1016/j.jappgeo.2014.06.017

Chanzy, A., Tarussov, A., Judge, A., Bonn, F., 1996. Soil Water Content Determination Using a Digital Ground-Penetrating Radar. Soil Sci. Soc. Am. J. 60, 1318–1326.

Chowdhury, A.I.A., Krol, M.M., Kocur, C.M., Boparai, H.K., Weber, K.P., Sleep, B.E., O'Carroll, D.M., 2015. NZVI injection into variably saturated soils: Field and modeling study. J. Contam. Hydrol. 183, 16–28. https://doi.org/10.1016/j.jconhyd.2015.10.003

Clausnitzer, V., Hopmans, J.W., 2000. Pore-scale measurements of solute breakthrough using microfocus X-ray computed tomography. Water Resour. Res. 36, 2067–2079. https://doi.org/10.1029/2000WR900076

Cnudde, V., Boone, M.N., 2013. High-resolution X-ray computed tomography in geosciences: A review of the current technology and applications. Earth-Science Rev. 123, 1–17. https://doi.org/10.1016/j.earscirev.2013.04.003

Cnudde, V., Masschaele, B., Dierick, M., Vlassenbroeck, J., Hoorebeke, L. Van, Jacobs, P., 2006. Recent progress in X-ray CT as a geosciences tool. Appl. Geochemistry, Frontiers in Analytical Geochemistry–An IGC 2004 Perspective 21, 826–832. https://doi.org/10.1016/j.apgeochem.2006.02.010

Connell, D., Key, K., 2013. A numerical comparison of time and frequency-domain marine electromagnetic methods for hydrocarbon exploration in shallow water. Geophys. Prospect. 61, 187–199. https://doi.org/10.1111/j.1365-2478.2012.01037.x

Costanza-Robinson, M.S., Harrold, K.H., Lieb-Lappen, R.M., 2008. X-ray microtomography determination of air-water interfacial area-water saturation relationships in sandy porous media. Environ. Sci. Technol. 42, 2949–2956. https://doi.org/10.1021/es072080d

Culligan, K.A., Wildenschild, D., Christensen, B.S.B., Gray, W.G., Rivers, M.L., 2006. Pore-scale characteristics of multiphase flow in porous media: A comparison of air-water and oil-water experiments. Adv. Water Resour. 29, 227–238. https://doi.org/10.1016/j.advwatres.2005.03.021

Cussler, E.L., 2009. Diffusion Mass Transfer in Fluid Systems, 3rd ed. Cambridge University Press, Cambridge. https://doi.org/10.1017/CBO9780511805134

Delgado-Rodríguez, O., Flores-Hernández, D., Amezcua-Allieri, M.A., Rosas-Molina, A., Marín-Córdova, S., Shevnin, V., 2014. Joint interpretation of geoelectrical and volatile organic compounds data: a case study in a hydrocarbons contaminated urban site. Geofísica Int. 53, 183–198. https://doi.org/10.1016/S0016-7169(14)71499-0

Denison, D., Carlson, W.D., Ketchan, R.A., 1997. Three-dimensional quantitative textural analysis of metamorphic rocks using high-resolution computed X-ray tomography : Part I . Methods and

techniques. J. Metamorph. Geol. 15, 29–44.

Ding, Y., Liu, B., Shen, X., Zhong, L., Li, X., 2013. Foam-Assisted Delivery of Nanoscale Zero Valent Iron in Porous Media. J. Environ. Eng. 139, 1206–1212. https://doi.org/10.1061/(ASCE)EE.1943-7870.0000727

Donselaar, L.N., Philipse, A.P., 1999. Interactions between silica colloids with magnetite cores: Diffusion, sedimentation and light scattering. J. Colloid Interface Sci. 212, 14–23. https://doi.org/10.1006/jcis.1998.5931

Doolittle, J.A., Brevik, E.C., 2014. The use of electromagnetic induction techniques in soils studies. Geoderma 223–225, 33–45. https://doi.org/10.1016/j.geoderma.2014.01.027

Elliott, D.W., Zhang, W.X., 2001. Field assessment of nanoscale bimetallic particles for groundwater treatment. Environ. Sci. Technol. 35, 4922–4926. https://doi.org/10.1021/es0108584

Emmerton, S., Muxworthy, A.R., Sephton, M.A., Aldana, M., Costanzo-Alvarez, V., Bayona, G., Williams, W., 2013. Correlating biodegradation to magnetization in oil bearing sedimentary rocks. Geochim. Cosmochim. Acta 112, 146–165. https://doi.org/10.1016/j.gca.2013.03.008

Engineering ToolBox, 2009. Density of Selected Solids [WWW Document]. Eng. ToolBox. URL https://www.engineeringtoolbox.com/density-solids-d_1265.html (accessed 2.4.20).

Engineering ToolBox, 2004. Water - Dynamic and Kinematic Viscosity [WWW Document]. Eng. ToolBox. URL https://www.engineeringtoolbox.com/water-dynamic-kinematic-viscosity-d_596.html (accessed 4.27.20).

Engineering ToolBox, 2003. Water - Density, Specific Weight and Thermal Expansion Coefficient [WWW

Document]. URL https://www.engineeringtoolbox.com/water-density-specific-weight-d_595.html (accessed 1.28.20).

Estella a, A., Sauk, W.., Abdel Aal, G.., 2002. Geophysical investigation of vadose zone conductivity anomalies at a hydrocarbon contaminated site: Implications for the assesment of intrinsic bioremediation. Environ. Eng. Geophys. 7, 103–110. https://doi.org/10.4133/JEEG7.3.103

Everett, M.E., 2013a. Ground-penetrating radar, in: Near-Surface Applied Geophysics. Cambridge University Press, New York, pp. 254–293.

Everett, M.E., 2013b. Electromagnetic induction, in: Near-Surface Applied Geophysics. Cambridge University Press, New York, pp. 200–238.

Fay, E.L., Knight, R.J., 2016. Detecting and quantifying organic contaminants in sediments with nuclear magnetic resonance. Geophysics 81, EN87–EN97. https://doi.org/10.1190/geo2015-0647.1

Flowers, T.C., Hunt, J.R., 2007. Viscous and gravitational contributions to mixing during vertical brine transport in water-saturated porous media. Water Resour. Res. 43, 1–18. https://doi.org/10.1029/2005WR004773

Foote, R.S., 2007. Method helps find hydrocarbon areas, aids optimum seismic survey planning. Oil Gas Journal; 105, 35–40.

Frey, N.A., Phan, M.H., Srikanth, H., Srinath, S., Wang, C., Sun, S., 2009. Interparticle interactions in coupled Au–Fe3O4 nanoparticles. J. Appl. Phys. 105, 07B502. https://doi.org/10.1063/1.3056582

Ganguly, S., Sikdar, S., Basu, S., 2009. Experimental investigation of the effective electrical conductivity of aluminum oxide nanofluids. Powder Technol. 196, 326–330.

https://doi.org/10.1016/j.powtec.2009.08.010

Ge, L., Li, F., 2019. Review of in situ X-ray fluorescence analysis technology in China. X-Ray Spectrom. 1–13. https://doi.org/10.1002/xrs.3135

Gibert, O., Hernández, M., Vilanova, E., Cornellà, O., 2014. Guidelining protocol for soil-column experiments assessing fate and transport of trace organics, DEMEAU.

Godio, A., Naldi, M., 2009. Integration of Electrical and Electromagnetic Investigation for Contaminated Site. Am. J. Environ. Sci. 5, 561–568. https://doi.org/10.3844/ajessp.2009.561.568

Hashemi, R., Nassar, N.N., Pereira Almao, P., 2013. Enhanced heavy oil recovery by in situ prepared ultradispersed multimetallic nanoparticles: A study of hot fluid flooding for Athabasca bitumen recovery. Energy and Fuels 27, 2194–2201. https://doi.org/10.1021/ef3020537

He, F., Zhao, D., 2008. Hydrodechlorination of trichloroethene using stabilized Fe-Pd nanoparticles: Reaction mechanism and effects of stabilizers, catalysts and reaction conditions. Appl. Catal. B Environ. 84, 533–540. https://doi.org/10.1016/j.apcatb.2008.05.008

He, F., Zhao, D., 2007. Manipulating the size and dispersibility of zerovalent iron nanoparticles by use of carboxymethyl cellulose stabilizers. Environ. Sci. Technol. 41, 6216–6221. https://doi.org/10.1021/es0705543

He, F., Zhao, D., 2005. Preparation and characterization of a new class of starch-stabilized bimetallic nanoparticles for degradation of chlorinated hydrocarbons in water. Environ. Sci. Technol. 39, 3314–3320. https://doi.org/10.1021/es048743y

He, F., Zhao, D., Liu, J., Roberts, C.B., 2007. Stabilization of Fe - Pd nanoparticles with sodium

carboxymethyl cellulose for enhanced transport and dechlorination of trichloroethylene in soil and groundwater. Ind. Eng. Chem. Res. 46, 29–34. https://doi.org/10.1021/ie0610896

Hedberg, S.A., Knight, R.J., MacKay, A.L., Whittall, K.P., 1993. The use of nuclear magnetic resonance for studying and detecting hydrocarbon contaminants in porous rocks. Water Resour. Res. 29, 1163–1170. https://doi.org/10.1029/92WR02540

Heimovaara, T.J., de Winter, E.J.G., van Loon, W.K.P., Esveld, D.C., 1996. Frequency-Dependent Dielectric Permittivity from 0 to 1 GHz: Time Domain Reflectometry Measurements Compared with Frequency Domain Network Analyzer Measurements. Water Resour. Res. 32, 3603–3610. https://doi.org/10.1029/96WR02695

Hertrich, M., 2008. Imaging of groundwater with nuclear magnetic resonance. Prog. Nucl. Magn. Reson. Spectrosc. 53, 227–248. https://doi.org/10.1016/j.pnmrs.2008.01.002

Hill, S., P, F.I., 1952. Channeling in packed columns. Chem. Eng. Sci. 1, 247–253. https://doi.org/10.1016/0009-2509(52)87017-4

Hizem, M., Budan, H., Devillé, B., Faivre, O., Mossé, L., Simon, M., 2008. Dielectric Dispersion : A New Wireline Petrophysical Measurement. Spe SPE 116130, 21–24. https://doi.org/10.2118/116130-MS

Hrubovčák, P., Zeleňáková, A., Zeleňák, V., Kováč, J., 2015. The study of magnetic properties and relaxation processes in Co/Au bimetallic nanoparticles. J. Alloys Compd. 649, 104–111. https://doi.org/10.1016/j.jallcom.2015.07.044

Hu, J.D., Zevi, Y., Kou, X.M., Xiao, J., Wang, X.J., Jin, Y., 2010. Effect of dissolved organic matter on the stability of magnetite nanoparticles under different pH and ionic strength conditions. Sci. Total Environ. 408, 3477–3489. https://doi.org/10.1016/j.scitotenv.2010.03.033

Hu, Y., Yu, Z., Zhang, W., Sun, Q., Liu, Q.H., 2016. Multiphysics Coupling of Dynamic Fluid Flow and Electromagnetic Fields for Subsurface Sensing. IEEE J. Multiscale Multiphysics Comput. Tech. 1, 14–25. https://doi.org/10.1109/JMMCT.2016.2559509

Hunter, A.K., McDavid, W.D., 2012. Characterization and correction of cupping effect artefacts in cone beam CT. Dentomaxillofacial Radiol. 41, 217–223. https://doi.org/10.1259/dmfr/19015946

Javadpour, F., Nicot, J.P., 2011. Enhanced CO2Storage and Sequestration in Deep Saline Aquifers by Nanoparticles: Commingled Disposal of Depleted Uranium and CO2. Transp. Porous Media 89, 265–284. https://doi.org/10.1007/s11242-011-9768-z

Johnson, R.L., Nurmi, J.T., Johnson, G.S.O.B., Fan, D., Johnson, R.L.O.B., Shi, Z., Salter-blanc, A.J., Tratnyek, P.G., Lowry, G. V, 2013. Field-Scale Transport and Transformation of Carboxymethylcellulose-Stabilized Nano Zero-Valent Iron.

Jung, B., O'Carroll, D., Sleep, B., 2014. The influence of humic acid and clay content on the transport of polymer-coated iron nanoparticles through sand. Sci. Total Environ. 496, 155–164. https://doi.org/10.1016/j.scitotenv.2014.06.075

Karn, B., Kuiken, T., Otto, M., 2009. Nanotechnology and in situ remediation: A review of the benefits and potential risks. Environ. Health Perspect. 117, 1823–1831. https://doi.org/10.1289/ehp.0900793

Klueglein, N., Lösekann-Behrens, T., Obst, M., Behrens, S., Appel, E., Kappler, A., 2013. Magnetite Formation by the Novel Fe(III)-reducing Geothrix fermentans Strain HradG1 Isolated from a Hydrocarbon-Contaminated Sediment with Increased Magnetic Susceptibility. Geomicrobiol. J. 30, 863–873. https://doi.org/10.1080/01490451.2013.790922

Kmetz, A.A., Becker, M.D., Lyon, B.A., Foster, E., Xue, Z., Johnston, K.P., Abriola, L.M., Pennell, K.D., 2016. Improved Mobility of Magnetite Nanoparticles at High Salinity with Polymers and Surfactants. Energy and Fuels 30, 1915–1926. https://doi.org/10.1021/acs.energyfuels.5b01785

Knight, R., 2001. GROUND PENETRATING RADAR FOR ENVIRONMENTAL APPLICATIONS. Annu. Rev. Earth Planet. Sci. 29, 229–255.

Knoll, G.F., 2005. Radiation Detection and Measurement (Hardcover). Book.

Kocur, C.M., Chowdhury, A.I., Sakulchaicharoen, N., Boparai, H.K., Weber, K.P., Sharma, P., Krol, M.M., Austrins, L., Peace, C., Sleep, B.E., O'Carroll, D.M., 2014. Characterization of nZVI mobility in a field scale test. Environ. Sci. Technol. 48, 2862–2869. https://doi.org/10.1021/es4044209

Kotsmar, C., Yoon, K.Y., Yu, H., Ryoo, S.Y., Barth, J., Shao, S., Prodanović, M., Milner, T.E., Bryant, S.L., Huh, C., Johnston, K.P., 2010. Stable Citrate-Coated Iron Oxide Superparamagnetic Nanoclusters at High Salinity 49, 12435–12443. https://doi.org/10.1021/ie1010965

Kuiken, T., 2010. Cleaning up contaminated waste sites: Is nanotechnology the answer? Nano Today 5, 6–8. https://doi.org/10.1016/j.nantod.2009.11.001

Lecoanet, H.F., Bottero, J.Y., Wiesner, M.R., 2004. Laboratory assessment of the mobility of nanomaterials in porous media. Environ. Sci. Technol. 38, 5164–5169. https://doi.org/10.1021/es0352303

Lewis, J., Sjöstrom, J., 2010. Optimizing the experimental design of soil columns in saturated and unsaturated transport experiments. J. Contam. Hydrol. 115, 1–13. https://doi.org/10.1016/j.jconhyd.2010.04.001

Linley, S., Holmes, A., Leshuk, T., Nafo, W., Thomson, N.R., Al-mayah, A., Mcvey, K., Sra, K., Gu, F.X., 2019a. Targeted nanoparticle binding & detection in petroleum hydrocarbon impacted porous media. Chemosphere 215, 353–361. https://doi.org/10.1016/j.chemosphere.2018.10.046

Linley, S., Thomson, N.R., McVey, K., Sra, K., Gu, F.X., 2020. Factors affecting pluronic-coated iron oxide nanoparticle binding to petroleum hydrocarbon-impacted sediments. Chemosphere 254, 126732. https://doi.org/10.1016/j.chemosphere.2020.126732

Linley, S., Thomson, N.R., McVey, K., Sra, K., Gu, F.X., 2019b. Influence of Pluronic coating formulation on iron oxide nanoparticle transport in natural and oil-impacted sandy aquifer media. Can. J. Chem. Eng. 98, 642–649. https://doi.org/10.1002/cjce.23650

Liu, Q., Roberts, A.P., Larrasoaña, J.C., Banerjee, S.K., Guyodo, Y., Tauxe, L., Oldfield, F., 2012. Environmental magnetism: Principles and applications. Rev. Geophys. 50, RG4002. https://doi.org/10.1029/2012RG000393

Liu, W., Tian, S., Zhao, X., Xie, W., Gong, Y., Zhao, D., 2015. Application of Stabilized Nanoparticles for In Situ Remediation of Metal-Contaminated Soil and Groundwater: a Critical Review. Curr. Pollut. Reports 1, 280–291. https://doi.org/10.1007/s40726-015-0017-x

Mansi, A.H., Castillo, M.P., Bernasconi, G., 2002. Controlled Laboratory Test for the Investigation of LNAPL Contamination Using a 2.0 GHz Ground-Penetrating Radar. Boll. di Geofis. Teor. ed Appl. 58, 169–180. https://doi.org/10.4430/bgta0197

Mar Gil-Díaz, M., Pérez-Sanz, A., Ángeles Vicente, M., Carmen Lobo, M., 2014. Immobilisation of Pb and Zn in soils using stabilised zero-valent iron nanoparticles: Effects on soil properties. Clean - Soil, Air, Water 42, 1776–1784. https://doi.org/10.1002/clen.201300730

Matott, L.-, 2013. OSTRICH – An Optimization Software Toolkit for Research Involving Computational Heuristics Documentation and User ' s Guide.

Mazáč, O., Benes, L., Landa, I., Maškova, A., 1990. 11. Determination of the Extent of Oil Contamination in Groundwater by Geoelectrical Methods, in: Ward, S.H. (Ed.), Geotechnical and Environmental Geophysics. pp. 107–112.

McNeill, J., 1980. Electromagnetic Terrain Conductivity Measurment at Low Induction Numbers. Mississauga.

Medvedeva, I. V., Zhakov, S. V., Revvo, A. V., Byzov, I. V., Bakhteeva, Y.A., Uimin, M.A., Yermakov, A.E., Mysik, A.A., 2014. Application of NMR relaxometry for determining the concentration of nanopowder magnetite in aqueous media. Phys. Met. Metallogr. 115, 744–748. https://doi.org/10.1134/S0031918X14080110

Mehta, D., Hawley, M.C., 1969. Wall effect in packed columns. Ind. Eng. Chem. Process Des. Dev. 8, 280–282. https://doi.org/10.1021/i260030a021

Menand, T., Woods, A.W., 2005. Dispersion, scale, and time dependence of mixing zones under gravitationally stable and unstable displacements in porous media. Water Resour. Res. 41, 1–13. https://doi.org/10.1029/2004WR003701

Menshov, O., Kuderavets, R., Vyzhva, S., Chobotok, I., Pastushenko, T., 2015. Magnetic mapping and soil magnetometry of hydrocarbon prospective areas in western Ukraine. Stud. Geophys. Geod. 59, 614–627. https://doi.org/10.1007/s11200-015-0705-4

Menshov, O., Kuderavets, R., Vyzhva, S., Maksymchuk, V., Chobotok, I., Pastushenko, T., 2016. Magnetic studies at Starunia paleontological and hydrocarbon bearing site (Carpathians, Ukraine). Stud.

Geophys. Geod. 60, 731–746. https://doi.org/10.1007/s11200-016-0621-2

Monteiro Santos, F.A., Mateus, A., Figueiras, J., Gonçalves, M.A., 2006. Mapping groundwater contamination around a landfill facility using the VLF-EM method — A case study. J. Appl. Geophys. 60, 115–125. https://doi.org/10.1016/j.jappgeo.2006.01.002

Morrow, L., Potter, D.K., Barron, A.R., 2015. Detection of magnetic nanoparticles against proppant and shale reservoir rocks. J. Exp. Nanosci. 10, 1028–1041. https://doi.org/10.1080/17458080.2014.951412

Mueller, N.C., Braun, J., Bruns, J., Černík, M., Rissing, P., Rickerby, D., Nowack, B., 2012. Application of nanoscale zero valent iron (NZVI) for groundwater remediation in Europe. Environ. Sci. Pollut. Res. 19, 550–558. https://doi.org/10.1007/s11356-011-0576-3

Mystrioti, C., Papassiopi, N., Xenidis, A., Dermatas, D., Chrysochoou, M., 2015. Column study for the evaluation of the transport properties of polyphenol-coated nanoiron. J. Hazard. Mater. 281, 64–69. https://doi.org/10.1016/j.jhazmat.2014.05.050

Nsugbe, E., Starr, A., Foote, P., Ruiz-Carcel, C., Jennions, I., 2016. Size Differentiation of A Continuous Stream of Particles Using Acoustic Emissions. IOP Conf. Ser. Mater. Sci. Eng. 161. https://doi.org/10.1088/1757-899X/161/1/012090

Oliviera, I.B., Demond, A.H., Salehzadeh, A., 1996. Packing of sands for the production of homogeneous porous media. Soil Sci. Soc. Am. J. 60, 49–53. https://doi.org/10.2136/sssaj1996.03615995006000010010x

Parsekian, A.D., Grosse, G., Walbrecker, J.O., Müller-Petke, M., Keating, K., Liu, L., Jones, B.M., Knight, R., 2013. Detecting unfrozen sediments below thermokarst lakes with surface nuclear magnetic

resonance. Geophys. Res. Lett. 40, 535–540. https://doi.org/10.1002/grl.50137

Petrovic, A.M., Siebert, J.E., Rieke, P.E., 1982. Soil Bulk Density Analysis in Three Dimensions by Computed Tomographic Scanning. Soil Sci. Soc. Am. J. 46, 445–450. https://doi.org/10.2136/sssaj1982.03615995004600030001x

Phenrat, T., Liu, Y., Tilton, R.D., Lowry, G. V., 2009. Adsorbed polyelectrolyte coatings decrease Fe o nanoparticle reactivity with TCE in water: Conceptual model and mechanisms. Environ. Sci. Technol. 43, 1507–1514. https://doi.org/10.1021/es802187d

Phenrat, T., Saleh, N., Sirk, K., Tilton, R.D., Lowry, G. V., 2007. Aggregation and sedimentation of aqueous nanoscale zerovalent iron dispersions. Environ. Sci. Technol. 41, 284–290. https://doi.org/10.1021/es061349a

Piacenza, E., Presentato, A., Turner, R.J., 2018. Stability of biogenic metal(loid) nanomaterials related to the colloidal stabilization theory of chemical nanostructures. Crit. Rev. Biotechnol. 38, 1137–1156. https://doi.org/10.1080/07388551.2018.1440525

Ponder, S.M., Darab, J.G., Bucher, J., Caulder, D., Craig, I., Davis, L., Edelstein, N., Lukens, W., Nitsche, H., Rao, L., Shuh, D.K., Mallouk, T.E., 2001. Surface chemistry and electrochemistry of supported zerovalent iron nanoparticles in the remediation of aqueous metal contaminants. Chem. Mater. 13, 479–486. https://doi.org/10.1021/cm000288r

Porsani, J.L., Filho, W.M., Elis, V.R., Shimeles, F., Dourado, J.C., Moura, H.P., 2004. The use of GPR and VES in delineating a contamination plume in a landfill site: A case study in SE Brazil. J. Appl. Geophys. 55, 199–209. https://doi.org/10.1016/j.jappgeo.2003.11.001

Porsch, K., Rijal, M.L., Borch, T., Troyer, L.D., Behrens, S., Wehland, F., Appel, E., Kappler, A., 2014.

Impact of organic carbon and iron bioavailability on the magnetic susceptibility of soils. Geochim. Cosmochim. Acta 128, 44–57. https://doi.org/10.1016/j.gca.2013.12.001

Porter, M.L., Wildenschild, D., Grant, G., Gerhard, J.I., 2010. Measurement and prediction of the relationship between capillary pressure, saturation, and interfacial area in a NAPL-water-glass bead system. Water Resour. Res. 46, 1–10. https://doi.org/10.1029/2009WR007786

Rahmani, A.R., Athey, A.E., Chen, J., Wilt, M.J., 2014. Sensitivity of dipole magnetic tomography to magnetic nanoparticle injectates. J. Appl. Geophys. 103, 199–214. https://doi.org/10.1016/j.jappgeo.2014.01.019

Rahmani, A.R., Bryant, S., Huh, C., Athey, A., Ahmadian, M., Chen, J., Wilt, M., 2015. Crosswell Magnetic Sensing of Superparamagnetic Nanoparticles for Subsurface Applications. SPE J. 20, 1067–1082. https://doi.org/10.2118/166140-PA

Raveendran, P., Fu, J., Wallen, S.L., 2003. Completely “Green” Synthesis and Stabilization of Metal Nanoparticles. J. Am. Chem. Soc. 125, 13940–13941. https://doi.org/10.1021/ja029267j

Reyes-López, J.A., Ramírez-Hernández, J., Lázaro-Mancilla, O., Carreón-Diazconti, C., Garrido, M.M.L., 2008. Assessment of groundwater contamination by landfill leachate: A case in México. Waste Manag. 28, 33–39. https://doi.org/10.1016/j.wasman.2008.03.024

Rijal, M.L., Porsch, K., Appel, E., Kappler, A., 2012. Magnetic signature of hydrocarbon-contaminated soils and sediments at the former oil field Hänigsen, Germany. Stud. Geophys. Geod. 56, 889–908. https://doi.org/10.1007/s11200-010-0040-8

Saleh, N., Phenrat, T., Sirk, K., Dufour, B., Ok, J., Sarbu, T., Matyjaszewski, K., Tilton, R.D., Lowry, G. V., 2005. Adsorbed triblock copolymers deliver reactive iron nanoparticles to the oil/water interface.

Nano Lett. 5, 2489–2494. https://doi.org/10.1021/nl0518268

Senturia, S.D., Robinson, J.D., 1970. Nuclear Spin-Lattice Relaxation of Liquids Confined in Porous Solids. Soc. Pet. Eng. J. 10, 237–244. https://doi.org/10.2118/2870-PA

Shen, X., Zhao, L., Ding, Y., Liu, B., Zeng, H., Zhong, L., Li, X., 2011. Foam, a promising vehicle to deliver nanoparticles for vadose zone remediation. J. Hazard. Mater. 186, 1773–1780. https://doi.org/10.1016/j.jhazmat.2010.12.071

Shushakov, O. a., 1996. Groundwater NMR in conductive water. Geophysics 61, 998–1006. https://doi.org/10.1190/1.1444048

Solanki, J.N., Murthy, Z.V.P., 2011. Preparation of Silver Nanofluids with High Electrical Conductivity. J. Dispers. Sci. Technol. 32, 724–730. https://doi.org/10.1080/01932691.2010.480863

Stromberg, J., Spinks, S., Pearce, M., 2019. Characterisation of the Neoarchean Fortescue Group Stratigraphy – Integrated downhole geochemical mineralogical correlation from new diamond drilling. ASEG Ext. Abstr. 2019, 1–4. https://doi.org/10.1080/22020586.2019.12073203

Taina, I.A., Heck, R.J., Elliot, T.R., 2008. Application of X-ray computed tomography to soil science: A literature review. Can. J. Soil Sci. 88, 1–20. https://doi.org/10.4141/cjss06027

Telford, W.M., Geldart, L.P., Sheriff, R.E., 1990. Magnetic Methods, in: Applied Geophysics. Press Syndicate of the University of Cambridge, New York, pp. 62–134.

Terraplus, 2013. KT-20 Magnetic Susceptibility/Conductivity/IP-Resistivity Meter.

Thomé, A., Reddy, K.R., Reginatto, C., Cecchin, I., 2015. Review of nanotechnology for soil and groundwater remediation: Brazilian perspectives. Water. Air. Soil Pollut. 226, 1–20.

https://doi.org/10.1007/s11270-014-2243-z

Thomson, N.R., 2019. 1-DUSAT.

Tiraferri, A., Sethi, R., 2009. Enhanced transport of zerovalent iron nanoparticles in saturated porous media by guar gum. J. Nanoparticle Res. 11, 635–645. https://doi.org/10.1007/s11051-008-9405-0

Topp, G.C., Davis, J.L., Annan, A.P., 1980. Electromagnetic determination of soil water content: Measurements in coaxial transmission lines. Water Resour. Res. 16, 574–582. https://doi.org/10.1029/WR016i003p00574

Tratnyek, P.G., Salter-Blanc, A.J., Nurmi, J.T., Amonette, J.E., Liu, J., Wang, C., Dohnalkova, A., Baer, D.R., 2011. Reactivity of zerovalent metals in aquatic media: Effects of organic surface coatings. ACS Symp. Ser. 1071, 381–406. https://doi.org/10.1021/bk-2011-1071.ch018

van Berkum, S., Dee, J., Philipse, A., Erné, B., 2013. Frequency-Dependent Magnetic Susceptibility of Magnetite and Cobalt Ferrite Nanoparticles Embedded in PAA Hydrogel. Int. J. Mol. Sci. 14, 10162–10177. https://doi.org/10.3390/ijms140510162

Volume Graphics GmbH, 2001. VGStudio Max 1.0 User's Manual. https://doi.org/10.1017/CBO9781107415324.004

Walsh, D.O., 2008. Multi-channel surface NMR instrumentation and software for 1D/2D groundwater investigations. J. Appl. Geophys. 66, 140–150. https://doi.org/10.1016/j.jappgeo.2008.03.006

Wang, C.B., Zhang, W.X., 1997. Synthesizing nanoscale iron particles for rapid and complete dechlorination of TCE and PCBs. Environ. Sci. Technol. 31, 2154–2156. https://doi.org/10.1021/es970039c

Wellington, S.L., Vinegar, H.J., 1987. X-ray computerized tomography. J. Pet. Tech. 885–898.

Wijewardana, N.S., Galagedara, L.W., Mowjood, M.I.M., 2012. Assessment of groundwater contamination by landfill leachate with ground penetrating radar, in: 14th International Conference on Ground Penetrating Radar (GPR). pp. 728–732.

Wilt, M.J., Alumbaugh, D.L., Morrison, H.F., Becker, A., Lee, K.H., Deszcz-Pan, M., 1995. Crosswell electromagnetic tomography: System design considerations and field results. GEOPHYSICS 60, 871–885. https://doi.org/10.1190/1.1443823

Xue, Z., Foster, E., Wang, Y., Nayak, S., Cheng, V., Ngo, V.W., Pennell, K.D., Bielawski, C.W., Johnston, K.P., 2014. Effect of grafted copolymer composition on iron oxide nanoparticle stability and transport in porous media at high salinity. Energy and Fuels 28, 3655–3665. https://doi.org/10.1021/ef500340h

Yoon, K.Y., Xue, Z., Fei, Y., Lee, J.H., Cheng, V., Bagaria, H.G., Huh, C., Bryant, S.L., Kong, S.D., Ngo, V.W., Rahmani, A.-R., Ahmadian, M., Ellison, C.J., Johnston, K.P., 2016. Control of magnetite primary particle size in aqueous dispersions of nanoclusters for high magnetic susceptibilities. J. Colloid Interface Sci. 462, 359–367. https://doi.org/10.1016/j.jcis.2015.09.058

Zhang, C., Suekane, T., Minokawa, K., Hu, Y., Patmonoaji, A., 2019. Solute transport in porous media studied by lattice Boltzmann simulations at pore scale and x-ray tomography experiments. Phys. Rev. E 100, 63110. https://doi.org/10.1103/PhysRevE.100.063110

Zhu, C., Daigle, H., Bryant, S.L., 2016. Paramagnetic nanoparticles as nuclear magnetic resonance contrast agents in sandstone: Importance of nanofluid-rock interactions. Interpretation 4, SF55–SF65. https://doi.org/10.1190/INT-2015-0137.1

Zia, S., Wenyong, D., Spreer, W., He, X., Muller, J., 2010. Mapping of soil salinity and clay content based electromagnetic induction measurments by EM38, in: XVIIthWorld Congress of the International Commission of Agricultural and Biosystems Engineering (CIGR). Quebec City, p. 10.

Appendices

Appendix A: Supplementary Literature Information

A-1 Stabilization of Nanoparticles

In general, NP stabilizers can be broken into three categories, surfactants, polymers, and polyelectrolytes (Busch et al., 2015). All these compounds work to prevent NP aggregation either through steric (i.e., entropic stabilization due to particle "crowding"), electrostatic (i.e., Columbic repulsion effects), or electrosteric stabilization (i.e., a combination of the two effects). A more detailed discussion of these stabilization mechanisms can be found in work by Piacenza, Presentato, and Turner (2018) (Piacenza et al., 2018). Figure A 1 schematically illustrates these stabilization mechanisms.

Stabilizers can be applied to NPs either before the formation of any NP aggregates, or after aggregates have formed (i.e., applying surface modifications to re-disperse the particles), known as pre-agglomeration stabilization or post agglomeration stabilization respectively (He and Zhao, 2007). The method by which stabilizers are added to NPs has been found to influence particle size and reactivity. For instance, He and Zhao (2008) found that palladized nZVI synthesized in CMC solution (pre-agglomeration stabilization) resulted in enhanced TCE degradation (He and Zhao, 2008). Phenrat et al. (2009) found that palladized nZVI stabilized in CMC solution after synthesis (post-agglomeration stabilization) resulted in decreased reactivity of the NPs with TCE (Phenrat et al., 2009). Phenrat et al. note that this contrast in results could be due to the smaller particle sizes achieved by the pre-agglomeration synthesis used by He and Zhao and due to the blocking of reactive sites by the physiosorbed CMC. A further benefit of pre-agglomeration stabilization is the potential to control particle size and thus reactivity (He and Zhao, 2007).

Most stabilizers studied are polymers or polyelectrolytes. These include polyethylene glycols, sodium polyasparate, polystyrene sulfonate, poly(2-acrylamido-2-methyl-1-proanesulfonic acid) (PAMPS),-PAMPS-acrylic acid (PAMPS-AA) copolymer, and poly(methacrylic acid)-block-poly(methyl methacrylate)-block-poly(styrenesulfonate) tri-block copolymers (Becker et al., 2015; Ding et al., 2013; Kmetz et al., 2016; Phenrat et al., 2009; Raveendran et al., 2003; Saleh et al., 2005; Shen et al., 2011; Xue et al., 2014). Furthermore, many natural "biopolymers" have also attracted interest, particularly (CMC) which has been studied at both the lab and field scale (Busch et al., 2015; Chowdhury et al., 2015; He et al., 2007; He and Zhao, 2008; Johnson et al., 2013; Kocur et al., 2014; Phenrat et al., 2009). Biopolymers are attractive due to their relatively low cost, biodegradability, and low toxicity (Tratnyek et al., 2011). Other biopolymers that have been studied include polyphenol (green tea extract), starch, citrate, guar gum, gum Arabic and hydroxyethyl cellulose (He and Zhao, 2005; Kmetz et al., 2016; Kotsmar et al., 2010; Mystrioti et al., 2015; Tiraferri and Sethi, 2009). Finally, several surfactants have also been used for iron NP stabilization, such as dodecylbenzene sulfonic acid, sodium lauryl ether sulfate, and sodium dodecyl sulfate (Ding et al., 2013; Lecoanet et al., 2004; Shen et al., 2011). These stabilizers have all found varying degrees of success under different conditions.

The stability of NPs for subsurface applications is typically assessed by the duration for which they can remain in suspension without agglomerating and settling. Many studies have reported that non-stabilized iron NPs (including Fe/Pd, nMag, and nZVI) aggregate and settle from solution within a matter of minutes due primarily to Van der Waals or magnetic attraction forces between particles (He and Zhao, 2005; Kotsmar et al., 2010; Phenrat et al., 2007). However, stabilized NPs have been found to remain in solution on the scale of days to months Green tea extract supported nZVI particles (GT-nZVI) have been reported to be stable in an aqueous solution for greater than 10 days (Mystrioti et al., 2015).

Further, nMag supported with PAMPs and PAMPS-AA have been found to remain stable in API brine solutions (8 wt % NaCl + 2 wt% $CaCl_2$ (Kmetz et al., 2016)) for 1 to 3 months (Becker et al., 2015; Kotsmar et al., 2010).

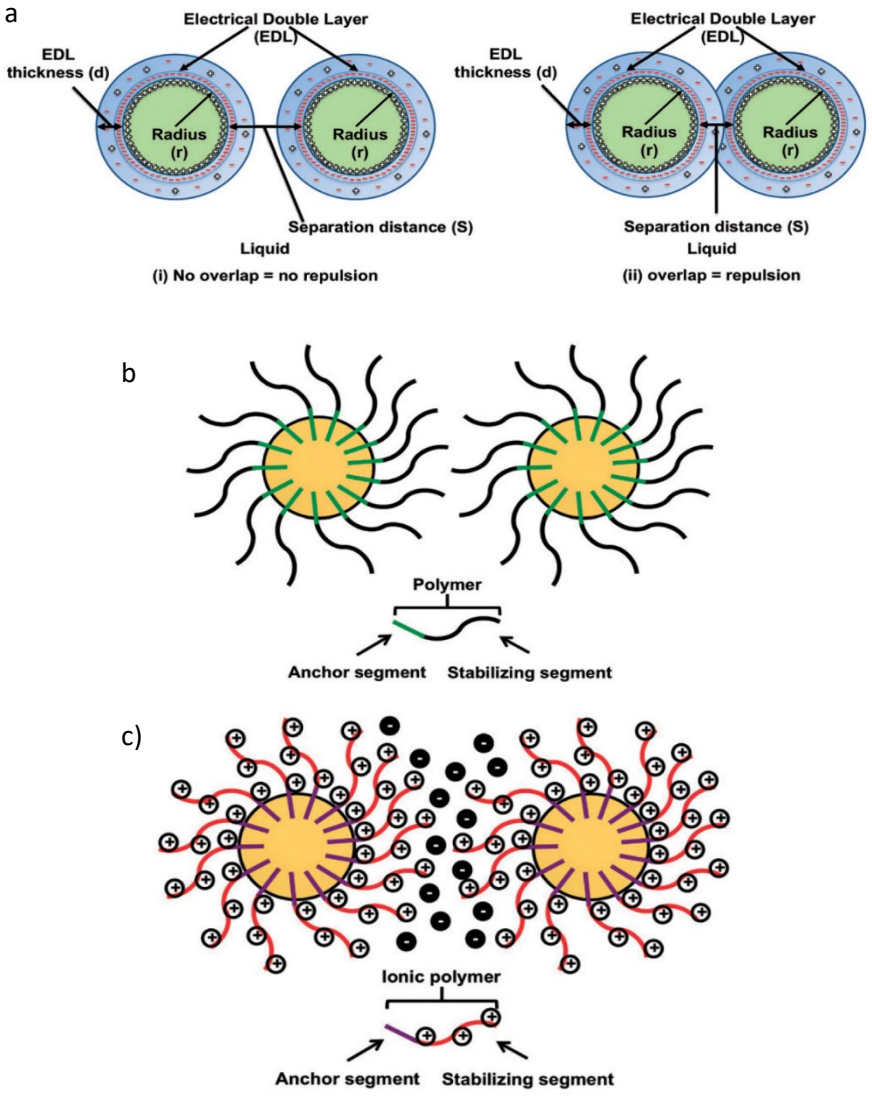

Figure A 1: Schematic illustration of a) electrostatic repulsion forces that arise between particles with like surface charges as they approach each other b) the steric repulsion that arises from the adsorption of polymers onto NP surfaces and c) electrosteric stabilization from the combined effects of electrostatic

and steric repulsion forces that arise from polyelectrolytes that are adsorbed onto NP surfaces. The schematics here were originally generated by Piacenza et al. (2018).

Several factors have been found to influence NP stability in solution. Saleh et al. (2005) showed that a higher degree of polymerization resulted in increased stabilization of nZVI particles that were surface modified by a tri-block copolymer (Saleh et al., 2005). Kotsmar et al. studied the effects of pH and salinity on the stability of citrate stabilized iron oxide NPs(Kotsmar et al., 2010). Solutions with NP concentrations of 0.1 wt % were prepared with salinities ranging from 0.1-4 wt % (ionic strength of 0.017M to 0.683 M) and pH values between 6-10. The NPs were found to be stable at pH values of 6 and 8 in salinity of 3.5% for 2 and 3 months, respectively. They were found to aggregate into a gel that could not be redisposed with sonication within 5 minutes at a pH of 10 and a salinity of only 0.5%. Interestingly, the hydrodynamic diameters of the NPs were found to increase in size with increasing salinity at a pH of 8 but were found to change very little at a pH of 6. The surface charge potential of the NPs was measured and found to be related to pH. The coated particles exhibited potentials between 35 and -55 mV between pH values of 6-10, with a zero-charge occurring approximately at a pH of 2. Conversely, equivalent non-stabilized NPs were found to have a zero-charge value at a pH of approximately 7. The authors note that while it is surprising that the NPs remained stable at high salinities, it is possible that forces from specific ion adsorption in the Stern layer of the electric double layer and hydration were sufficient to maintain the stability of the particles at a pH of 6 an 8. However, at a pH of 10, the growth of the nanoclusters was too large, and thus these forces were not strong enough to keep the particles in suspension. Finally, background environmental, such as clay content, the presence of humic acid, and dissolved oxygen content have also been found to affect NP stability (Ding et al., 2013; Hu et al., 2010; Jung et al., 2014; Ponder et al., 2001).

A-2 Magnetic Susceptibility of Geologic Material

Table A 1: Magnetic Susceptibility of Geologic Material, adapted from (Telford et al., 1990).

Category	Material	Susceptibility Range (unitless)	Susceptibility average (unitless)
Sedimentary	Dolomite	0—0.9	0.1
	Limestones	0—3	0.3
	Sandstones	0—20	0.4
	Shales	0.01—15	0.6
	Av. 48 Sedimentary	0—70	0.9
Metamorphic	Schist	0.3—3	1.4
	Gneiss	0.1—25	
	Quartzite	—	4
	Serpentine	3—17	
	Slate	0—35	6
	Av. 61 Metamorphic	0—70	4.2
Igneous	Granite	0—50	2.5
	Rhyolite	0.2—35	-
	Dolerite	1—35	17
	Augite-Syenite	30—40	—
	Diabase	1—160	55
	Porphyry	0.3—200	60
	Gabbro	1—90	70
	Basalts	0.2—175	70
	Diorite	0.6—120	85
	Peridotite	90—200	150
	Andesite	—	160
	Av. Acidic Igneous	0—80	8
	Av. Basic Igneous	0.5—97	25
Minerals	Graphite	—	0.1
	Quartz	—	-0.01
	Rock Salt	—	-0.01
	Anhydrite, gypsum	—	-0.01
	Calcite	-0.001—0.01	—
	Coal	—	0.02
	Clays	—	0.2
	Chalcopyrite	—	0.4
	Sphalerite	—	0.7
	Cassiterite	—	0.9
	Siderite	1—4	—
	Pyrite	0.05—5	1.5
	Limonite	—	2.5
	Arsenopyrite	—	3
	Hematite	0.5—35	6.5
	Chromite	3—110	7
	Franklinite	—	430

	Pyrrhotite	1—6000	1500
	Ilmenite	300—3500	1800
	Magnetite	1200—192000	6000

Appendix B: Additional Experimental Information

B-1 NaI Calibration Curve

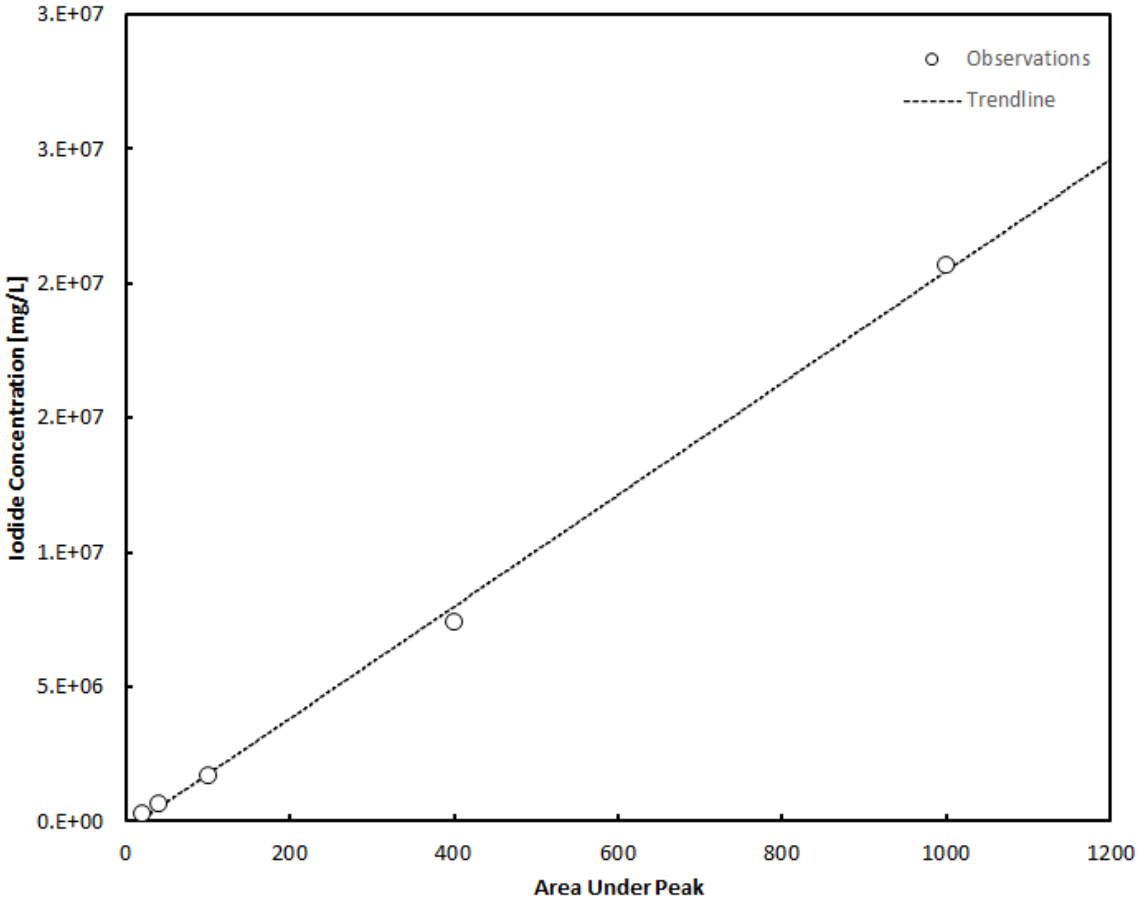

Figure B 1: Average IC NaI calibration curve showing trendline with an R^2 value of 0.9985.

B-2 Bromide BTCs and OSTRICH Modeling Results

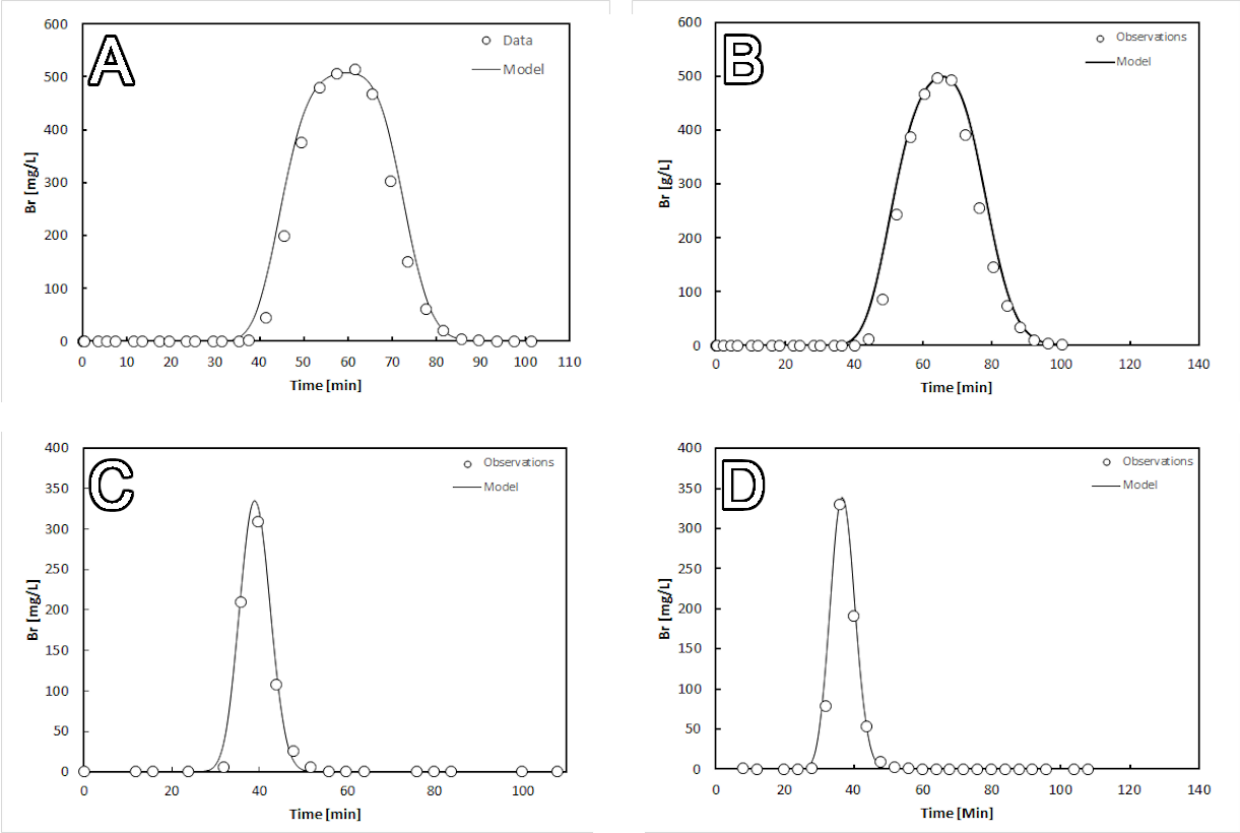

Figure B 2: Br tracer BTCs observations and 1-DUSAT modeling results showing (A) Br-1-A, (B) Br-1-B, (C) Br-2-A, and (D) Br-2-B.

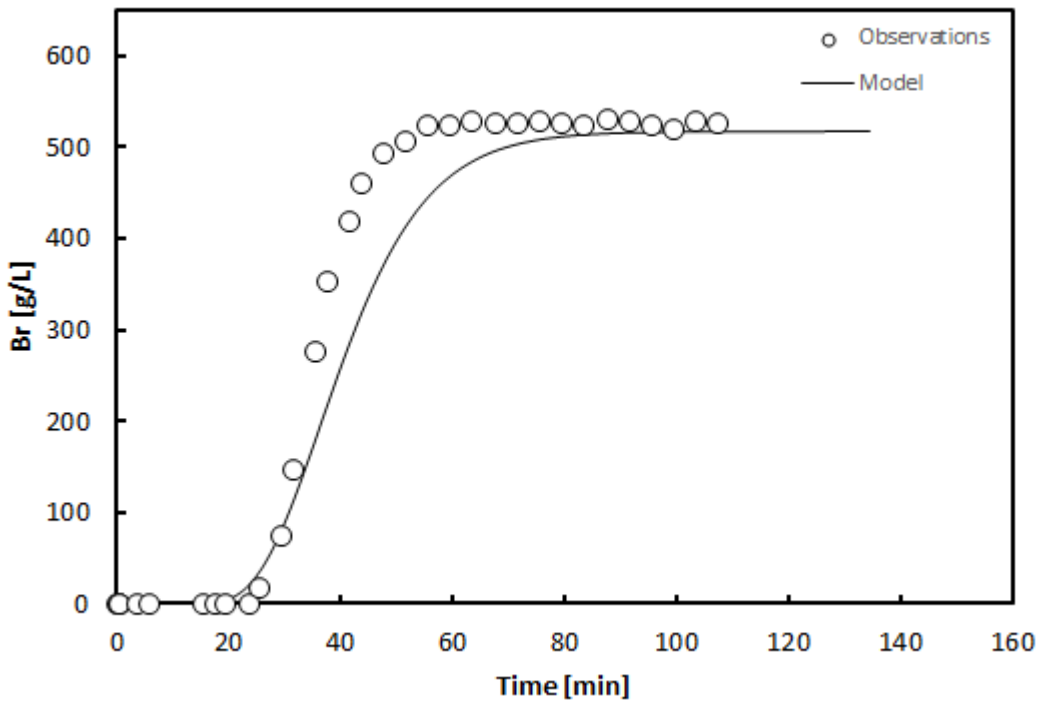

Figure B 3: Br tracer BTC observations and 1-DUSAT modeling results for Br-1-C.

B-3 Sigma Aldrich 150 µm Glass Bead Characterization Data and Calculations

Table B 1: Summary of glass bead density estimation results

Trial	Mass (g)	Volume (cm^3)	Density (g/cm^3)	Average	Standard Deviation
1	20	14	1.43	1.46	0.02
2	25	17	1.47		
3	25	17	1.47		
4	25	17	1.47		
5	50	35	1.43		
6	25	17	1.47		

B-4 Dissection of Sigma Aldrich Bead Packed Column

Following the first Sigma Aldrich glass bead packed contrast scan, the column was dissected to assess the visible interior distribution of NPs. Figure B 4 shows the packed column just before scanning and highlights the fingering of NPs that occurred.

Figure B 5 shows the distribution of NPs within the interior of the column as visible to the naked eye.

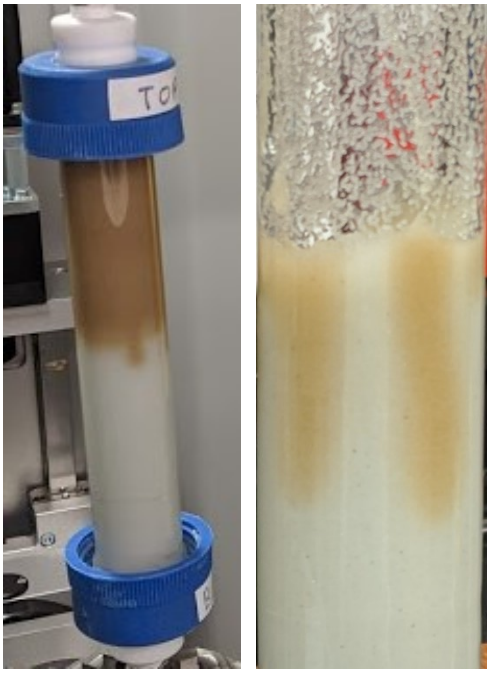

Figure B 4: Sigma Aldrich glass bead wet packed column, showing the column containing NPs before X-ray CT scanning (left) and the column showing obvious NP fingering during column dissection.

4.3cm from top 5.6cm from top 8.8cm from top

Figure B 5: Interior distribution of NPs visible during column dissection.

B-5 Flow-through NaI Detection Threshold Scans

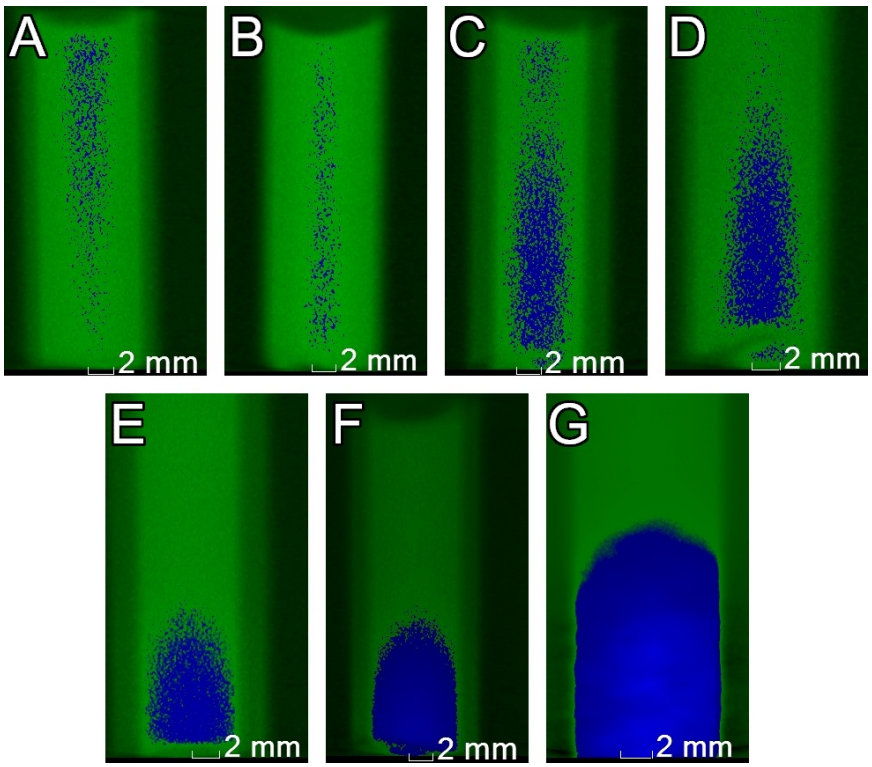

Figure B 6: X-ray CT scan of glass bead packed and saturated flow-through cuvette injected with NaI solutions of 2 g_I/L (A), 10 g_I/L (B), 15 g_I/L (C), 25 g_I/L (D), 50 g_I/L (E), 75 g_I/L (F), and 100 g_I/L (G).

B-6 Liquid to Liquid NaI to Fe_3O_4 NP Cuvette Comparison Scans

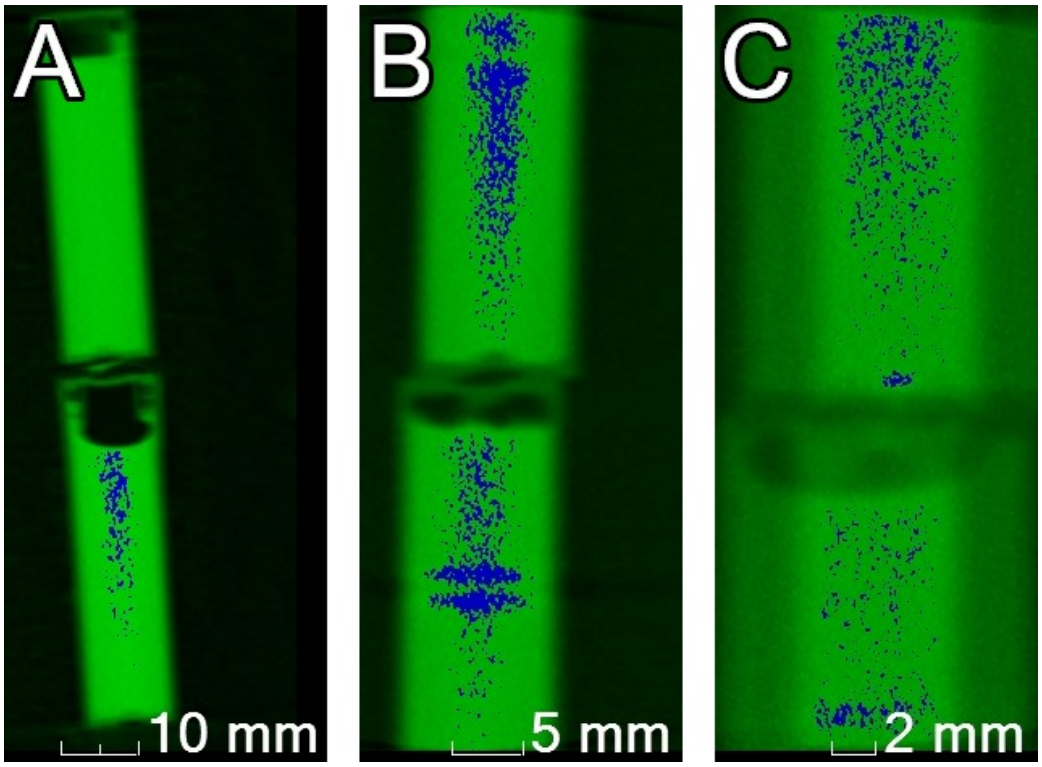

Figure B 7: X-ray CT scan liquid to liquid NaI (top in each scan) to Fe_3O_4 NP (bottom in each scan) cuvette contrast scans showing (A) 2 g/L NaI vs 10 g/L NP, (B) 5g/L NaI vs 25 g/L NP, (C) 10g/L NaI vs 50 g/L NP.

B-7 IFT Experiment X-ray CT Scan Results

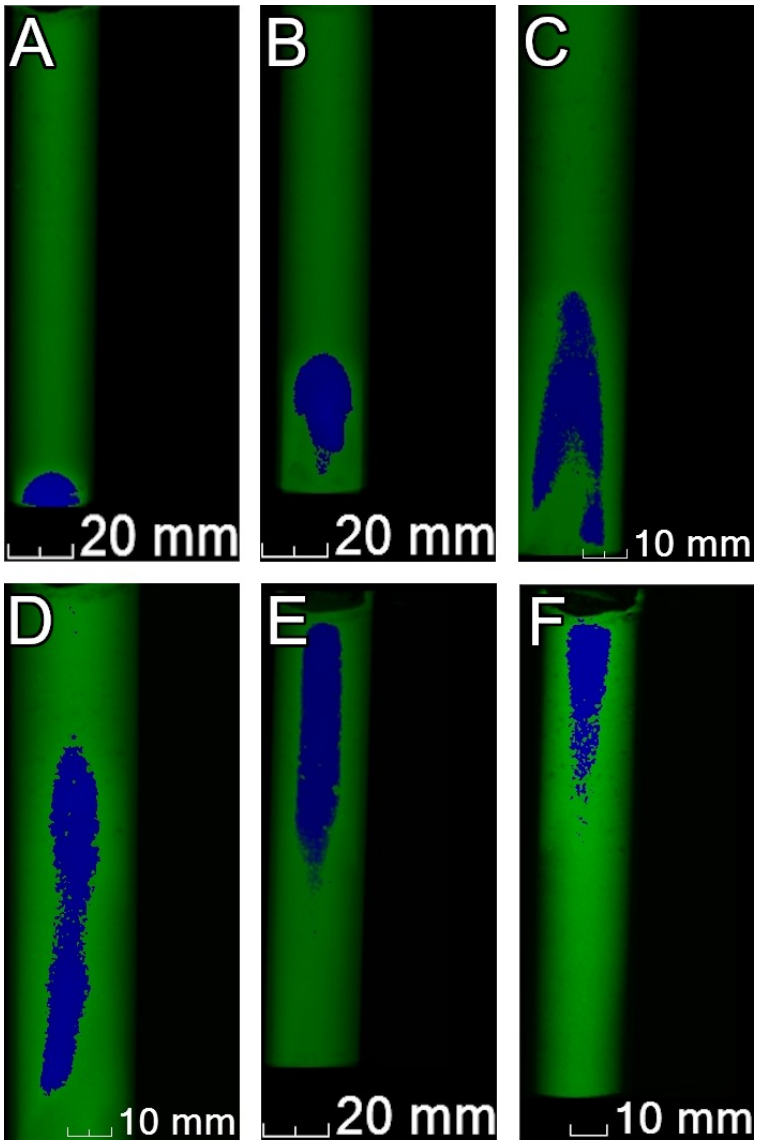

Figure B 8: IFT-1 X-ray CT results showing (A) Scan 2, (B) Scan 3, (C) Scan 4, (D) Scan 5, (E) Scan 6 and (F) Scan 7. Scan 1 was performed before NaI injection. The flow time before Scan 2 – 7 were 10.75 minutes of NaI injection followed by 9.25 minutes of flow with Milli-Q water, then flow with Milli-Q water for 15, 15, 20, 20, and 20 minutes, respectively. The stop-flow periods required for Scans 3 – 7 were 49, 64, 40, 44, and 54 minutes, respectively.

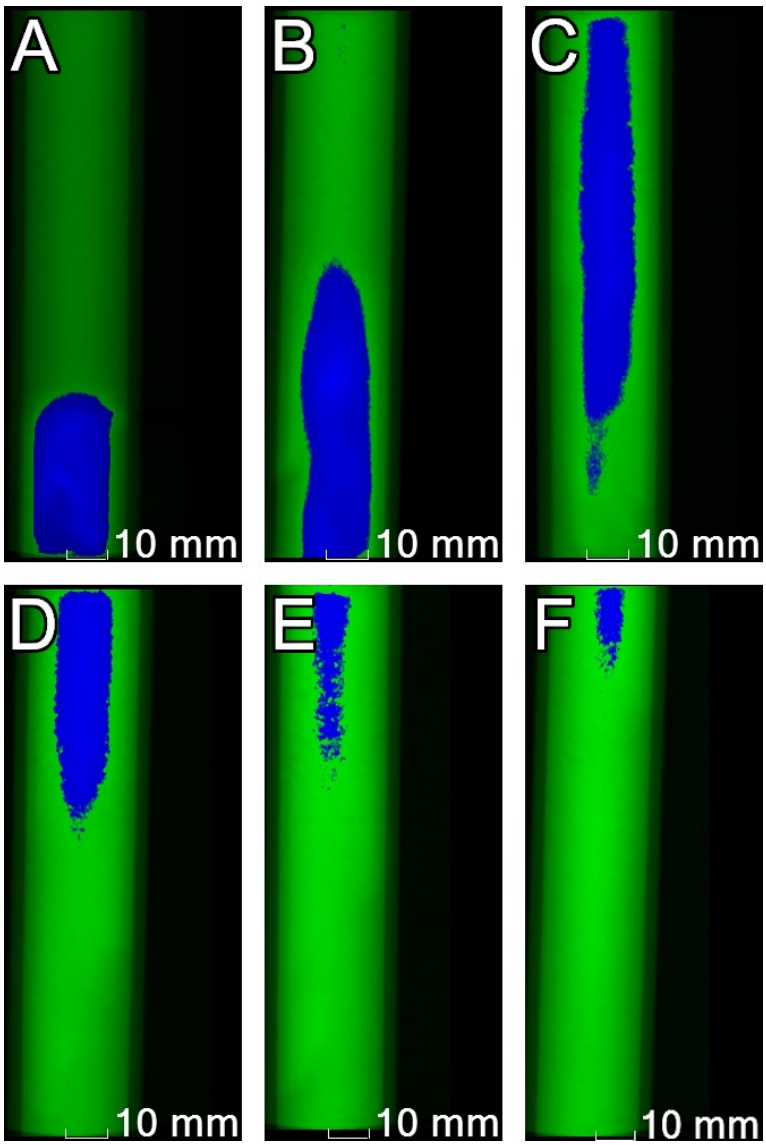

Figure B 9: IFT-3 X-ray CT results showing (A) Scan 2, (B) Scan 3, (C) Scan 5, (D) Scan 6, (E) Scan 7 and (F) Scan 8. Scan 1 was performed before NaI injection. The flow time before Scan 2, Scan 3, Scans 4 and 5, and Scans 6 – 8, were 3.5 minutes of NaI injection followed by 11 minutes of flow with Milli-Q water, then flow with Milli-Q water for 4.5, 10.5, 6, 6 and 6 minutes, respectively. The stop-flow periods required for Scan 3, Scans 4 and 5, and Scans 6–8 were 63.5, 128.5, 78, 73, and 66 minutes, respectively.

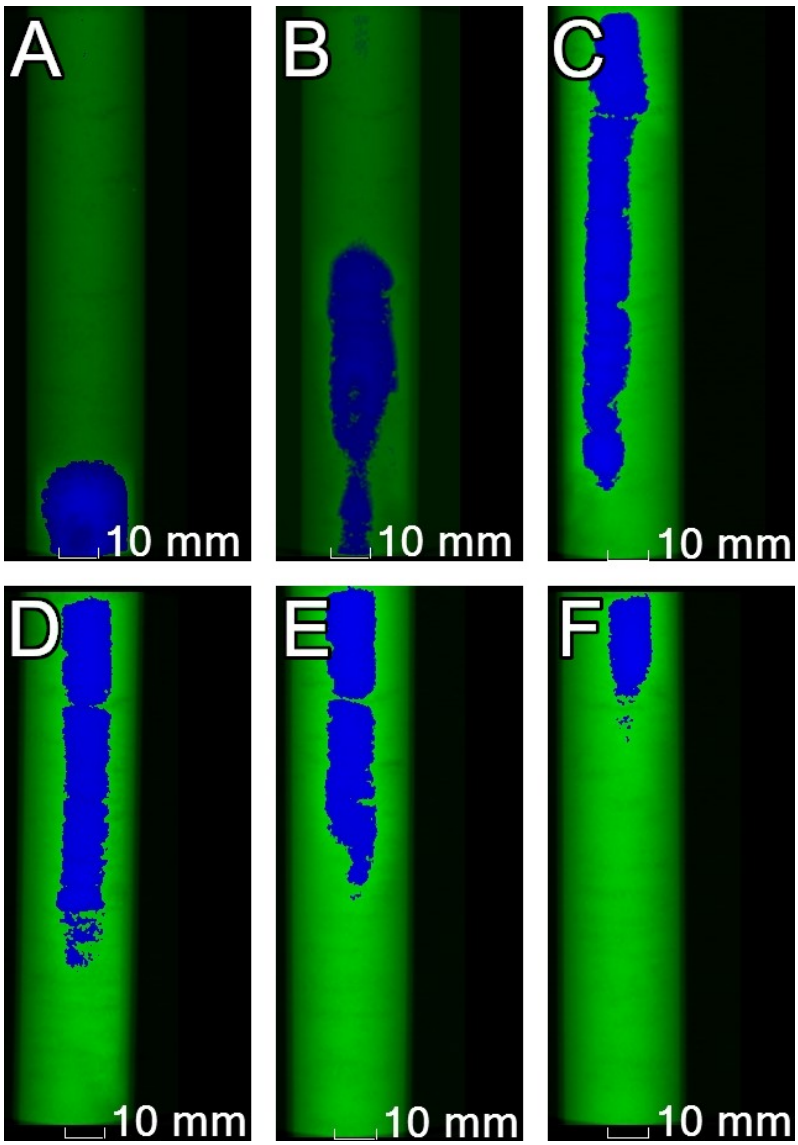

Figure B 10: IFT-4 X-ray CT results showing (A) Scan 2, (B) Scan 3, (C) Scan 4, (D) Scan 5, (E) Scan 7 and (F) Scan 8. Scan 1 was performed before NaI injection. The flow time before Scan 2 –5, Scans 6 and 7, and Scan 8 were 11.5 minutes of NaI injection followed by 10 minutes of flow with Milli-Q water, then flow with Milli-Q water for 26, 29, 25, 50 and 25 minutes, respectively. The stop-flow periods required for Scans 3–5, Scans 6 and 7, and Scan 8 were 47, 44, 51, 84, and 39 minutes, respectively.

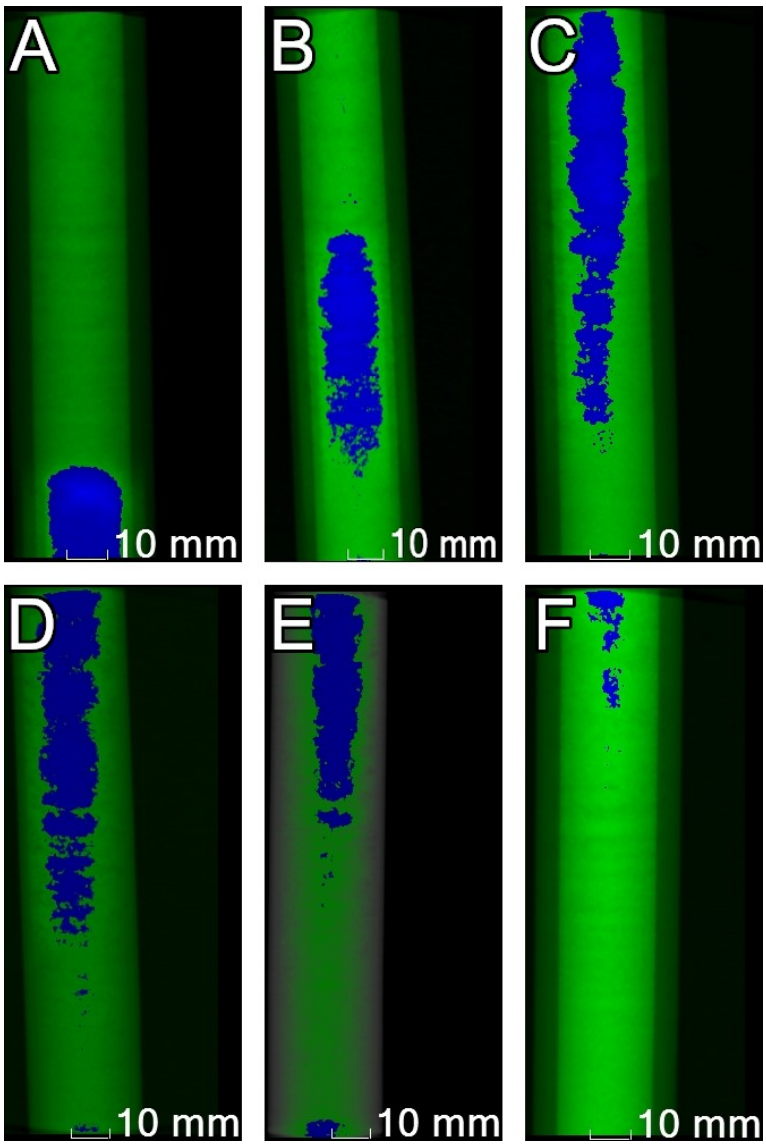

Figure B 11: IFT-5 X-ray CT results showing (A) Scan 2, (B) Scan 3, (C) Scan 4, (D) Scan 5, (E) Scan 6 and (F) Scan 7. Scan 1 was performed before NaI injection. The flow time before Scan 2 – 7 were 5.5 minutes of NaI injection followed by 5 minutes of flow with Milli-Q water, then flow with Milli-Q water for 10, 10, 10, 10, and 14 minutes, respectively. The stop-flow periods required for Scans 3–7 were 57, 62, 59, 55, and 57 minutes, respectively.

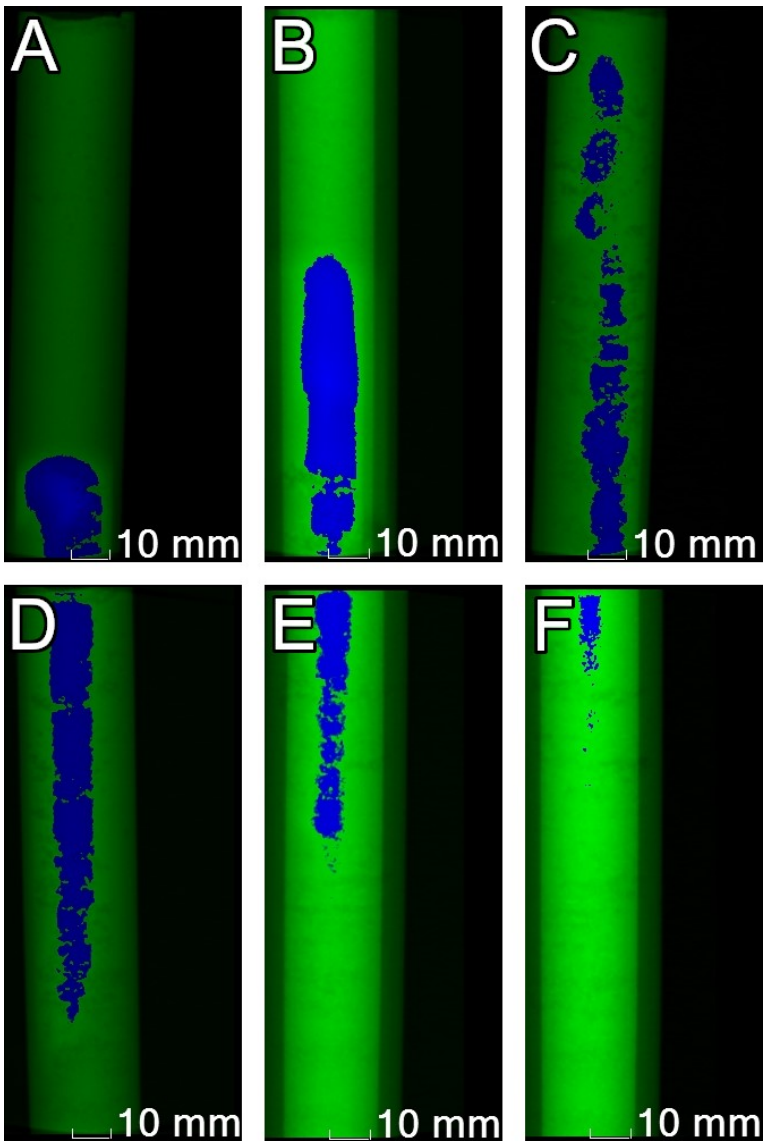

Figure B 12: IFT-6 X-ray CT results showing (A) Scan 2, (B) Scan 3, (C) Scan 4, (D) Scan 6, (E) Scan 7 and (F) Scan 8. Scan 1 was performed before NaI injection. The flow time before Scans 2 – 4, Scans 5 and 6, and Scans 7–8 were 3.5 minutes of NaI injection followed by 4 minutes of flow with Milli-Q water, then flow with Milli-Q water for 7.5, 7.5, 15, 11.5 and 12.5 minutes, respectively. The stop-flow periods required for Scans 3-4, Scans 5 and 6, and Scans 7-8 were 56.5, 62.5, 121, 51.5, and 48.5 minutes, respectively.

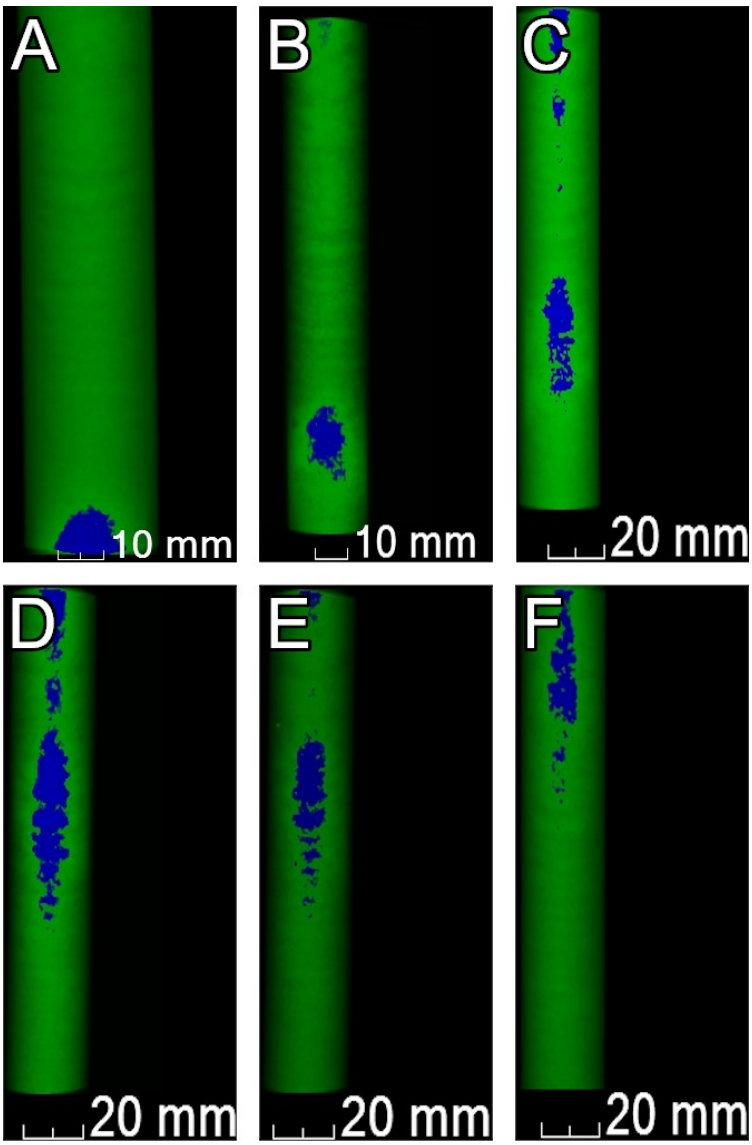

Figure B 13: IFT-7 X-ray CT results showing (A) Scan 2, (B) Scan 3, (C) Scan 4, (D) Scan 5, (E) Scan 6 and (F) Scan 7. Scan 1 was performed before NaI injection. The flow time before Scan 2 – 7 were 10.75 minutes of NaI injection followed by 9.25 minutes of flow with Milli-Q water, then flow with Milli-Q water for 15, 15, 20, 20, and 20 minutes, respectively. The stop-flow periods required for Scans 3–7 were 49, 64, 38, 46, and 52 minutes, respectively.

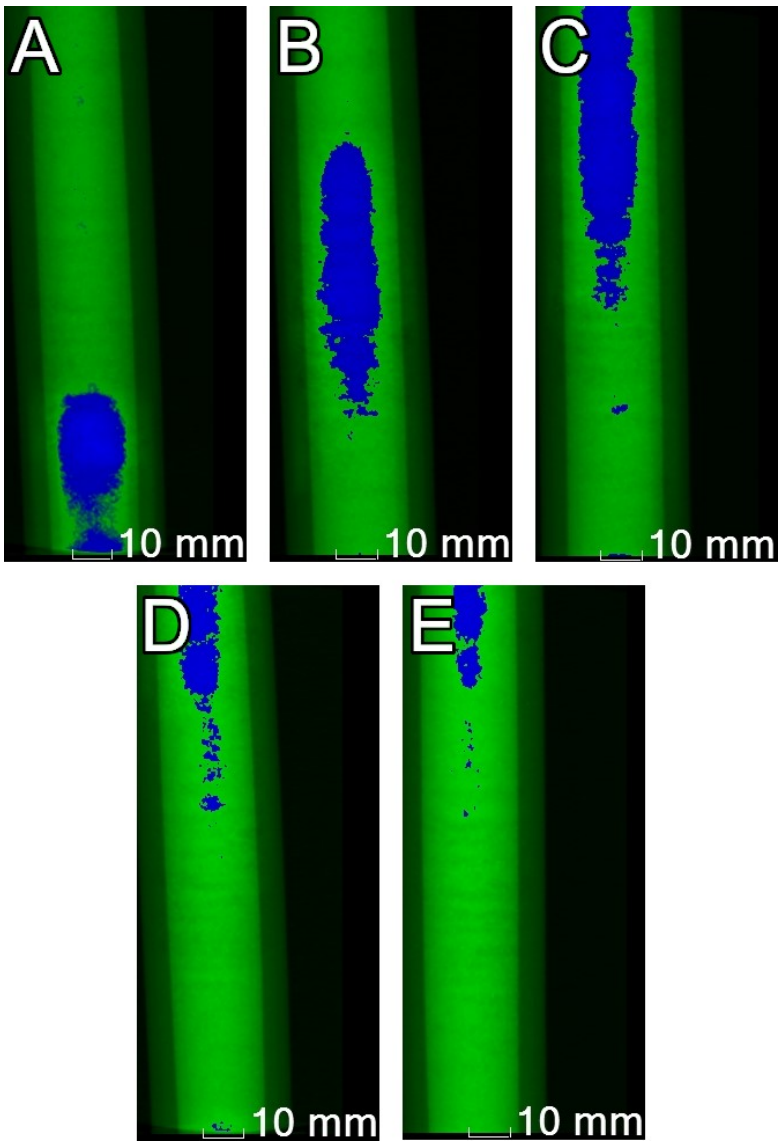

Figure B 14: IFT-8 X-ray CT results showing (A) Scan 2, (B) Scan 3, (C) Scan 4, (D) Scan 5, and (E) Scan 6. Scan 1 was performed before NaI injection. The flow time before Scan 2 – 6 were 5.5 minutes of NaI injection followed by 5 minutes of flow with Milli-Q water, then flow with Milli-Q water for 10, 8, 10, and 12 minutes, respectively. The stop-flow periods required for Scans 3–6 were 165, 64, 53, and 44 minutes, respectively.

B-8 Pycnometer Calibration and NaI Density Data

Table B 2: Pycnometer Calibration Data.

Parameter	Measurement 1	Measurement 1	Measurement 1	Average	St. Dev
Mass of Pycnometer (g)	10.7193	10.7195	10.7194	10.7194	1.0E-04
Known Density of DI Water @ 22 C (g/cm^3)	0.99776 (Engineering ToolBox, 2003)				
Volume of Pycnometer	10.00805137				

Table B 3: NaI density measurements.

NaI Concentration (g_I/L)	Weight (g)			Average	St. Dev	Density g/cm^3
	Measurement 1	Measurement 2	Measurement 3			
25	20.8782	20.8783	20.8778	20.8781	2.6E-04	1.0151
50	21.0618	21.0616	21.0613	21.0616	2.5E-04	1.0334
75	21.2497	21.2495	21.2496	21.2496	1.0E-04	1.0522
100	21.4284	21.4282	21.428	21.4282	2.0E-04	1.0700
125	21.614	21.6139	21.6138	21.6139	1.0E-04	1.0886
150	21.7924	21.7925	21.7922	21.7924	1.5E-04	1.1064
175	21.9686	21.9689	21.9684	21.9686	2.5E-04	1.1240
200	22.1755	22.1758	22.1756	22.1756	1.5E-04	1.1447
Milli Q Water	20.6954	20.6954	20.6951	20.6953	1.7E-04	0.9968
DI Water	20.7062	20.7045	20.7044	20.7050	1.0E-03	0.9978

B-9 All IFT Experiment BTCs

The calculated standard deviation on each IC NaI measurement was $\pm$ 0.206 g/L (accounting for dilution factor and ignoring errors introduced by the dilution process) based on the standard deviation of all 100 mg_I/L standard measurements. The BTCs for IFT-1, 2, 3, 5, 6, 7, 8, are shown in Figure B 15-Figure B 22, respectively.

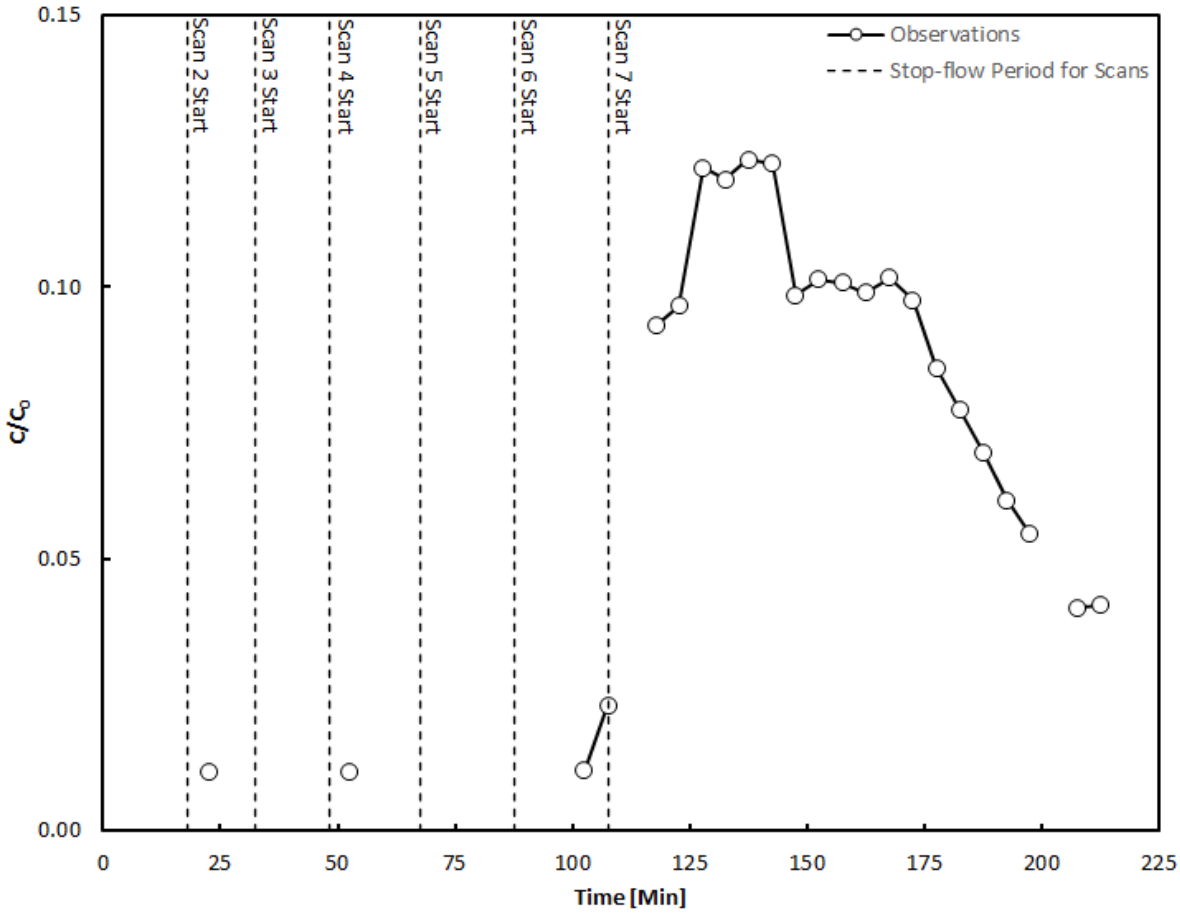

Figure B 15: BTC for IFT-1. The time of the stop-flow periods required for each X-ray CT scan have been removed for clarity. The vertical black dashed lines represent the location of each stop-flow period for each scan relative to the effluent sample points. Effluent sample collection began after Scan 1. The stop-flow times for Scans 2 through 7 were approximately 143, 49, 64, 80, 88, and 54 minutes, respectively.

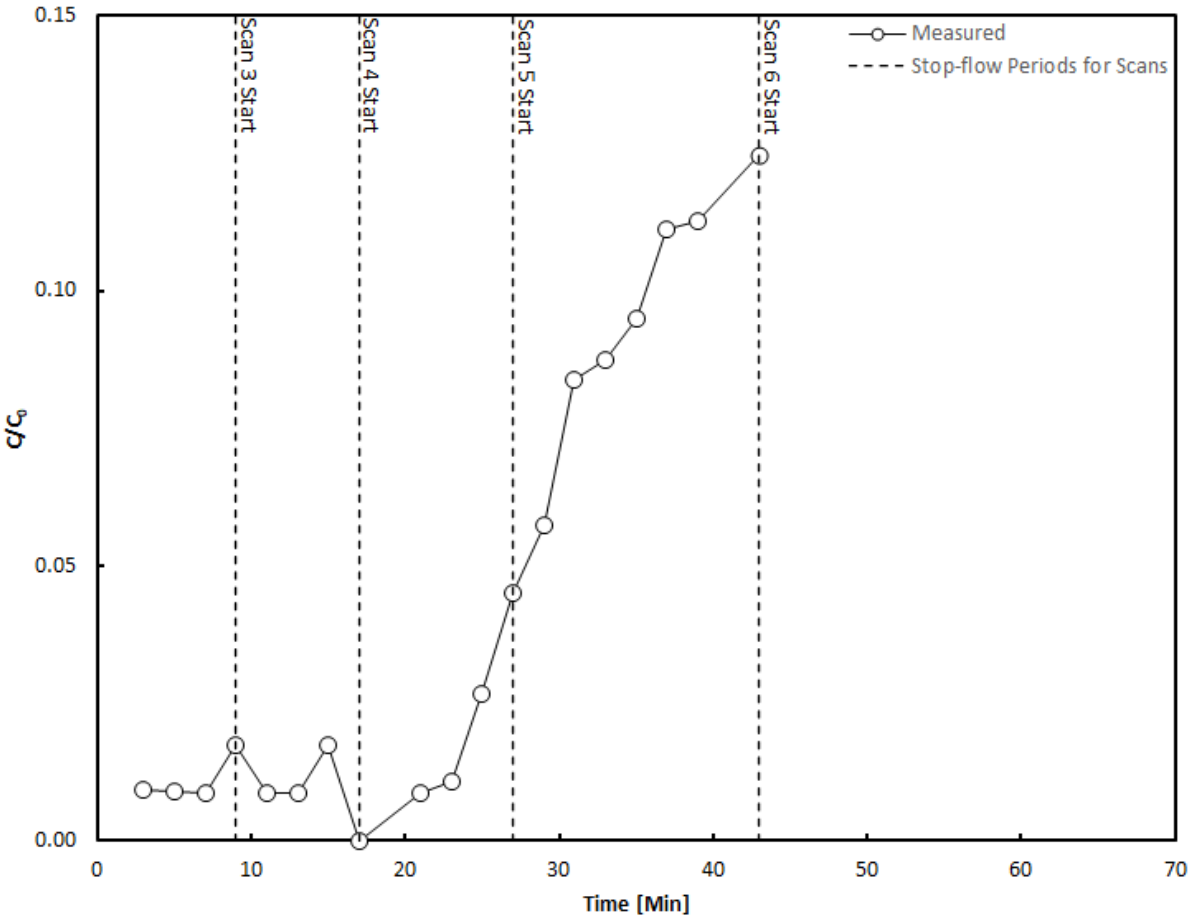

Figure B 16: BTC for IFT-2. The time of the stop-flow periods required for each X-ray CT scan have been removed for clarity. The vertical black dashed lines represent the location of each stop-flow period for each scan relative to the effluent sample points. Effluent sample collection began after Scan 2. The stop-flow times for Scans 3 through 6 were approximately 170, 56, 40, and 87 minutes, respectively.

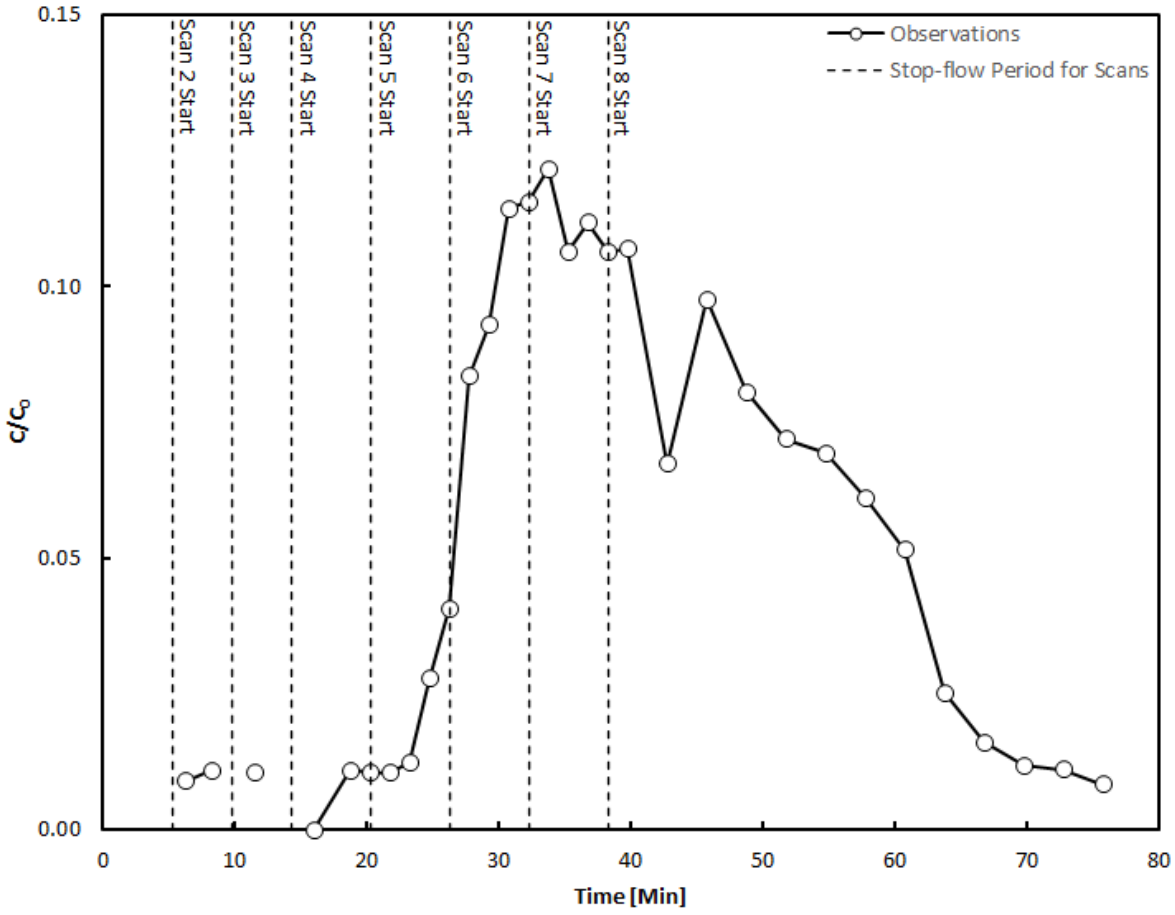

Figure B 17: BTC for IFT-3. The time of the stop-flow periods required for each X-ray CT scan have been removed for clarity. The vertical black dashed lines represent the location of each stop-flow period for each scan relative to the effluent sample points. Effluent sample collection began after Scan 2. The stop flor times for Scans 2 through 8 were approximately 82.5, 63.5, 61.5, 67, 78, 73, and 66 minutes, respectively.

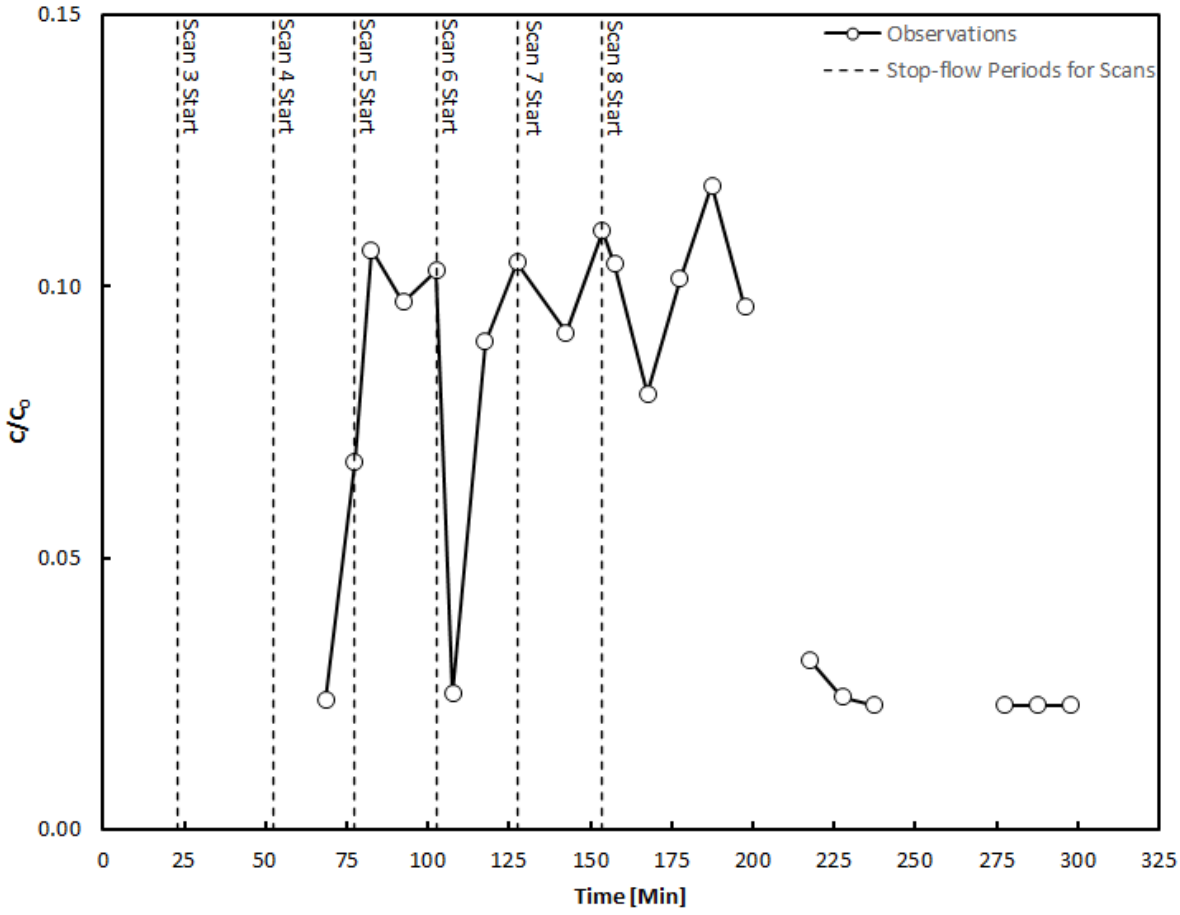

Figure B 18: BTC for IFT-4. The time of the stop-flow periods required for each X-ray CT scan have been removed for clarity. The vertical black dashed lines represent the location of each stop-flow period for each scan relative to the effluent sample points. Effluent sample collection began after Scan 2. The stop flor times for Scans 3 through 8 were approximately 47, 44, 51, 48, 36, and 39 minutes, respectively.

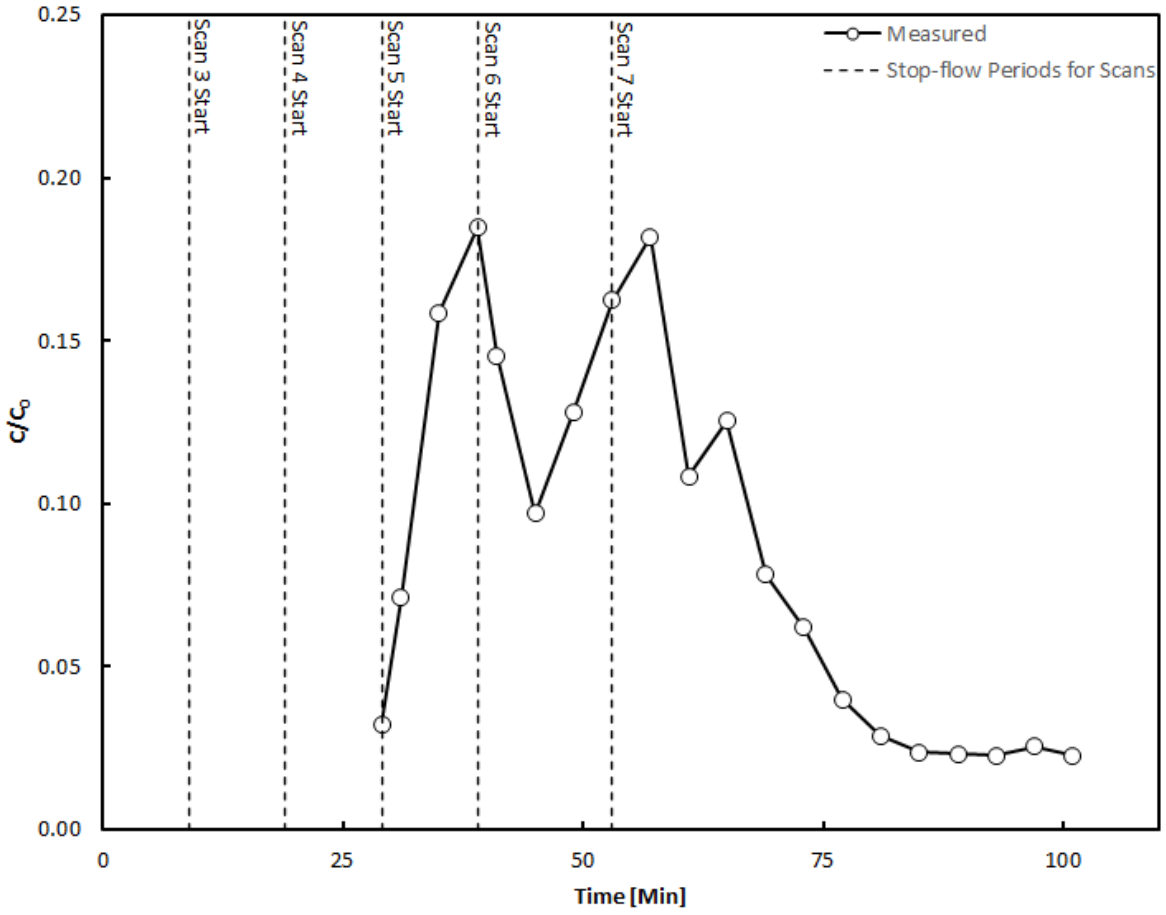

Figure B 19: BTC for IFT-5. The time of the stop-flow periods required for each X-ray CT scan have been removed for clarity. The vertical black dashed lines represent the location of each stop-flow period for each scan relative to the effluent sample points. Effluent sample collection began after Scan 2. The stop flor times for Scans 3 through 7 were approximately 57, 62, 59, 55, and 57 minutes, respectively.

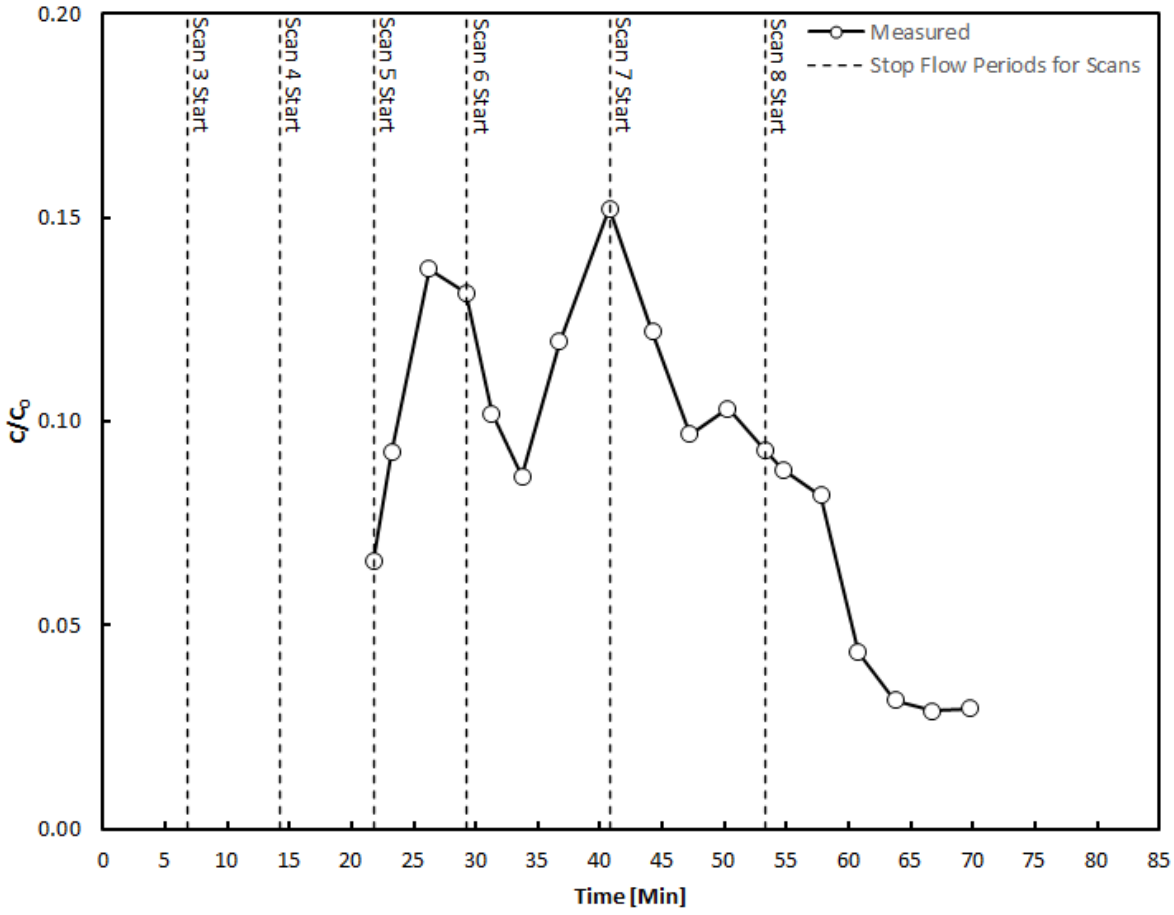

Figure B 20: BTC for IFT-6. The time of the stop-flow periods required for each X-ray CT scan have been removed for clarity. The vertical black dashed lines represent the location of each stop-flow period for each scan relative to the effluent sample points. Effluent sample collection began after Scan 2. The stop flor times for Scans 3 through 8 were approximately 56.5, 62.5, 59.5, 61.5, 51.5, and 48.5 minutes, respectively.

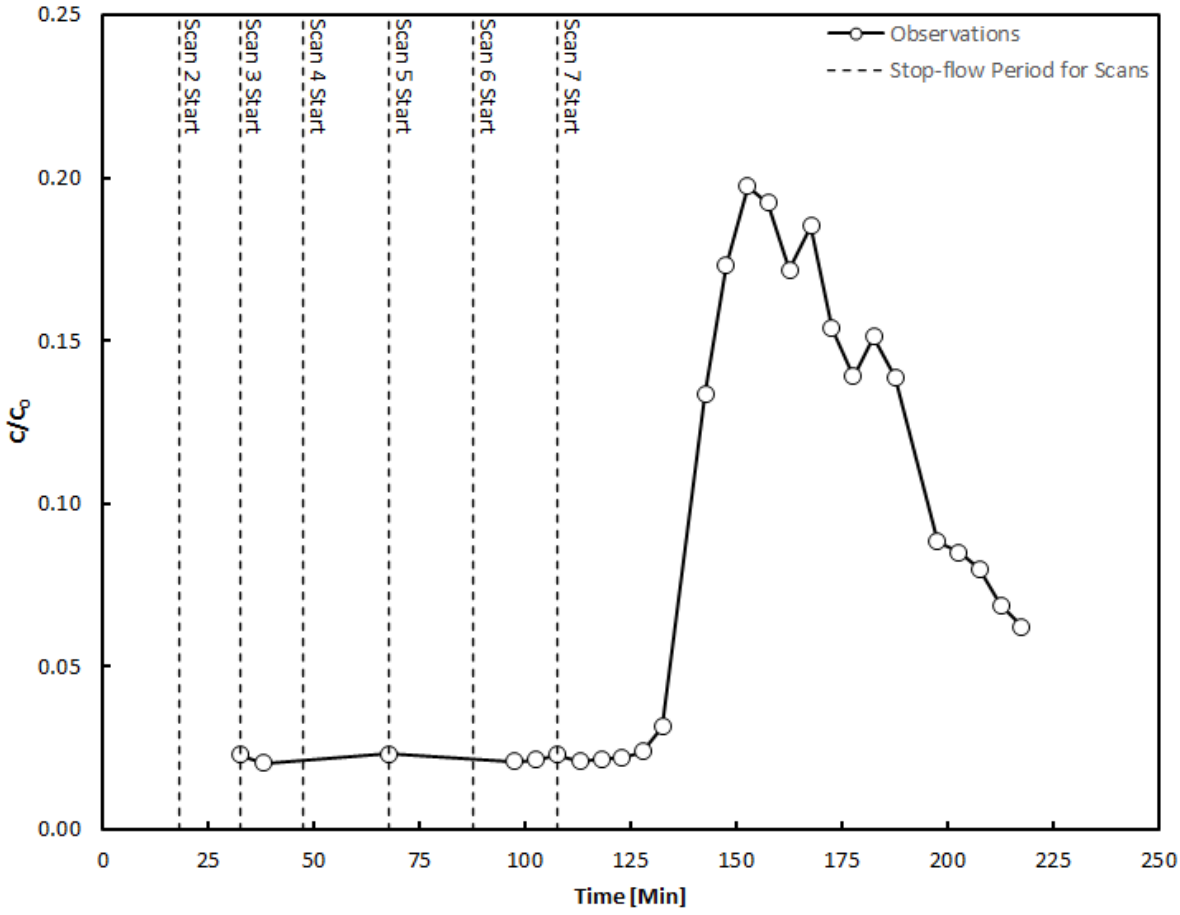

Figure B 21: BTC for IFT-7. The time of the stop-flow periods required for each X-ray CT scan have been removed for clarity. The vertical black dashed lines represent the location of each stop-flow period for each scan relative to the effluent sample points. Effluent sample collection began after Scan 2. The stop flor times for Scans 2 through 7 were approximately 44, 49, 64, 38, 46, and 52 minutes, respectively.

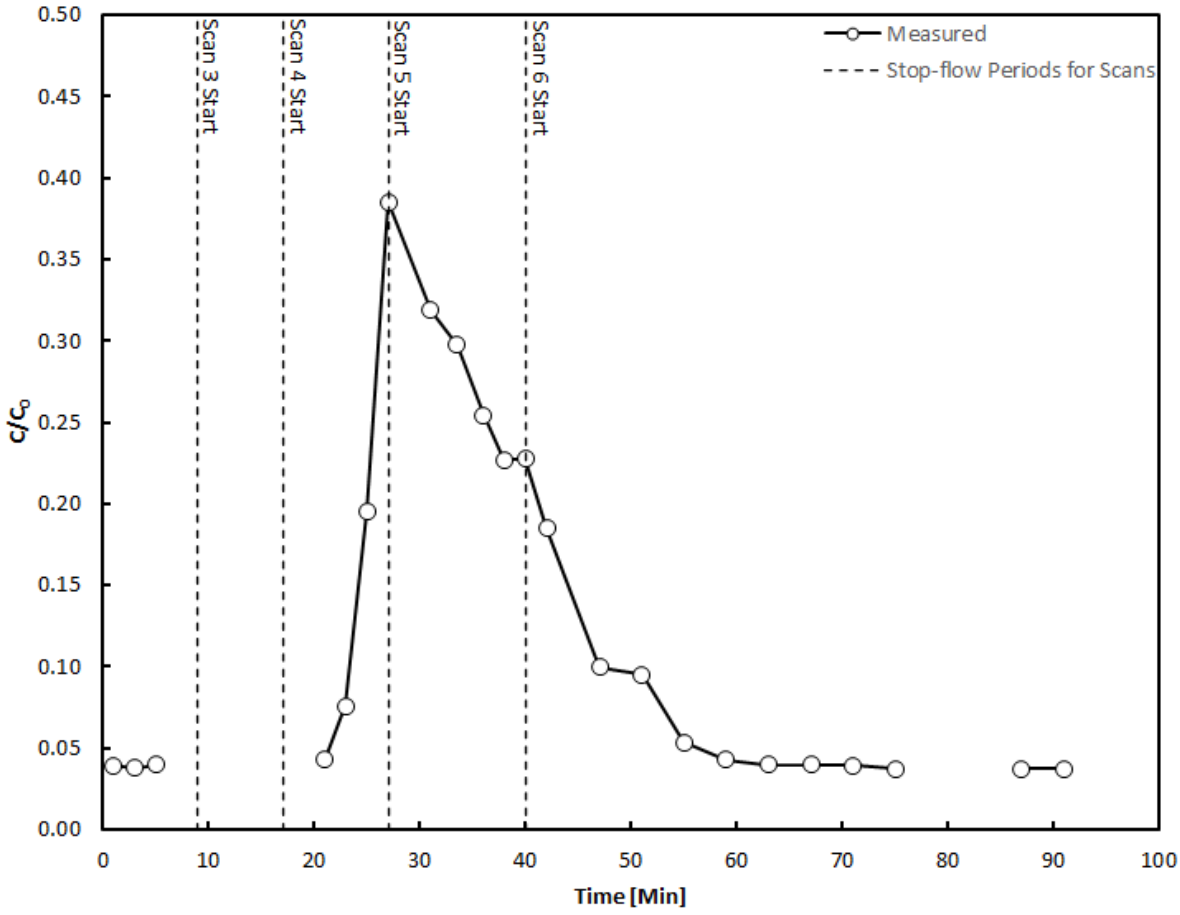

Figure B 22: BTC for IFT-8. The time of the stop-flow periods required for each X-ray CT scan have been removed for clarity. The vertical black dashed lines represent the location of each stop-flow period for each scan relative to the effluent sample points. Effluent sample collection began after Scan 2. The stop flor times for Scans 3 through 6 were approximately 165, 64, 53, and 44 minutes, respectively.